

**EFFECT OF METALS DOPING ON TIN OXIDE THIN FILM
PROPERTIES PREPARED BY SPRAY PYROLYSIS TECHNIQUE**

JUMNAIN PUTPAN

**A THESIS SUBMITTED IN PARTIAL FULFILLMENT OF THE REQUIREMENTS
FOR THE DEGREE OF MASTER OF SCIENCE**

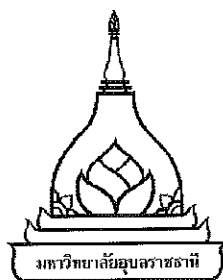
MAJOR IN CHEMISTRY

FACULTY OF SCIENCE

UBON RATCHATHANI UNIVERSITY

YEAR 2012

COPYRIGHT OF UBON RATCHATHANI UNIVERSITY



THESIS APPROVAL
UBON RATCHATHANI UNIVERSITY
MASTER OF SCIENCE
MAJOR IN CHEMISTRY FACULTY OF SCIENCE

TITLE EFFECT OF METALS DOPING ON TIN OXIDE THIN FILM PROPERTIES
PREPARED BY SPRAY PYROLYSIS TECHNIQUE

NAME MR. JUMNAIN PUTPAN

THIS THESIS HAS BEEN ACCEPTED BY

..... (ASST.PROF.DR. SUWAT PABCHANDA)	CHAIR
..... (ASSOC.PROF.DR. JATUPORN WITTAYAKUN)	COMMITTEE
..... (ASST.PROF.DR. JUTHAMAS JITCHAROEN)	COMMITTEE
..... (DR. PRANORM SAEJUENG)	COMMITTEE
..... (ASST.PROF.DR. JANPEN INTARAPRASERT)	DEAN

APPROVAL BY UBON RATCHATHANI UNIVERSITY

.....
(ASSOC.PROF.DR. UTITH INPRASIT)

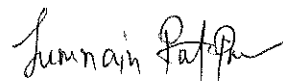
VICE PRESIDENT FOR ACADEMIC AFFAIRS
FOR THE PRESIDENT OF UBON RATCHATHANI UNIVERSITY
ACADEMIC YEAR 2012

ACKNOWLEDGMENTS

I would like to thank my advisor Asst. Prof. Dr. Suwat Pabchanda for his constant advice, guidance, insight, and for sharing his extensive knowledge of chemistry. I am wish to thank Assoc. Prof. Dr. Jatuporn Wittayakun for being a committee and his suggestions. Thanks to Asst. Prof. Dr. Juthamas Jitcharoen and Dr. Pranorm Saejueng for their comments and suggestions. Thanks to the Center for Innovation in Chemistry: Postgraduate Education and Research Program in Chemistry (PERCH-CIC) and Ubon Ratchathani University for financial support.

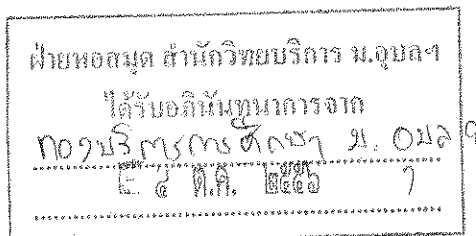
I would also like to thank many people who have contributed their time, instrumentation, and advice to my project. Thanks to Department of Microbiology for SEM analysis. Thanks to Department of Chemistry for UV-Vis Spectrometer, Fluorescence Spectrometer and FT-IR measurement. Thanks to Department of Physics for XRD and AFM measurements. Many thanks to everyone in the Center for Innovation in Chemistry.

I would like to thank all of my family for their love and encouragement.



(Mr. Jumnain Putpan)

Researcher



บทคัดย่อ

ชื่อเรื่อง : ผลของการเจือโลหะต่อสมบัติของฟิล์มบางดีบุกออกไซด์เตรียมโดยเทคนิคสเปรย์ไพโรไลซิส

โดย : จำเนียร พุดพันธ์

ชื่อปริญญา : วิทยาศาสตร์มหาบัณฑิต

สาขาวิชา : เคมี

ประธานกรรมการที่ปรึกษา : ผู้ช่วยศาสตราจารย์ ดร. สุวัฒน์ ผาบจันดา

ศัพท์สำคัญ : ฟิล์มบางดีบุกออกไซด์ การเจือเหล็กหรือพลวง เทคนิคสเปรย์ไพโรไลซิส

งานวิจัยนี้ศึกษาผลของชนิดและความเข้มข้นสารเจือต่อสมบัติทางโครงสร้างและสมบัติเชิงแสงของฟิล์มบางดีบุกออกไซด์เตรียมโดยเทคนิคสเปรย์ไพโรไลซิสบนฐานรองกระจกสไลด์ โดยใช้ 25 มิลลิโมล ทิน (IV) คลอไรด์เพนตะไฮเดรตเป็นสารตั้งต้นในตัวทำละลายผสมของเอทานอล น้ำ และกรดไฮโดรคลอริก อัตราส่วน 90 : 10 : 4 โดยปริมาตร ในงานนี้ปรับเปลี่ยนความเข้มข้นสารเจือไอร์ออน (III) คลอไรด์ และ แอนติโมนี (III) คลอไรด์จากร้อยละ 0 ถึง 18 โดยโมล ระหว่างสเปรย์ไพโรไลซิสใช้อุณหภูมิฐานรองกระจกคงที่ที่ 400 องศาเซลเซียส ตรวจสอบสมบัติทางโครงสร้างและสมบัติเชิงแสงของฟิล์มบางที่เตรียมได้จากผลการวิเคราะห์ด้วยเทคนิคการเลี้ยวเบนรังสีเอกซ์ซึ่งชี้ว่าฟิล์มบางดีบุกออกไซด์ทุกความเข้มข้นของสารเจือมีโครงสร้างผลึกแบบรูไทต์เตตระโกนอล ยกเว้นที่ความเข้มข้นของสารเจือเหล็กร้อยละ 18 โดยโมล การเพิ่มระดับสารเจือส่งผลให้ทั้งขนาดผลึกและความเป็นผลึกของฟิล์มบางลดลง ที่ระดับความเข้มข้นของสารเจือเท่ากันขนาดผลึกของฟิล์มบางดีบุกออกไซด์เจือด้วยสารเจือเหล็กมีขนาดต่ำกว่าฟิล์มบางที่เจือด้วยสารเจือพลวง จากผลการวิเคราะห์ด้วยกล้องจุลทรรศน์อิเล็กตรอนแบบส่องกราดและกล้องจุลทรรศน์แรงอะตอม พบว่าขนาดของเกรนและความขรุขระของพื้นผิวฟิล์มเพิ่มขึ้นเมื่อเพิ่มระดับความเข้มข้นของสารเจือเหล็กและมีค่าลดลงเมื่อเพิ่มระดับความเข้มข้นของสารเจือพลวง จากผลการวิเคราะห์ด้วยฟูเรียร์ทรานสฟอร์มอินฟราเรดสเปกโทรสโกปีบ่งชี้ว่าไอออนดีบุกถูกแทนที่ด้วยไอออนเหล็กหรือพลวงในโครงสร้างแลตทิซดีบุกออกไซด์ โดยพบการเลื่อนของพีคการสั่นของดีบุกออกไซด์ฟิล์มไปยังเลขคลื่นที่เพิ่มขึ้น ผลการวิเคราะห์การเรืองแสงบ่งชี้ว่าความเข้มการเรืองแสงของฟิล์มบางดีบุกออกไซด์เจือด้วยสารเจือพลวงมีค่าลดลงมากกว่าผลของการเจือสารเจือเหล็ก นอกจากนี้

แถบช่องว่างพลังงานเชิงแสงแบบตรงของฟิล์มบางดีบุกออกไซด์มีค่าลดลงเมื่อเจือด้วยสารเจือทั้งสองชนิด ซึ่งการเจือด้วยสารเจือหลักส่งผลให้ค่าดังกล่าวลดลงมากกว่าการเจือด้วยสารเจือพลวง ค่าการส่งผ่านแสงของฟิล์มบางดีบุกออกไซด์ลดลงเมื่อเจือด้วยสารเจือหลัก ในขณะที่ค่าดังกล่าวลดลงสำหรับการเจือด้วยสารเจือพลวงร้อยละ 6 โดยโมลและมีค่าเพิ่มขึ้นที่ความเข้มข้นการเจือสารเจือพลวงสูงขึ้น

ABSTRACT

TITLE : EFFECT OF METALS DOPING ON TIN OXIDE THIN FILM PROPERTIES
PREPARED BY SPRAY PYROLYSIS TECHNIQUE

BY : JUMNAIN PUTPAN

DEGREE : MASTER OF SCIENCE

MAJOR : CHEMISTRY

CHAIR : ASST. PROF. SUWAT PABCHANDA, Ph.D.

KEYWORDS : TIN OXIDE THIN FILMS / IRON OR ANTIMONY DOPING / SPRAY
PYROLYSIS TECHNIQUE

The purpose of this research was to investigate the effect of dopants and their concentrations on structural and optical properties of SnO_2 films prepared by spray pyrolysis technique. The SnO_2 films were deposited on slide glass plates from 25 mmol $\text{SnCl}_4 \cdot 5\text{H}_2\text{O}$ in the mixed solvent of $\text{C}_2\text{H}_5\text{OH}/\text{H}_2\text{O}/\text{HCl}$ 90:10:4 (v/v/v). In this work, FeCl_3 and SbCl_3 were selected as doping additives with quantities varied from 0 to 18 mol%. The glass substrate temperature was kept constant at 400 °C during the spray pyrolysis. The structural and optical properties of the prepared thin films were characterized. From X-ray Diffraction (XRD) results, all deposited SnO_2 thin films were in rutile phase with tetragonal structure, except that of 18 mol% Fe-doping. The increased of doping concentrations resulted in a decreased of both crystallinity and crystalline sizes of prepared doping films. At the same doping level, crystalline sizes of Fe-doping were lower than those of Sb-doping. From Scanning Electron Microscopy (SEM) and Atomic Force Microscopy (AFM) results, the grain sizes and surface roughness of prepared thin films were enhanced with increasing concentration of Fe-doping. However, those of Sb-doping films were decreased with increasing concentration of Sb-doping. From Fourier Transform Infrared Spectroscopy (FT-IR) results, Sn ions were replaced by Fe or Sb ions in SnO_2 lattice, resulting in shift of vibration peak of SnO_2 film to higher wavenumber. The photoluminescence (PL) analysis indicated that both suppressed the PL emission intensity, but the PL intensity of SnO_2 films with Sb-doping was lower than that of Fe-doping. Moreover, the direct optical band gap of the

SnO_2 films decreased for both dopants. More decreased was observed in Fe-doping more than Sb-doping. The transparencies of the SnO_2 films decreased with all increased concentrations of Fe-doping, whereas the transparency of 6 mol% Sb-doping films was decreased, and those of other Sb-doping films were increased.

CONTENTS

	PAGE
ACKNOWLEDGMENTS	I
ABSTRACT IN THAI	II
ABSTRACT IN ENGLISH	IV
CONTENTS	VI
LIST OF TABLES	IX
LIST OF FIGURES	X
LIST OF ABBREVIATIONS	XV
CHAPTER	
1 INTRODUCTION	1
2 LITERATURE REVIEWS	
2.1 Basic properties of undoped and (Fe or Sb)-doped SnO ₂ films	3
2.2 Thin film deposition methods	4
2.3 Precursor and their concentration	6
2.4 Solvent for spray pyrolysis	8
2.5 Deposition temperature for spray pyrolysis	8
3 EXPERIMENTAL	
3.1 Chemicals and instruments	10
3.2 Experimental	11
3.3 Characterization techniques	11
3.3.1 X-ray Diffraction (XRD)	11
3.3.2 Scanning Electron Microscopy (SEM)	13
3.3.3 Atomic Force Microscopy (AFM)	13
3.3.4 Fourier Transform Infrared Spectroscopy (FT-IR)	14
3.3.5 Fluorescence Spectroscopy	14
3.3.6 UV-Visible Spectroscopy	14

CONTENTS (CONTINUED)

	PAGE
4 RESULTS AND DISCUSSION	
4.1 Structural analysis of undoped and (Fe or Sb)-doped tin oxide films	16
4.2 Surface analysis of undoped and (Fe or Sb)-doped tin oxide films	25
4.2.1 Surface morphology studies of undoped and (Fe or Sb)-doped tin oxide films by SEM	25
4.2.2 Surface morphology studies of undoped and (Fe or Sb)-doped tin oxide films by AFM	29
4.3 Optical properties of undoped and (Fe or Sb)-doped tin oxide films	35
4.3.1 Characterization of undoped and (Fe or Sb)-doped tin oxide films by FT-IR	35
4.3.2 Effect of dopants (Fe or Sb) and doping levels on the photoluminescence properties of tin oxide films	37
4.3.3 Effect of dopants (Fe or Sb) and doping levels on the transparency of tin oxide films	40
4.3.4 Effect of dopants (Fe or Sb) and doping levels on the optical band gap energy of tin oxide films	43
5 CONCLUSIONS	47
REFERENCES	49

CONTENTS (CONTINUED)

	PAGE
APPENDICES	
A Results of characterized studies	57
B Estimation of photoluminescence emission intensity of prepared thin films with background correction method	90
VITAE	94

LIST OF TABLES

TABLE		PAGE
2.1	The advantages and disadvantages of various methods for prepared SnO ₂ films	5
3.1	Chemicals	10
3.2	Instruments	10
4.1	Summary of XRD parameters for different dopants and various doping concentrations	17
4.2	Approximately average grain size of SnO ₂ thin films for different dopants and their doping levels	28
4.3	The main vibration frequencies (cm ⁻¹) of SnO ₂ thin films for different dopants and various doping levels	37
4.4	Photoluminescence (PL) emission intensity of SnO ₂ thin films for different dopants and various doping levels	39
4.5	Transparency (%T) of SnO ₂ thin films for different dopants and their doping levels	43
4.6	The direct optical band gap of SnO ₂ thin films for different and their doping levels	45
1B	Data from emission spectrum of SnO ₂ sample	92

LIST OF FIGURES

FIGURE	PAGE
2.1 The primitive tetragonal unit cell of the bulk SnO_2 , with the basis of $(\text{SnO}_2)_2$. The lattice parameters are $a = 0.4737 \text{ nm}$, $c = 0.3186 \text{ nm}$ and $u = 0.306$	4
4.1 X-ray diffraction patterns of Fe-doped SnO_2 thin films for various doping levels: 0, 6, 12, 18 and 100 mol%	18
4.2 X-ray diffraction patterns of Sb-doped SnO_2 thin films for various doping levels: 0, 6, 12, 18 and 100 mol%	19
4.3 FWHM for thin films at various dopant as a function of mol% doping concentration in spray solution	22
4.4 Crystalline size for thin films at various dopant as a function of mol% doping concentration in spray solution	23
4.5 Tetragonality (c/a) for thin films at various dopant as a function of mol% doping concentrations in spray solution	24
4.6 XRD peak intensity of (211) orientation for thin films at various dopant as a function of mol% doping concentration in spray solution	25
4.7 SEM micrographs of SnO_2 thin films for different dopants and various doping levels: (a) undoped SnO_2 , (b) Fe-doped SnO_2 6 mol%, (c) Fe-doped SnO_2 12 mol% and (d) Fe-doped SnO_2 18 mol%	26
4.8 SEM micrographs of SnO_2 thin films for different dopants and various doping levels: (a) Sb-doped SnO_2 6 mol%, (b) Sb-doped SnO_2 12 mol% and (c) Sb-doped SnO_2 18 mol%	27
4.9 Approximately average grain sizes of films at various dopant as a function of mol% doping concentrations in spray solution	29

LIST OF FIGURES (CONTINUED)

FIGURE	PAGE
4.10 2D and 3D AFM micrograph of SnO ₂ thin films for difference dopants and various doping levels: (a) undoped SnO ₂ , (b) Fe-doped SnO ₂ 6 mol%, (c) Fe-doped SnO ₂ 12 mol% and (d) Fe-doped SnO ₂ 18 mol%	31
4.11 2D and 3D AFM micrograph of SnO ₂ thin films for difference dopants and various doping levels: (a) undoped SnO ₂ , (b) Sb-doped SnO ₂ 6 mol%, (c) Sb-doped SnO ₂ 12 mol% and (d) Sb-doped SnO ₂ 18 mol%	32
4.12 Root mean square (RMS) roughness of films at various dopant as a function of mol% doping concentration in spray solution	33
4.13 Mean grain sizes from AFM of thin films at various dopant as a function of mol% doping concentration in spray solution	34
4.14 FT-IR spectra of the powder scratched from films: (a) undoped SnO ₂ , (b) Fe-doped SnO ₂ 6 mol%, (c) Fe-doped SnO ₂ 12 mol%, (d) Fe-doped SnO ₂ 18 mol%, (e) Sb-doped SnO ₂ 6 mol%, (f) Sb-doped SnO ₂ 12 mol% and (g) Sb-doped SnO ₂ 18 mol%	36
4.15 Photoluminescence spectra of (a) undoped SnO ₂ , (b) Fe-doped SnO ₂ 6 mol%, (c) Fe-doped SnO ₂ 12 mol%, (d) Fe-doped SnO ₂ 18 mol%, (e) Sb-doped SnO ₂ 6 mol%, (f) Sb-doped SnO ₂ 12 mol% and (g) Sb-doped SnO ₂ 18 mol%	38
4.16 Variation of PL emission intensity of SnO ₂ films films at various dopant as a function of mol% doping concentration in spray solution	40
4.17 Optical transparency of thin films at various dopant as a function of mol% doping concentration in spray solution: (a) undoped SnO ₂ , (b) Fe-doped SnO ₂ 6 mol%, (c) Fe-doped SnO ₂ 12 mol%, (d) Fe-doped SnO ₂ 18 mol%, (e) Sb-doped SnO ₂ 6 mol%, (f) Sb-doped SnO ₂ 12 mol% and (g) Sb-doped SnO ₂ 18 mol%	41

LIST OF FIGURES (CONTINUED)

FIGURE		PAGE
4.18	Average transmittance value in visible region (400 - 800 nm) from transmission spectra of thin films at various dopant as a function of mol% doping concentration in spray solution	42
4.19	Direct optical band gap of thin films at various dopant as a function of mol% doping concentration in spray solution: (a) undoped SnO ₂ , (b) Fe-doped SnO ₂ 6 mol%, (c) Fe-doped SnO ₂ 12 mol%, (d) Fe-doped SnO ₂ 18 mol%, (e) Sb-doped SnO ₂ 6 mol%, (f) Sb-doped SnO ₂ 12 mol% and (g) Sb-doped SnO ₂ 18 mol%	44
4.20	Direct optical band gaps of thin films at various dopant as a function of mol% doping concentration in spray solution	45
A.1	X-ray diffraction patterns of thin films for various doping levels (n = 3); (a) undoped SnO ₂ and (b) Fe-doped SnO ₂ 6 mol%	58
A.2	X-ray diffraction patterns of thin films for various doping levels (n = 3); (a) Fe-doped SnO ₂ 12 mol% and (b) Fe-doped SnO ₂ 18 mol%	59
A.3	X-ray diffraction patterns of Fe ₂ O ₃ thin films (n = 3)	60
A.4	X-ray diffraction patterns of thin films for various doping levels (n = 3); (a) Sb-doped SnO ₂ 6 mol% and (b) Sb-doped SnO ₂ 12 mol%	61
A.5	X-ray diffraction patterns of thin films (n = 3); (a) Sb-doped SnO ₂ 18 mol% and (b) Sb ₂ O ₃ film	62
A.6	SEM micrographs thin films (n = 2); (a) SnO ₂ and (b) Fe-doped SnO ₂ 6 mol%	63
A.7	SEM micrographs of SnO ₂ thin films for different doping levels (n = 2); (a) Sb-doped SnO ₂ 6 mol% and (b) Sb-doped SnO ₂ 12 mol%	64
A.8	SEM micrographs of SnO ₂ thin films for different doping levels (n = 2); (a) Sb-doped SnO ₂ 6 mol% and (b) Sb-doped SnO ₂ 12 mol%	65

LIST OF FIGURES (CONTINUED)

FIGURE	PAGE
A.9 SEM micrographs of Sb-doped SnO ₂ 18 mol% thin films (n = 2)	66
A.10 2D (left) and 3D (right) AFM micrographs of SnO ₂ thin films (n = 3)	67
A.11 2D (left) and 3D (right) AFM micrographs of Fe-doped SnO ₂ 6 mol% (n = 3)	68
A.12 2D (left) and 3D (right) AFM micrographs of Fe-doped SnO ₂ 12 mol% (n = 3)	69
A.13 2D (left) and 3D (right) AFM micrographs of Fe-doped SnO ₂ 18 mol% (n = 3)	70
A.14 2D (left) and 3D (right) AFM micrographs of Sb-doped SnO ₂ 6 mol% thin films (n = 3)	71
A.15 2D (left) and 3D (right) AFM micrographs of Sb-doped SnO ₂ 12 mol% thin film (n = 3)	72
A.16 2D (left) and 3D (right) AFM micrographs of Sb-doped SnO ₂ 18 mol% thin films (n = 3)	73
A.17 FT-IR spectra of films (n = 3); (a) undoped SnO ₂ and (b) Fe-doped SnO ₂ 6 mol%	74
A.18 FT-IR spectra of films (n = 3); (a) Fe-doped SnO ₂ 12 mol% and (b) Fe-doped SnO ₂ 18 mol%	75
A.19 FT-IR spectra of films (n = 3); (a) Sb-doped SnO ₂ 6 mol% and (b) Sb-doped SnO ₂ 12 mol%	76
A.20 FT-IR spectra of Sb-doped SnO ₂ 18 mol% thin films (n = 3)	77
A.21 PL spectra of films (n = 3); (a) undoped SnO ₂ and (b) 6 mol% Fe-doped SnO ₂	78
A.22 PL spectra of films (n = 3); (a) Fe-doped SnO ₂ 12 mol% and (b) Fe-doped SnO ₂ 18 mol%	79

LIST OF FIGURES (CONTINUED)

FIGURE	PAGE
A.23 PL spectra of films ($n = 3$); (a) Sb-doped SnO_2 6 mol% and (b) Sb-doped SnO_2 12 mol%	80
A.24 PL spectra of Sb-doped SnO_2 18 mol% thin films ($n = 3$)	81
A.25 Optical transparencies of films ($n = 3$); (a) undoped SnO_2 and (b) 6 mol% Fe-doped SnO_2	82
A.26 Optical transparencies of films ($n = 3$); (a) Fe-doped SnO_2 12 mol% and (b) Fe-doped SnO_2 18 mol%	83
A.27 Optical transparencies of films ($n = 3$); (a) Sb-doped SnO_2 6 mol% and (b) Sb-doped SnO_2 12 mol%	84
A.28 Optical transparencies of Sb-doped SnO_2 18 mol% thin films ($n = 3$)	85
A.29 Optical band gaps of films ($n = 3$); (a) SnO_2 and (b) Fe-doped SnO_2 6 mol%	86
A.30 Optical band gaps of films ($n = 3$); (a) Fe-doped SnO_2 12 mol% and (b) Fe-doped SnO_2 18 mol% film	87
A.31 Optical band gaps of films ($n = 3$); (a) Sb-doped SnO_2 6 mol% and (b) Sb-doped SnO_2 12 mol%	88
A.32 Optical band gaps of Sb-doped SnO_2 18 mol% thin films ($n = 3$)	89
B.1 The positions of presented symbols in background correction equation	91
B.2 Data values of presented symbols in background correction equation	92

LIST OF ABBREVIATIONS

Abbreviations	Full word
TCO	Transparent Conducting Oxide
PPA	Polypropylene Adipate
PECVD	Plasma Enhanced Chemical Vapor Deposition
SPD	Spray Pyrolysis Deposition
XRD	X-ray Diffraction
SEM	Scanning Electron Microscopy
AFM	Atomic Force Microscopy
FT-IR	Fourier Transform Infrared Spectroscopy
UV-Vis	Ultraviolet - Visible Spectroscopy
ATO	Antimony doped tin oxide
eV	Electron volt
g	Gram
°C	Degree of Celsius
CVD	Chemical Vapor Deposition
mol%	Percent by mole
at%	Percent by atom
wt%	Percent by weigh
l	Liter
cm	Centimeter
No.	Number
θ	Bragg's angle
FWHM	Full Width at Half Maxima
JCPDS	Joint Committee on Powder Diffraction Standards
E_g	Energy band gap

CHAPTER 1

INTRODUCTION

Transparent conductive oxide (TCO) film was attractive for many optoelectronic devices due to their unique physical properties such as high electrical conductivity and high transparency in the visible region. Thus, transparent and electrically conductive films were widely used for a variety of applications [1-2]. In particular, tin oxide films have high transparency in the visible region, low electrical resistivity, reflectivity in the IR region, stable at high temperatures and very good adhesion to many substrates such as glass [3] and flexible substrate (polypropylene adipate (PPA)) [4]. Therefore, tin oxide films were widely used for a variety of applications such as gas sensor [5-6], dye-sensitized solar cell [7], light emitting diodes [8] and thermoelectric material [9].

There are a number of techniques developed for deposition of thin films on substrate such as magnetron sputtering [10], plasma enhance chemical vapor deposition (PECVD) [11], spin coating [12], dip coating [13], electrostatic spray pyrolysis [14], thermal evaporation [15] and spray pyrolysis deposition (SPD) [16-18] and the properties of thin films relate to the deposition methods. Among these methods, one of the most simple technique is spray pyrolysis in which a thin films is deposited by spraying solution onto the heated substrate where the constituents react to form a chemical compounds [19]. The spray pyrolysis system is rather simple in principle and represents the less expensive alternative method with high deposition rate. In addition, the oxide film prepared by this technique is also physically and chemically resistant against environmental effects and adheres strongly to different substrates. Moreover, the doped oxide films could be easily prepared by adding dopants into the spray solution. These make spray pyrolysis coating to be a good choice for this thesis.

Recently, the structural and optical properties of undoped SnO_2 [5-6, 9-10, 12-18, 20], Fe-doped SnO_2 [21-25] and Sb-doped SnO_2 [4, 11, 26-32] thin films prepared by spray pyrolysis technique were investigated. However, from the best of our knowledge, there is no report for

fabrication of Fe-doped SnO_2 films and Sb-doped SnO_2 films under the same condition on glass substrate by spray pyrolysis method.

The objective of this thesis was to establish a relationship between the dopant (Fe and Sb) and the SnO_2 thin film properties. Therefore, tin oxide films doping with Fe and Sb at different concentrations ranging from 0 to 18 mol% were prepared by spray pyrolysis method. The properties of the films were characterized by X-ray Diffraction (XRD), Scanning Electron Microscopy (SEM), Atomic Force Microscopy (AFM), Fourier Transform Infrared Spectroscopy (FT-IR), Fluorescence Spectroscopy and UV-Visible Spectroscopy.

The present thesis has been derived in the following sequence. Chapter 1 presented the introduction, chapter 2 described some of the previous work related to this thesis, chapter 3 presented the fabrication of SnO_2 , Fe-doped SnO_2 and Sb-doped SnO_2 thin films and characterization techniques used in this work, chapter 4 described the results and discussions and finally, the thesis was concluded in chapter 5.

CHAPTER 2

LITURATURE REVIEWS

In the past decade, transparent conductive oxide (TCO) films were attracted a great attention because of their fascinating properties and potential building blocks for electronics, optoelectronics and sensor applications [1]. Tin oxide (SnO_2) film is one of the promising materials for fabrication of nanodevices such as gas sensor [5-6], dye-sensitized solar cell [7] and light emitting diodes [8]. Currently, tin oxide was the most interesting materials among metal oxides due to their broad application lists related to their optical and electrical properties. For instance, undoped and (Fe or Sb)-doped SnO_2 films could be used in optoelectronics, sensors and transducers. Here, some of the properties of these films were highlighted:

- 2.1 Basic properties of undoped and (Fe or Sb)-doped SnO_2 films
- 2.2 Thin films deposition methods
- 2.3 Precursors and their concentrations
- 2.4 Solvent for spray pyrolysis
- 2.5 Deposition temperature for spray pyrolysis

2.1 Basic properties of undoped and (Fe or Sb)-doped SnO_2 films

These were two forms of tin oxide, differing by the electronic state of the tin atom. When the tin atom was in the +4 oxidation state, the tin oxide was formed in stannic oxide (SnO_2). When the tin atom was in the +2 oxidation state, stannous oxide (SnO) was formed. Stannic tin oxide is a wide band gap semiconductor with a band gap of 3.6 eV [18, 33-34], whereas stannous tin oxide has a band gap of 2.5 - 3.0 eV. Stannic tin oxide has the rutile crystal structure and starts to crystallize at 450 °C, while the stannous form of tin oxide has the litharge structure. Stannic is the most common form of tin oxide and that the only form which is useful in gas sensing application. The density of tin oxide is 6.99 g/cm³ [34]. Stoichiometric SnO_2 is an insulator; however, oxygen vacancies render it to n-type semiconductor. The formation energy

of oxygen vacancies and tin interstitials was very low, so it was hard to deposited a stoichiometric film and most films turned out to be conductive [34].

Tin oxide (SnO_2) normally forms in the tetragonal rutile structure (space group $p4/mmm$) as illustrated in Figure 2.1. Its lattice parameters are included of $a = 0.4737$ nm, $c = 0.3186$ nm and $u = 0.306$ [35]. The large different in the value of electronegativity of Sn (1.96) and O (3.44) render it to be a strong ionic bonding. In the tetragonal structures, the tin (Sn) atoms were tetrahedrally coordinated to six oxygen (O) atoms.

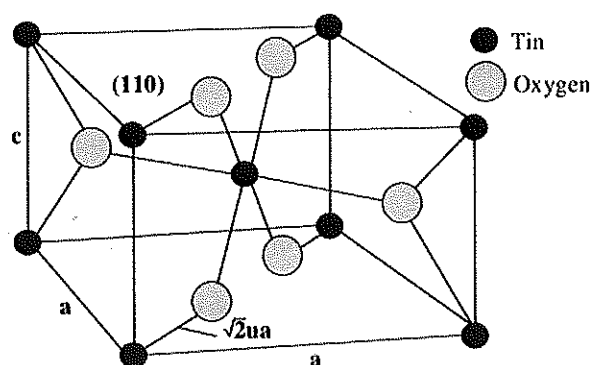


Figure 2.1 The primitive tetragonal unit cell of the bulk SnO_2 , with the basis of $(\text{SnO}_2)_2$.

The lattice parameters are $a = 0.4737$ nm, $c = 0.3186$ nm and $u = 0.306$ [35].

2.2 Thin film deposition methods

There are a number of methods used for deposition of undoped and (Fe or Sb)-doped SnO_2 films as presented in Table 2.1. These chemical methods comprised of gas phase and solution deposition methods. The gas phase methods included of sputtering [10], chemical vapor deposition (CVD) [11] and thermal evaporation [15], while dip coating [13, 25, 32], spin coating [12, 23-24] and spray pyrolysis [3, 5-6, 9, 14, 16-22, 26, 29-31, 36-38] methods employ solution precursor. The advantages and disadvantages of various methods for preparation of SnO_2 films were shown in Table 2.1.

Table 2.1 The advantages and disadvantages of various methods for prepared SnO₂ films

Deposition methods	Advantages	Disadvantages
Chemical vapor deposition (CVD)	- Smooth and uniform films surface	- Low deposition rate - Difficult to increase film thickness - High cost technique
Thermal evaporation	- Smooth and uniform films surface	- Low deposition rate - High cost technique
Sputtering	- Smooth and uniform films surface - High deposition rate - Easy to increase films thickness	- High cost technique
Dip coating	- Smooth and uniform films surface - Precursor solution is recyclable	- Difficult to increase films thickness and control precursor evaporation
Spin coating	- Smooth films surface - Easy to increase films thickness	- Limit in size of substrate - High cost technique
Spray pyrolysis	- Simple equipment - Easy to adding doping materials - High growth rate and easy to increase film thickness - Mass production capability for uniform large area coating - Low cost technique	- Rough films surface - Substrate should be durable for high temperature - Precursor unrecyclable - Difficult to control dust spray size - Easy to nozzle clogged

The spray pyrolysis is a low cost technique, simple and has major advantage of allowing deposition over area for industrial applications [19]. Using this method, dopants could be easily introduced into the matrix of the films by adding appropriate precursors. The precursors decomposed under suitable thermal treatment and the desired solid compound were form,

while the unwanted species were evaporated. In this work, the structural and optical properties of the undoped SnO_2 and (Fe or Sb)-doped SnO_2 thin films deposited by spray pyrolysis were presented.

2.3 Precursor and their concentrations

The type of the tin (Sn) precursors is one of the most important factors affecting the microstructure and in turns the films properties. X-ray diffraction measurements indicated that the SnO_2 films prepared from SnCl_4 presented a preferential growth along the (200) direction whereas the sample prepared from SnCl_2 , presented a preferentially along the (110) direction [39]. Moreover, SEM photographs of SnO_2 films suggested that the films derived from $\text{SnCl}_4 \cdot 5\text{H}_2\text{O}$ exhibited better surface morphology than those of films from $\text{SnCl}_2 \cdot 2\text{H}_2\text{O}$ [39]. The improved electrical and optical properties were obtained when $\text{SnCl}_4 \cdot 5\text{H}_2\text{O}$ was used as the starting material instead of $\text{SnCl}_2 \cdot 2\text{H}_2\text{O}$. Although $\text{SnCl}_2 \cdot 2\text{H}_2\text{O}$ is cheaper than $\text{SnCl}_4 \cdot 5\text{H}_2\text{O}$ and could be easily produced in a laboratory, $\text{SnCl}_4 \cdot 5\text{H}_2\text{O}$ is selected to prepare thin films in this thesis due to the superior film properties.

The undoped and (Fe or Sb)-doped SnO_2 thin films were deposited using different concentrations of precursor solution. It has been reported that the crystalline size increased with increasing precursor concentrations in the spray solution. SEM analysis suggested that the orientation of the grains was random, but the grain size increased with increasing concentrations of the precursor solution. The films were prepared by using pentahydrated stannic chloride ($\text{SnCl}_4 \cdot 5\text{H}_2\text{O}$) as a precursor, and the spraying solution with 0.01 M [21], 0.20 M [22] and 0.28 M [38] were used. The initial concentrations of the sprayed solution as 0.25 M of stannic chloride were used. This concentration was a good compromise between times of film deposition, influencing of the substrate cooling during the deposition process and possibility of thickness and growth rate control of SnO_2 film.

Doping the SnO_2 nanostructure with transition metals were primary means of controlling optical property and electrical conductivity of SnO_2 host semiconductors. Iron (Fe) and antimony (Sb) were selected to study effect of additives on the SnO_2 thin film properties.

The concentrations of Fe-doping were the important parameter for controlling SnO_2 films properties. Effect of Fe-doping concentrations (0 - 28.4 mol% in solution) on SnO_2 thin films properties deposited on the glass substrates using spray pyrolysis was investigated [21]. The precursor solution was prepared by dissolving a certain amount (0.01 M) of stannic chloride ($\text{SnCl}_4 \cdot 5\text{H}_2\text{O}$) and different amount of iron (III) chloride hexa hydrate ($\text{FeCl}_3 \cdot 6\text{H}_2\text{O}$) in 10 ml of solvent (a mixture of double distilled water and ethanol in a volume ratio 1:1). To enhance the solubility of stannic chloride, a few drops of HCl was also added to the solution. The weight percentage (wt%) of $\text{FeCl}_3 \cdot 6\text{H}_2\text{O}$ in the solution was changed from 0 to 10 wt% (or 0 to 28.4 mol% or atomic ratio of $(\text{Fe})/(\text{Sn}) = 0 - 40$ at%). The XRD patterns indicated that all films with different doping levels had polycrystalline SnO_2 (with tetragonal-cassiterite phase) and SnO phases. Increasing the doping levels increased the amorphous phase along with the reduction of peak intensities and increasing of the width that resulted in the mean crystalline size reduction. Also, in doping levels less than 19.1 mol%, XRD peaks intensity were stronger and this related to higher crystallinity of the films. The crystalline sizes of films decreased from 60 - 80 nm (for undoped SnO_2 films) down to 25 - 45 nm in 19.1 mol% doping level. The average transmittance of the films decreased from about 90% to 70% when the doping level increased from 0 mol% to 19.1 mol% (or 0 at% to 23.6 at% in solution). Thus, Fe-doping levels at 6, 12 and 18 mol% were investigated in this thesis in order to keeping optical transparency and controlling amorphous background of films.

In addition to Fe, the literature survey revealed that very recently, there have been studies on the properties of antimony doped SnO_2 films [4, 11, 26-28, 30-32, 38]. From previous study [38], pure and antimony doped tin oxide films were deposited on both glass and quartz plates by spray pyrolysis method. The substrate temperatures was varied in the range of 300 - 450 °C and the doping varied from 0 to 10.7 mol% in solution (or 0 to 12 at% of $(\text{Sb})/(\text{Sn})$) and their effects on the structural, optical and electrical properties were studied. It was found that 8.3 mol% (or 9 at%) was the optimum doping level and the best electro-optic properties were obtained; resistivity as low as $9 \times 10^{-4} \Omega \cdot \text{cm}$ and the average transmission of 80% in the visible region, at the substrate temperature of 400 °C. Moreover, when doping with Sb change in preferred orientation was observed from (110) to (200). The optical investigation showed that, depending upon the doping concentrations, the antimony doped films had direct allowed

transitions in the range 4.13 - 4.22 eV and indirect allowed transitions in the range 2.54 - 2.65 eV, respectively [38].

SbCl_3 was used as dopant source for Sb-doping because of its low cost [27-28, 30-31]. The XRD analysis showed that the undoped SnO_2 films had (211) preferred orientation whereas the Sb-doped films had (200) plane [27].

Scanning electron microscopy studies indicated that the surfaces of the films prepared with lower doping level (1 mol%) consisted of larger grains whereas those prepared with higher doping levels (> 1 mol%) consisted of smaller grains. Some researchers [27-29] reported that ATO films showed a preferential growth along the (200) direction. However, Ma et al. [4] found that the preferred orientation was (110) direction. In this thesis, SbCl_3 was used a dopant source of Sb-doping for preparation of Sb-doped SnO_2 films.

2.4 Solvent for spray pyrolysis

The precursor solution was prepared by dissolving a certain amount of stannic chloride ($\text{SnCl}_4 \cdot 5\text{H}_2\text{O}$) and different amounts of dopant in a mixture of double distilled water and ethanol in a volume ratio of 1 : 1 [21]. To enhance the solubility of stannic chloride and dopant, HCl was also added to the solution [21, 38, 40]. However, Smith et al. [40] and Shanti et al. [38] have shown that the preferred orientation was (110) with low amount of HCl in the starting solution (< 0.2 mol/l). Thus, a mixture of 90 ml of ethanol, 10 ml of double distilled water and 4 ml of HCl (in the starting solution was 0.5 mol/l) was selected to prepare the SnO_2 films by spray pyrolysis in this thesis.

2.5 Deposition temperature for spray pyrolysis

The effects of the deposition temperature on the structural, optical, morphological and electrical properties of undoped SnO_2 films prepared by spray deposition method were investigated [17]. The X-ray diffraction patterns for undoped SnO_2 films deposited at 300, 350, 400, 450 and 500 $^{\circ}\text{C}$ indicated that films deposited at 300 $^{\circ}\text{C}$ were nearly amorphous whereas the increase of deposition temperature above 350 $^{\circ}\text{C}$ caused the increase of crystallization of the films. The films deposited at 350 $^{\circ}\text{C}$ showed only three peaks namely (200), (211) and (301)

whereas the films deposited at higher temperatures showed as many as five peaks such as (110), (101), (200), (211) and (301), respectively. Thin films deposited at 350, 400, 450 and 500 °C showed sharp XRD peaks, indicating to polycrystalline and cassiterite tetragonal structure. In all films, the half width of the Bragg peaks decreased and the intensity of the peak increased with increasing deposition temperature. Especially, the peaks (110) and (211) dominantly increased with the increase of deposition temperatures. It was also observed by XRD analysis that, the crystallinity of the films was improved, the crystalline size became larger, and the degree of surface roughness increased with increasing substrate temperatures.

In addition, Shanti et al. [38] prepared pure and Sb-doped SnO₂ films by spray pyrolysis method using substrate temperatures in the range of 300 - 450 °C. It was observed that, from the XRD patterns, the preferred orientation changed from (110) to (200) with Sb-doping and (200) peak intensity was maximum at 400 °C substrate temperature. This was indicated that Sb has also gone into the interstitial sites of Sn atoms in SnO₂ lattice structure and 400 °C substrate temperature has been found to be optimum substrate temperature. Moreover, the deposition temperature over 500 °C was not suitable due to limit of glass substrate annealing temperature (546 °C). Thus, 400 °C was selected to be a deposition temperature for preparation of thin films by spray pyrolysis in this thesis.

CHAPTER 3

EXPERIMENTAL

3.1 Chemicals and instruments

All the chemicals used in this thesis were analytical grade as shown in Table 3.1.

Table 3.1 Chemicals

Chemicals	Formula	Assay (%)	Manufacturer
Tin (IV) chloride pentahydrate	$\text{SnCl}_4 \cdot 5\text{H}_2\text{O}$	98.0 %	Sigma Aldrich
Iron (III) Chloride	FeCl_3	97.0 %	Sigma Aldrich
Antimony (III) Chloride	SbCl_3	99.9 %	Sigma Aldrich
Ethyl alcohol	$\text{CH}_3\text{CH}_2\text{OH}$	99.9 %	Merck
Hydrochloric acid	HCl	37.0 %	Carlo Erba
Nitric acid	HNO_3	69.0 %	AnalaR

The details of instruments for thin film characterization were listed in Table 3.2.

Table 3.2 Instruments

Instruments	Model	Company
X-ray Diffractometer (XRD)	Philips X 'pert MPD	Philips
Scanning Electron Microscope (SEM)	JSM 5410-LV	JEOL
Atomic Force Microscope (AFM)	XE-100	PARK
Fourier Transform Infrared Spectrometer (FT-IR)	Spectrum RX 1	Perkin Elmer
Fluorescence Spectrometer	LS-55	Perkin Elmer
UV-Visible Spectrometer	Lambda 25	Perkin Elmer

3.2 Experimental

The undoped and metals (Fe or Sb)-doped SnO_2 thin films were deposited on the glass substrates by home-made spray pyrolysis experimental set-up. Optical microslide glass plates with an effective area of 7.5 x 2.5 cm were used as substrates. The glass substrates were cleaned with HNO_3 : HCl (1 : 3) cleaning solution, rinsed with ethanol in an ultrasonic bath and heated at 500 °C for 1 hour before spraying. The precursor solution was prepared by dissolving 8.75 g (0.025 mol) of $\text{SnCl}_4 \cdot 5\text{H}_2\text{O}$ in the mixed solvent of $\text{C}_2\text{H}_5\text{OH}/\text{H}_2\text{O}/\text{HCl}$ 90 : 10 : 4 (v/v/v) [38]. Different doping levels were prepared by varying the metal salts (FeCl_3 or SbCl_3) content in the spray solution. The SnO_2 films were deposited by spraying solutions at various doping concentrations of dopants as 0, 6.0, 12.0 and 18.0 mol%, respectively in the separated sets of experiment. The substrate temperature was kept constantly at 400 ± 10 °C. The flow rate of solution (3.0 ml/min) was controlled by compressed air at a carried air pressure of 0.2 kg/cm². The normalized distance between the spray nozzle and the substrate was 60 cm and 15 ml of starting solution was used for spraying in each case.

3.3 Characterization techniques

The structural and optical properties were characterized by XRD, SEM, AFM, FT-IR, Fluorescence and UV-Visible spectrometric methods. The details of methods were presented in section 3.3.1 - 3.3.6.

3.3.1 X-ray Diffraction (XRD)

The X-ray diffraction studies were carried out using X-ray diffractometer (Philips X 'pert MPD, $\text{Cu K}\alpha$ radiation wavelength 0.154 nm) to investigate the structure of the deposited films. The scanning range of 2θ was restricted to the range of 20 - 60° with scan rate of 0.02 °/s.

The average crystalline size was calculated using the Scherrer's formula (in equation 3.1) based on the XRD patterns [41].

$$D = \frac{k\lambda}{\beta \cos \theta} \quad (3.1)$$

where; D is the average crystalline size

k is the Scherrer's constant, (in this case, it is assumed to be 0.9)

λ is the wavelength of X-ray (0.15406 nm)

β is Full-Width-Half-Maxima (FWHM) of the peak (in radians)

θ is the Bragg's angle (in radians).

The lattice strain (ϵ) induced in films due to crystal imperfection and distortion was calculated using the equation 3.2:

$$\epsilon = \frac{\beta_{hkl}}{4 \tan \theta} \quad (3.2)$$

where; ϵ is lattice strain

β_{hkl} is Full-Width-Half-Maxima (FWHM) of the (211) peak (in radians)

θ is the Bragg's angle (in radians).

The lattice distance (d), lattice parameters (a-axis, c-axis) and cell volume (v) of thin films could be also calculated according to the equation 3.3 - 3.6, respectively [42-43].

$$d_{hkl} = \frac{\lambda}{2 \sin \theta} \quad (3.3)$$

$$a = \frac{\lambda \sqrt{S}}{2 \sin \theta} \quad (3.4)$$

$$c = \frac{1}{\sqrt{\frac{1}{d_{(101)}^2} - \frac{1}{2d_{(110)}^2}}} \quad (3.5)$$

$$V = a^2 c \quad (3.6)$$

where; d is the lattice distance at hkl

(h, k, l) are Miller indices of XRD plane

S is summation of $h^2 + k^2 + l^2$

a and c are lattice parameters

λ is wavelength of X-ray (0.15406 nm)

θ is Bragg's angle (in radians)

V is cell volume of tetragonal unit cell.

The tetragonality (c/a) could be determined by following equation:

$$\text{Tetragonality} = \frac{c}{a} \quad (3.7)$$

where; a and c are lattice constants and could be calculated from the XRD patterns.

3.3.2 Scanning Electron Microscopy (SEM)

The surface morphology in microstructure of deposited films was examined by scanning electron microscope (SEM; JEOL JSM-5410 LV). The SEM was operated at 25 kV and magnification at 10,000 in the vacuum atmosphere. The samples were coated with gold by sputtering technique before measurement.

3.3.3 Atomic Force Microscopy (AFM)

Atomic force microscopy (AFM) is one of the microscopic techniques. Small sample was usually mounted on some sort of piezoelectric scanner. A probe tip was then brought into extremely closed proximity to the sample surface, the sample was then scanned laterally, and usually the strength of the feedback signal (or error or some other quantity) was monitored as a function of x , y positions. AFM could be done with a number of modes and variations, i.e. contact, tapping and noncontact modes to manipulate individual atom such as tin oxide nanocrystal. In this thesis, surface morphology of SnO_2 films were investigated by atomic force microscopy (AFM; Park, XE - 100) with operated in non-contact mode on a scanning area of $1 \mu\text{m} \times 1 \mu\text{m}$ with scan rate as 0.50 Hz on XY direction and slow scan reverse system. The average grain size and root mean square (RMS) values of surface roughness were estimated for study the effect of dopant and their concentrations on the surface morphology of SnO_2 films.

The root mean square (RMS) of films could be calculated according to the equation 3.8 [44].

$$R_{\text{RMS}} = \sqrt{\frac{\sum_{i=1}^N (Z_i - \bar{Z})^2}{N}} \quad (3.8)$$

where; R_{RMS} is root mean square

N is total number of data points

Z_i is vertical coordinate of the image

\bar{Z} is mean value of Z_i .

3.3.4 Fourier Transform Infrared Spectroscopy (FT-IR)

Fourier transform infrared spectroscopy (FT-IR) gives information about functional groups present in a compound along with the molecular geometry and inter or intra molecular interactions. The powder scratched from deposited film was characterized by fourier transform infrared (FT-IR) spectroscopy using Perkin Elmer FT-IR spectrometer model spectrum RX1. The FT-IR spectra were measure from samples prepared by KBr pallet technique (KBr : sample ratio, 300 : 1) in the wavenumber ranges of 400 - 1500 cm^{-1} .

3.3.5 Fluorescence Spectroscopy

Room temperature photoluminescence (PL) measurements were performed with a Perkin-Elmer LS - 55 fluorescence spectrometer recording spectra in the range of 300 – 400 nm using excitation line at 215 nm, excitation slit 6.0, emission slit 3.0 and scan speed 500 nm/min, respectively. The photoluminescence spectra of the prepared thin films on glass substrates were directly measured under the above mentioned condition.

3.3.6 UV-Visible Spectroscopy

The optical absorption and transparency studies were performed in the wavelength range of 300 - 1,100 nm using Lambda 25 UV - Vis double beam spectrophotometer with scan speed 960 nm/min. The thickness of films (t) were determined by using the optical transmission spectra (%T) and the following equation [21]:

$$t = \frac{\lambda_1 \lambda_2}{2\eta (\lambda_1 - \lambda_2)} \quad (3.9)$$

where; λ_1 and λ_2 are two consecutive peaks in transmission spectra

η is refractive index of SnO_2 ($\eta = 1.95$).

From optical absorption measurements, the direct optical band gap (E_g) for various of SnO_2 thin films doping with Fe- and Sb-doping levels were obtained by plotting $(\alpha h\nu)^2$ versus photon energy ($h\nu$) and using the following relation [21]:

$$(\alpha h\nu)^2 = A (h\nu - E_g) \quad (3.10)$$

where; α is absorption coefficient

A is constant

E_g is direct band gap of the materials

$h\nu$ is photon energy.

CHAPTER 4

RESULTS AND DISCUSSION

Several characterization techniques were used to study the prepared thin films; like XRD, SEM, AFM, FT-IR, Fluorescence Spectroscopy and UV-Visible Spectroscopy. An attempt has been made to correlate of the structural and optical properties of these films with the dopants and their concentrations. The results of structural and optical properties of films were characterized and discussed in the following sections.

4.1 Structural analysis of undoped and (Fe or Sb)-doped tin oxide films

The X-ray diffraction patterns of Fe-doped SnO_2 and Sb-doped SnO_2 thin films in various doping levels of 0, 6, 12, 18 and 100 mol% in spray solution were shown in Figure 4.1 and 4.2, respectively. As shown in Figure 4.1a, the XRD pattern of undoped SnO_2 illustrated (110), (101), (200) and (211) orientated growth at 2θ as 26.8° , 34.1° , 38.3° and 52.0° , respectively. The XRD pattern of the SnO_2 indicated that the undoped film was tetragonal rutile structure with the lattice constants as $a = b = 0.4711$ nm and $c = 0.3174$ nm, which corresponded with the data of SnO_2 powders record in the JCPDS document (Powder Diffraction File Compiled by the Joint Committee on Powder Diffraction, 1985, Card No. 03-1116). No diffraction peaks corresponding to Sn or other impurities were detected within the limits of experimental error. The broad hump at 2θ between 20° and 30° was the background intensity due to amorphous of glass substrate [30].

The XRD patterns of Fe-doped SnO_2 films were deposited by spraying solutions at various doping concentrations of Fe as 6, 12 and 18 mol%, as presented in Figure 4.1b - d, respectively. Most of them were exhibited the tetragonal rutile structure of polycrystalline SnO_2 with the same prefer orientation (the (200) plane), except Fe-doping at 18 mol%. However, for 18 mol% Fe-doping (Figure 4.1d), it could be seen that no diffraction peaks corresponding to the tetragonal rutile structure of crystalline SnO_2 or SnO were observed. Moreover, there exist another phase which was different from the known phase in undoped films (see Figure 4.1a and 4.1e). The different diffraction pattern of 18 mol% Fe-doping compared with undoped SnO_2 was

The different diffraction pattern of 18 mol% Fe-doping compared with undoped SnO₂ was expected to the distortion in the structure of tetragonal SnO₂ due to high Fe-doping levels. The XRD pattern of Sb-doped SnO₂ films were compared in Figure 4.2. All cases of Sb-doped SnO₂ films with 6, 12 and 18 mol% doping presented the tetragonal rutile structure of polycrystalline SnO₂, which different preferred orientation compared to undoped films (Figure 4.2a). According to the XRD analysis results in Figure 4.1 and 4.2, the aim of the present work was to study the effect of dopants and their concentrations on the structural and optical properties of the system (Fe or Sb)-doped SnO₂ films. The XRD results for these concentrations were summarized in Table 4.1.

Table 4.1 Summary of XRD parameters for different dopants and various doping concentrations

XRD parameter	Dopants concentrations (mol%)						
	SnO ₂	Fe-doping			Sb-doping		
	0	6	12	18*	6	12	18
Preferred orientation	211	200	200	-	200	110	110
2 θ change (%)**	0.00	0.73	0.97	-	- 0.15	0.17	0.42
FWHM (degree)***	0.351	1.047	1.137	-	0.394	1.089	1.464
Intensity (Cps)***	220	52	39	-	109	81	61
Strain***	0.0031	0.0094	0.0102	-	0.0035	0.0098	0.0131
Crystalline size (nm)***	25.19	9.81	8.50	-	22.50	8.71	6.22
Lattice parameter: a (nm)	0.4711	0.4775	0.4852	-	0.4717	0.4703	0.4692
Lattice parameter: c (nm)	0.3174	0.3127	0.3090	-	0.3183	0.3180	0.3173
Unit cell volume (nm ³)	0.0704	0.0713	0.0727	-	0.0708	0.0703	0.0699
Tetragonality (c/a)	0.6737	0.6549	0.6369	-	0.6748	0.6762	0.6763

*All parameters of Fe-doped SnO₂ 18 mol% not calculated due to XRD plane of SnO₂ rutile tetragonal phase were not detected

$$**2\theta \text{ change (\%)} \text{ of preferred orientation} = 100 \times \left(\frac{2\theta_{\text{doped film}} - 2\theta_{\text{undoped film}}}{2\theta_{\text{undoped film}}} \right)$$

***The FWHM, intensity, strain, and crystalline sizes have been calculated from the (211) plane.

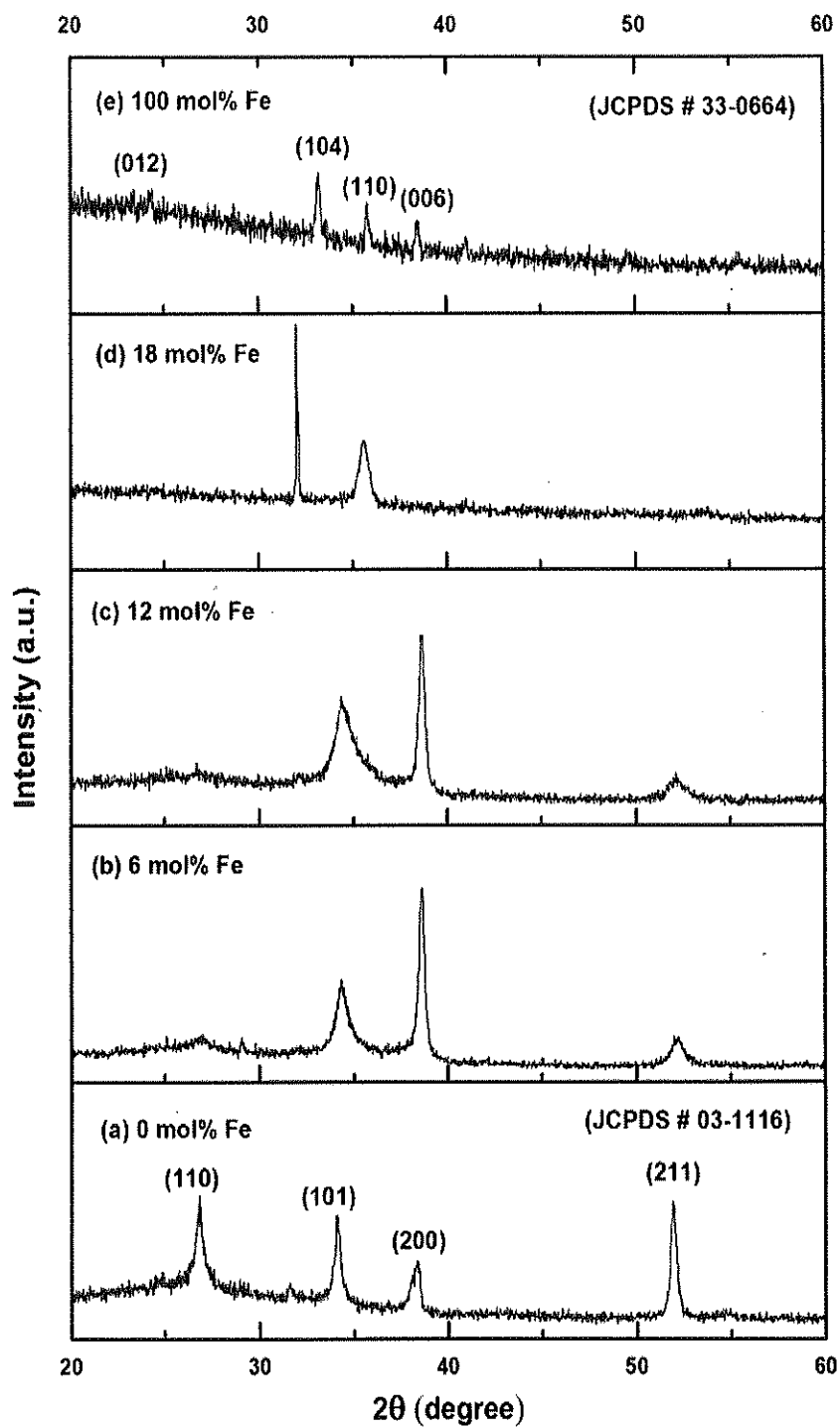


Figure 4.1 X-ray diffraction patterns of Fe-doped SnO₂ thin films for various doping levels: 0, 6, 12, 18 and 100 mol%.

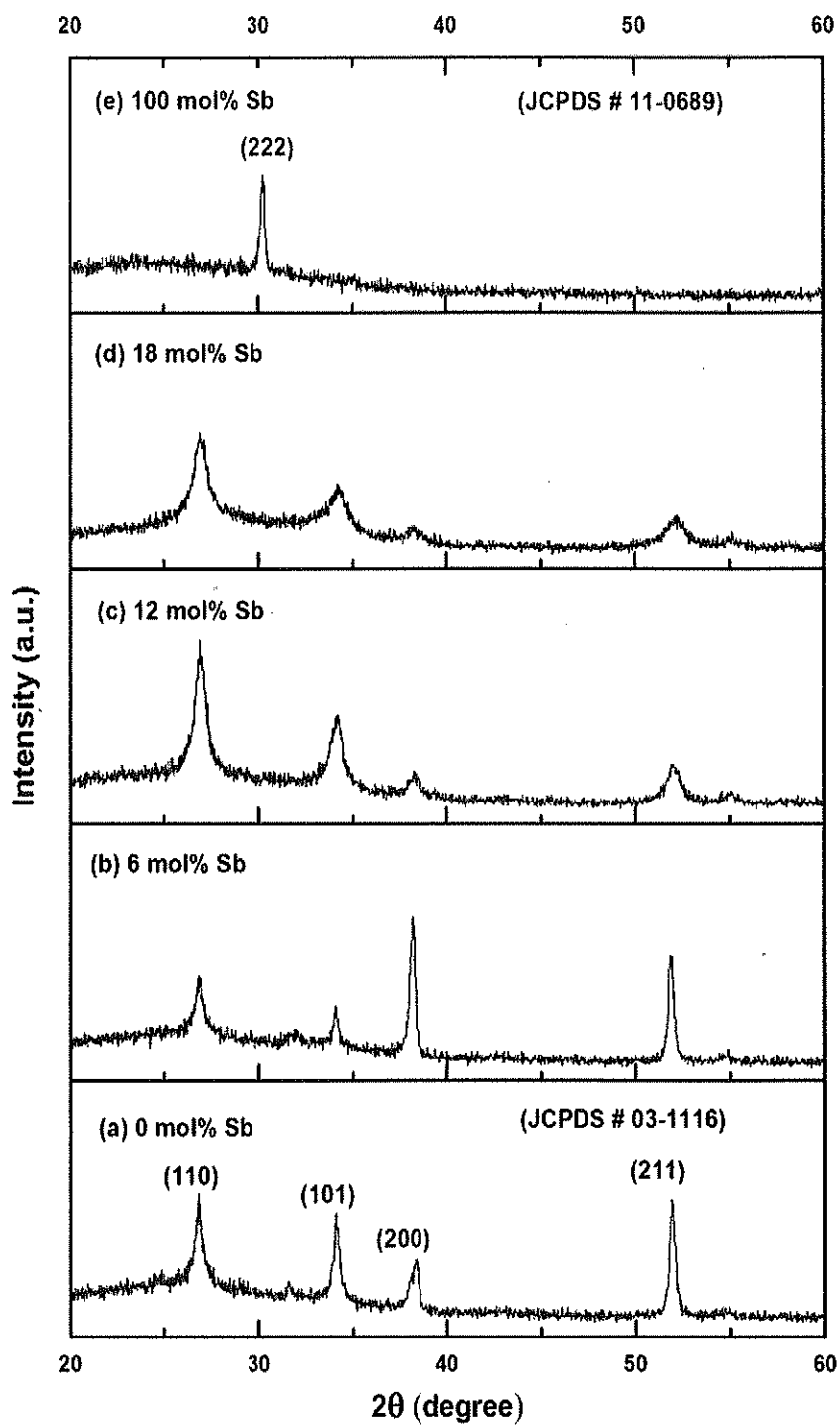


Figure 4.2 X-ray diffraction patterns of Sb-doped SnO₂ thin films for various doping levels: 0, 6, 12, 18 and 100 mol%.

The preferred orientation of the X-ray diffraction patterns of (Fe or Sb)-doped SnO_2 were illustrated in Table 4.1. The XRD analysis showed that a preferred (211) orientation was observed for the undoped SnO_2 thin films. In Fe-doping case, the Fe-doped films grew in (200) plane both 6 and 12 mol% Fe-doping. All of them exhibited a preferred orientation growth along the (200) direction which was not agreement with the results obtained by some researchers [21, 23-25], in which the XRD patterns of Fe-doped SnO_2 films exhibited peaks corresponding to the rutile structure of polycrystalline SnO_2 with the maximum intensity peak from (110) planes with high deposition temperature (500 - 800 °C). However, for 18 mol% Fe-doping, no diffraction peaks corresponding to the tetragonal rutile structure of SnO_2 were observed. Moreover, the apparent diffraction peaks were not corresponded to Fe_2O_3 film (Figure 4.1e). It was assumed that, the different diffraction pattern between 18 mol% Fe-doping and undoped SnO_2 was assumed to the high distortion of lattice structure due to substitution of Sn atoms by Fe atoms in SnO_2 lattice. From this, at low Fe-doping levels (6 - 12 mol%), Sn atoms were replaced by Fe atoms and affected to distortion of lattice in SnO_2 lattice structure due to lattice mismatch. At high Fe-doping level (18 mol%), the substitution of Sn atoms by Fe atoms were increased, resulted to changing to different XRD pattern peaks at 18 mol% Fe-doping.

As the Sb-doping concentrations were increased, a preferred (200) orientation was appeared for 6 mol% Sb-doped films, while the reflection intensity for plane (110) was very prominent with the antimony concentrations of 12 mol% Sb-doping. The Sb-doped SnO_2 films showed a preferential growth along the (200) direction, agreement with the results obtained by some researchers [27-29]. While the 12 and 18 mol% Sb-doping also indicated that a (110) preferred orientation was agreed with the films prepared by r. f. magnetron sputtering technique [4]. However, the diffraction patterns of 18 mol% Sb-doping still corresponded to the tetragonal rutile structure. The results were agreed with the tetragonality of Fe-doped SnO_2 , which was higher than that of Sb-doping (Table 4.1). The results indicated that, Fe-doping was more influencing on the structural distortion of SnO_2 than that of Sb-doping.

For Fe- or Sb-doped SnO_2 , the 2θ values in XRD patterns of the SnO_2 phase were shifted to lower or higher value, indicating that Fe or Sb was incorporated into Sn sites in SnO_2 lattice. If a change in the 2θ values became lower value, the crystal radius of host was smaller than that of a dopant. In contrast, if a change in the 2θ values became higher value, the crystal radius of

host was bigger than that of a dopant. A change in the 2θ values as a function of dopant and their concentrations were illustrated in Table 4.1. It was observed that, the 2θ percentage change of Fe-doped SnO_2 for 6 and 12 mol% Fe-doping as 0.73% and 0.97 %, respectively. From changing in the 2θ values of SnO_2 peak to higher value of 2θ , the tin crystal radius was indicated bigger grain size than that of the iron crystal. The Shannon - Prewitt crystal radius (CN = 6) of Sn^{4+} , Fe^{3+} and Fe^{2+} were 83, 69 and 75 pm, respectively [45]. Sn^{4+} crystal radius was greater than both Fe^{3+} and Fe^{2+} , resulted to the peak shifting to higher angle side, which was good agreement with the results obtained by XRD patterns as shown in Table 4.1. In the Sb-doping case, the 2θ percentage change for 6 mol% Sb-doping was -0.15%, whereas the 2θ values of peak from (110) plane with 12 and 18 mol% Sb-doping was increased as 0.17% and 0.42%, respectively. The Shannon - Prewitt crystal radius (CN = 6) of Sn^{4+} , Sb^{3+} and Sb^{5+} were 83, 90 and 74 pm, respectively. Sb^{3+} crystal radius was greater than that of Sn^{4+} resulting to peak shifting to lower angle side, which indicated that Sb^{3+} was incorporated to SnO_2 lattice structure at 6 mol% Sb-doping. In contrast, the crystal radius of Sb^{5+} was smaller than that of Sn^{4+} relating to change of 2θ percentage to higher value, which indicated that Sn^{4+} was substituted by Sb^{5+} in SnO_2 lattice sites at 12 and 18 mol% Sb-doping. Therefore, a part of Sn^{4+} in SnO_2 lattice sites were replaced by Sb^{5+} and Sb^{3+} with 6, 12 and 18 mol% Sb-doping. This observation was good agreement with the Shannon - Prewitt crystal radius.

From Table 4.1 and Figure 4.3, the full width at half maxima (FWHM) at (211) plane of SnO_2 thin films for different dopants and various doping levels were investigated. The FWHM values of tin oxide doped with Fe at 6 and 12 mol% were 1.047° and 1.137° , whereas Sb-doping at 6 and 12 mol% were 0.394° and 1.089° , respectively. The FWHM of thin films were slightly increased with increased of doping concentrations compared with SnO_2 (0.351°). The increased in FWHM along with increasing of doping level were suggested that dopant incorporation into the SnO_2 lattice resulted in a reduction of crystallinity of thin films. Moreover, FWHM of Fe-doped SnO_2 thin films were higher than that of Sb-doping at the same doping concentrations. This indicated that Fe-doping was influenced on the crystallinity of thin films more than that of Sb-doping.

The presence of compressive strain was also supported by observed reduction of the unit cell volume in Sb-doped SnO_2 films (Table 4.1). This was signified a compressive strain in

a lattice attributed to mismatch of Shannon - Prewitt crystal radius of Sb^{3+} ions (90 pm) and Sb^{5+} ions (74 pm) compared to Sn^{4+} ions (83 pm). In addition, the values of unit cell volume and corresponding lattice strain of Sb-doped SnO_2 films were also shown in Table 4.1. As shown, lattice strain of 6, 12 and 18 mol% Sb were higher than that of SnO_2 . Furthermore, the unit cell volume of Sb-doped SnO_2 films was tend to decrease but increase with Fe-doping. For Fe-doping, the observed increase in the unit cell volume may arise from the possible introduction to iron-ions into both substitutional and interstitial lattice sites. It can be inferred that, both iron and antimony were incorporated into the SnO_2 lattice. Moreover, strain values of Sb-doped SnO_2 were higher than that of Fe-doping at the same doping level. This indicated that Sb-doping was influencing on the compressive of lattice strain in SnO_2 lattice structure more than that of Fe-doping.

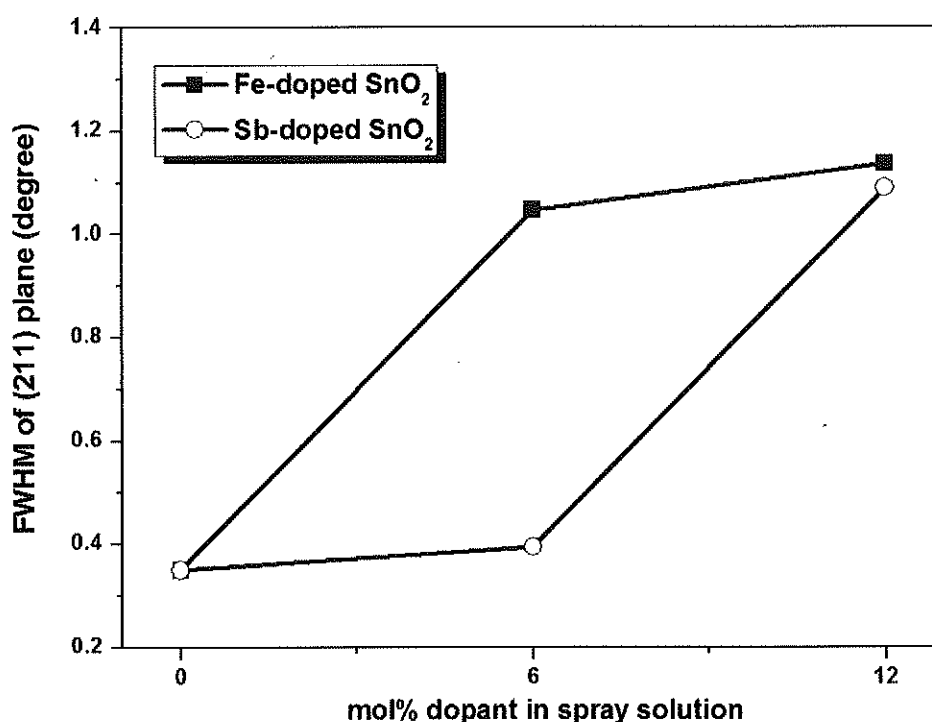


Figure 4.3 FWHM of (211) orientation for thin films at various dopant as a function of mol% doping concentrations in spray solution.

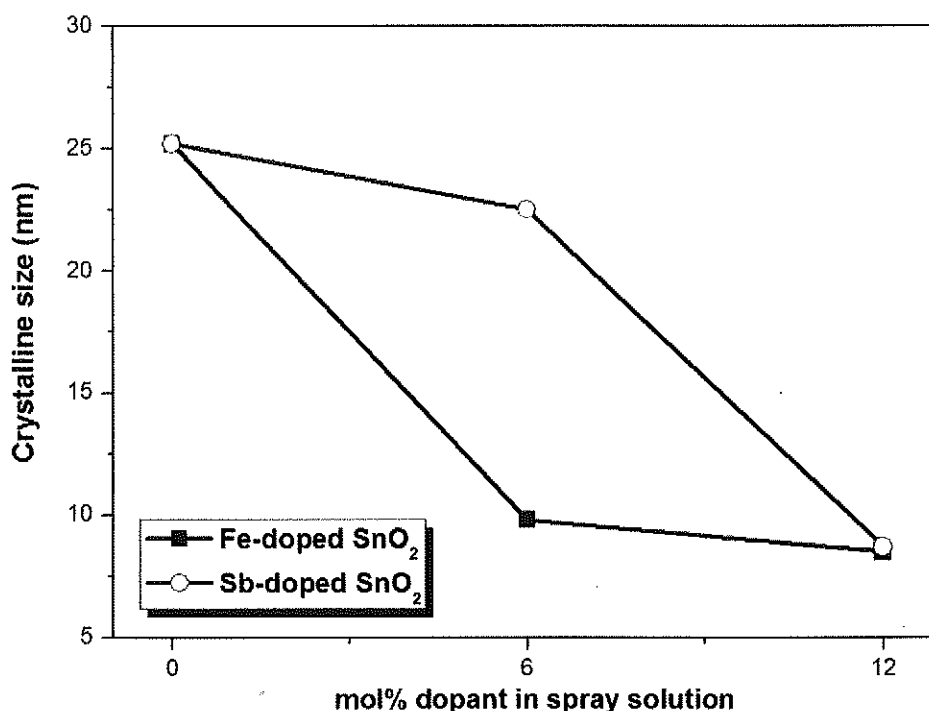


Figure 4.4 Crystalline size for thin films at various dopant as a function of mol% doping concentrations in spray solution.

The crystalline sizes for thin films at various dopants as a function of mol% doping concentrations in spray solution were calculated from Sherrer's equation as shown in Figure 4.4. As shown, the crystalline sizes of tin oxide doped with Fe at 6 and 12 mol% were 9.81 nm and 8.50 nm, whereas Sb-doping were 22.50 nm and 8.71 nm, respectively. The crystalline sizes tended to decrease with increasing Fe and Sb content compared with SnO_2 (25.19 nm). The increasing of Sb or Fe atoms incorporated in SnO_2 host matrix led to crystalline growth suppression, resulting in reduction of crystalline sizes. Moreover, the crystalline sizes of Fe-doped SnO_2 were lower than that of Sb-doping at the same doping level. This indicated that Fe-doping was influenced on the reduction of crystalline sizes more than that of Sb-doping.

For doped SnO_2 films with high Fe- or Sb-doping concentrations, the weak diffraction peaks of SnO_2 could be detected, as shown in Figure 4.1 and 4.2. At low doping concentrations, dopant ions were incorporated into the SnO_2 crystal structure to form a solid solution. At high doping concentrations, impurity phases such as Fe_2O_3 or Sb_2O_3 could be segregated in the surface or grain boundary of SnO_2 under annealing condition. However, no diffraction peaks corresponding to impurity phases were detected within the limit of experimental error.

As dopant ions were incorporated in to SnO_2 lattice, the tetragonal distortion could be induced. The variations of their tetragonality as a function of different doping concentrations were listed in Table 4.1 and the data also presented in graphs as shown in Figure 4.5. The tetragonality (c/a) of Fe-doped SnO_2 films were decreased sharply and lower than those of Sb-doping at the same doping concentrations. The solid solution limit of Sb ions in SnO_2 films could be lower than that of Fe ions. The tetragonality (c/a) of Fe-doped SnO_2 films remarkably decreased with increasing Fe content, which was in agreement with the smaller size both of Fe^{3+} (69 pm) and Fe^{2+} (75 pm) compared to Sn^{4+} (83 pm). At the same condition, the tetragonality (c/a) of Sb-doped SnO_2 films slightly increased with increasing Sb-doping, which indicated that a part of Sn^{4+} in SnO_2 lattice sites were replaced by Sb^{3+} (90 pm) and Sb^{5+} (74 pm). A small amount of secondary phases with disoriented distribution may be insufficient to form adequate sharp to be detected by XRD patterns because the XRD peak was only sensitive to long - range crystalline order. Therefore, the segregated impurities cannot be detected in XRD patterns of SnO_2 films probably due to the limited resolution of our XRD instrument as well as amorphous structure of the impurities.

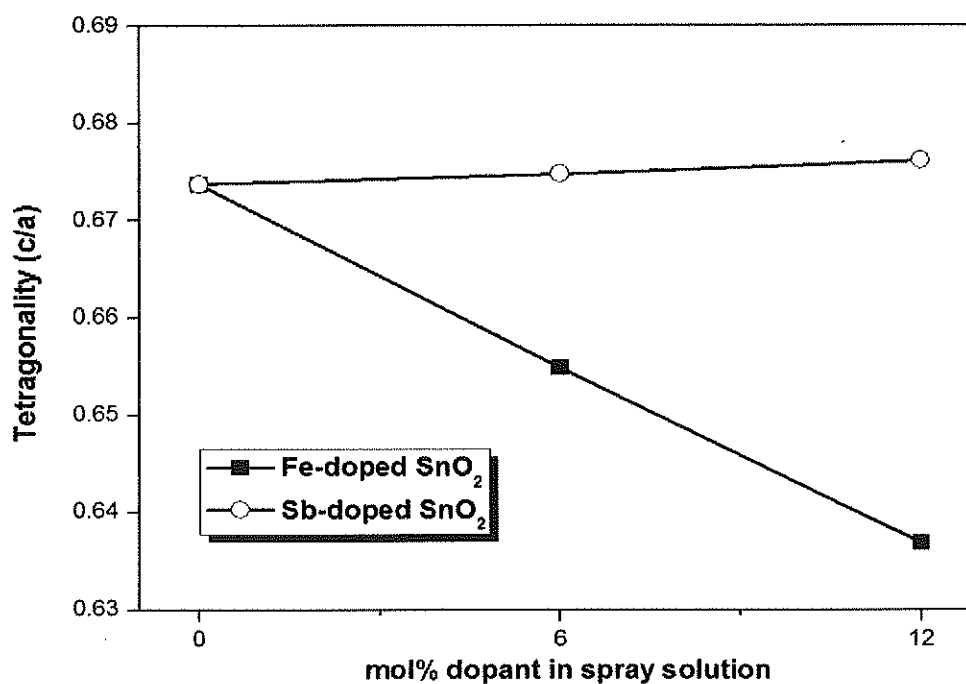


Figure 4.5 Tetragonality (c/a) for thin films at various dopant as a function of mol% doping concentrations in spray solution.

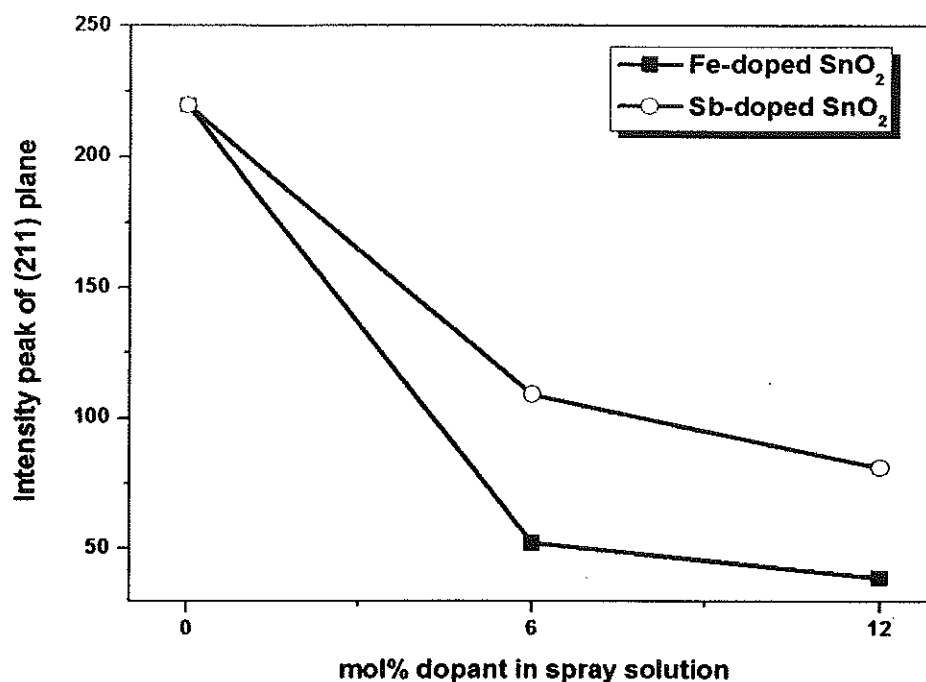


Figure 4.6 XRD peak intensity of (211) orientation for thin films at various dopant as a function of mol% doping concentrations in spray solution.

In addition, the XRD peak intensity was reduced obviously and the full width at half - maximum (FWHM) increased with the increase of dopant concentrations, indicating that the crystalline quality of the films was very sensitive to the addition of dopants. The preferred orientation of (211) was observed for the undoped SnO₂ thin films. The XRD peak intensity of the samples at (211) orientation with different dopant concentrations were presented in Figure 4.6. It was also indicated that the peak intensity of Fe-doping with increasing doping level were reduced more than that of the Sb-doping, which was good agreement with the tetragonality of films.

4.2 Surface morphology studies of undoped and (Fe or Sb)-doped tin oxide films

4.2.1 Surface morphology studies of undoped and (Fe or Sb)-doped tin oxide films by SEM

The SEM micrographs of undoped SnO₂, Fe-doped SnO₂ and Sb-doped SnO₂ thin films for different doping levels (6, 12 and 18 mol%) were shown in Figure 4.7 and 4.8,

respectively. The surface morphologies of the SnO_2 films were strongly depend on the doping concentrations.

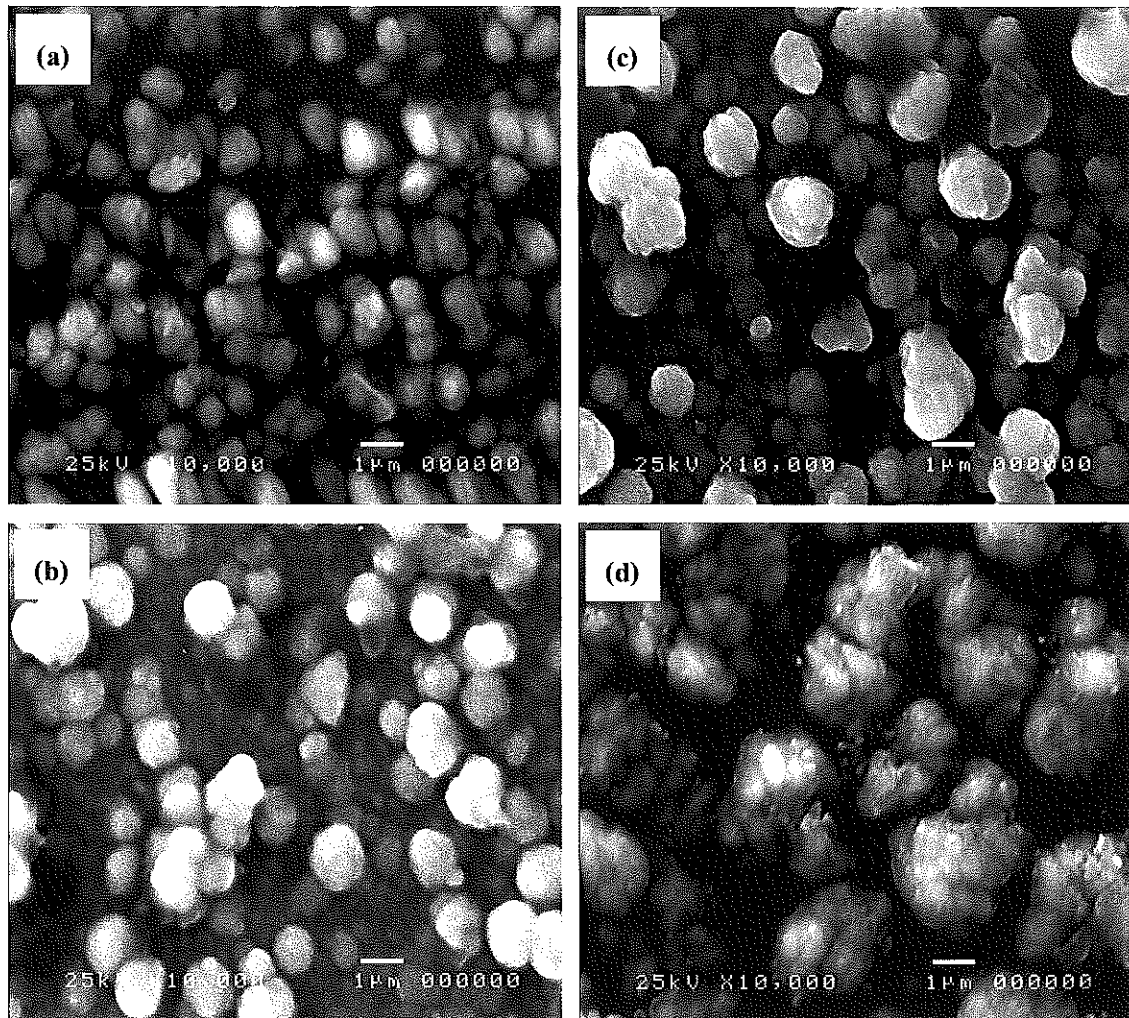


Figure 4.7 SEM micrographs of SnO_2 thin films for different dopants and various doping levels:

- (a) undoped SnO_2 , (b) Fe-doped SnO_2 6 mol%, (c) Fe-doped SnO_2 12 mol% and (d) Fe-doped SnO_2 18 mol%.

As seen, the SnO_2 films (Figure 4.7 a and 4.8 a) have the fine distribution of spherical shaped grains and almost uniform [27]. In Fe-doped SnO_2 films (Figure 4.7 b - d), the bigger round shaped grains, surrounded by a small grains were appeared on the films surface. The numbers of bigger grains were increased with increasing of Fe-doping concentrations. At 18 mol% Fe-doping (Figure 4.7 d), the agglomerated grains from small grains to bigger grains

were appeared. For Sb-doping (Figure 4.8 b - d), the grain sizes were decreased with increased of Sb contents and increased again at 18 mol% Sb-doping.

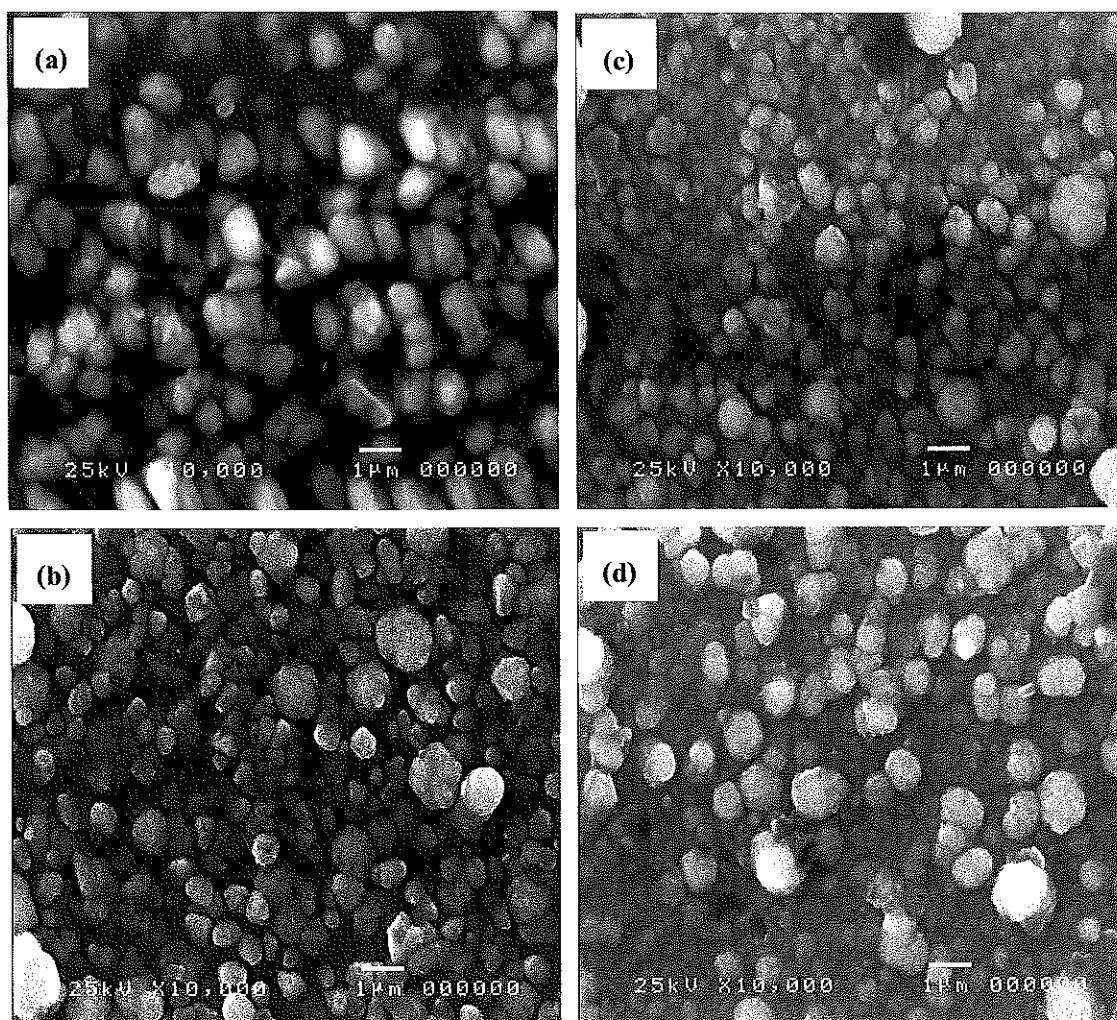


Figure 4.8 SEM micrographs of SnO_2 thin films for different dopants and various doping levels:

(a) undoped SnO_2 , (b) Sb-doped SnO_2 6 mol%, (c) Sb-doped SnO_2 12 mol% and (d) Sb-doped SnO_2 18 mol%.

The approximately average grain size of Fe- and Sb-doped SnO_2 were shown in Table 4.2 and Figure 4.9. As seen in Table 4.2, approximately average grain size of Fe-doped SnO_2 at 6, 12 and 18 mol% were about 1,436 nm, 1,780 nm and 2,700 nm, respectively. The approximately average grain sizes were increased with increasing of Fe-doping levels. The concentration of Fe-doping influenced on surface morphology with grain growth promotion in

films and more effective at higher doping concentrations due to grain segregation was increased along with increasing of Fe contents.

The approximately average grain size of Sb-doped SnO_2 was shown in Table 4.2 and Figure 4.9. The approximately average grain size of Sb-doped SnO_2 at 6, 12 and 18 mol% were about 720 nm, 480 nm and 900 nm, respectively. The approximately average grain size of SnO_2 films were decreased with increased of Sb-doping concentrations (6 - 12 mol%). The similar results were obtained from Sb-doped SnO_2 films prepared by spray pyrolysis technique [27]. However, grain sizes were increased with Sb-doping reach to 18 mol%. The increased of grain size with Fe or Sb-doping (18 mol%) could be explained by possible reasons, with the increasing of doping concentrations, the deposited films lost the crystallinity, lead to high grain growth promotion.

Table 4.2 Approximately average grain size of SnO_2 thin films for different dopants and their doping levels*

Thin films	Approximately average grain size (nm)
SnO_2	880
Fe-doped SnO_2 6 mol%	1,436
Fe-doped SnO_2 12 mol%	1,780
Fe-doped SnO_2 18 mol%	2,700
Sb-doped SnO_2 6 mol%	720
Sb-doped SnO_2 12 mol%	480
Sb-doped SnO_2 18 mol%	900

* Approximately average grain size from at least 10 grains in each conditions.

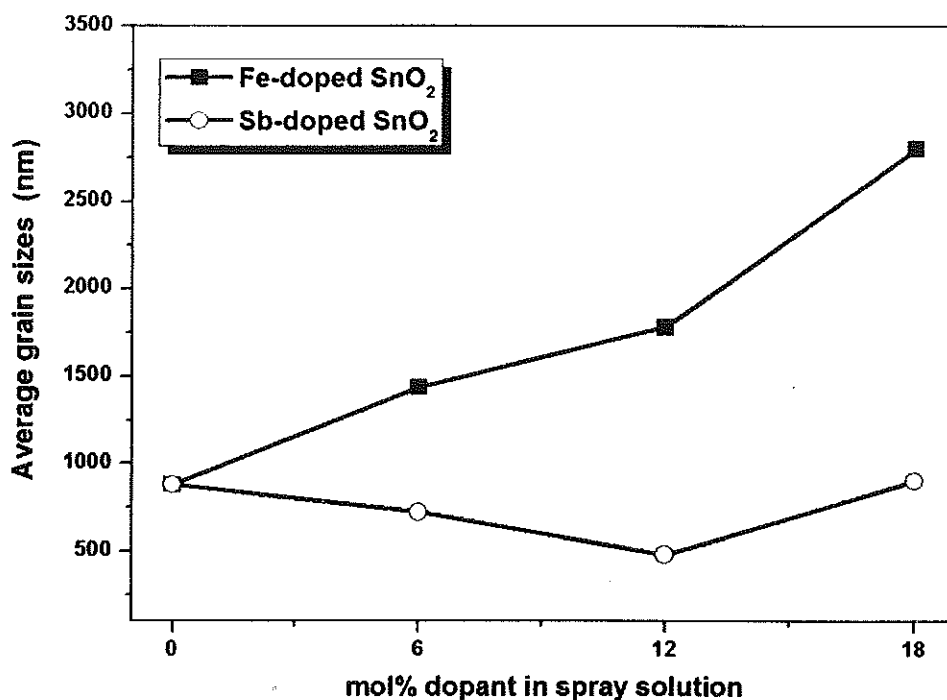


Figure 4.9 Approximately average grain sizes of films at various dopants as a function of mol% doping concentrations in spray solution.

4.2.2 Surface morphology studies of undoped and (Fe or Sb)-doped tin oxide films by AFM

2D and 3D atomic force micrographs of the undoped and (Fe or Sb)-doped tin oxide films for different dopant concentrations on a scanning area of $1 \times 1 \mu\text{m}$ were shown in Figure 4.10 - 4.11. Root mean square (RMS) roughnesses of the films from the AFM data were shown in Figure 4.12. For Fe-doped SnO_2 films, the surface roughness was found to increase with increasing Fe contents. Root mean square (RMS) roughness of films with 0, 6, 12 and 18 mol% Fe-doping were 18, 21, 23 and 26 nm, respectively. This was matched with other report related to the surface roughness studies by AFM [23]. On the other hand, root mean squared (RMS) roughness of films with 0, 6, 12 and 18 mol% Sb content were 18, 12, 11 and 13 nm, respectively. The surface roughness was found to be decreased with increasing the Sb content which correlated along with decreasing of crystalline sizes and grain sizes in the XRD and SEM analysis. The results confirmed that the crystalline sizes of the particles were decreased with increasing Sb-doping. The similar results were obtained from Sb-doped SnO_2 films prepared by sol gel

dip-coating technique [46]. However, for increasing of Sb-doping levels to 18 mol%, surface roughness of SnO_2 films were increased along with decreasing of crystalline sizes. That was due to increasing of doping concentrations, the deposited films lost the crystallinity, lead to high grain growth promotion, resulted to increasing of surface roughness of films.

Roughness of the surface was related to the crystalline sizes of films. The phenomenon was described by Ostwald ripening process [24, 47]. In the crystal growth process, the nucleation process was occurred and generated crystals. The crystals were combined to produce grains, grain sizes were depended on crystalline sizes. Large grains had lower surface to volume ratio, resulting to a lower energy state. Then, small grains tended to detach and diffuse though the surface of larger grains, lead to grain segregation and sizes of grains were very different. The different of large and small grain sizes on surface films were led to high surface roughness. In contrast, thin films with small crystalline sizes had small grain sizes with high surface energy and resulted to low surface roughness due to regularly of small grain sizes.

For Sb-doping, the surface roughness of SnO_2 films were decreased with increasing of Sb-doping levels, due to incorporation of Sb atoms in SnO_2 lattice which produced lattice defect and enhanced nucleation sites. Consequently, small crystalline sizes were formed on surface of films and resulted to decrease of surface roughness of films. However, the surface roughness was found to be increased with 18 mol% Sb-doping. For high doping levels, the deposited films lost the crystallinity, led to grain growth promotion producing more roughness of surface in films.

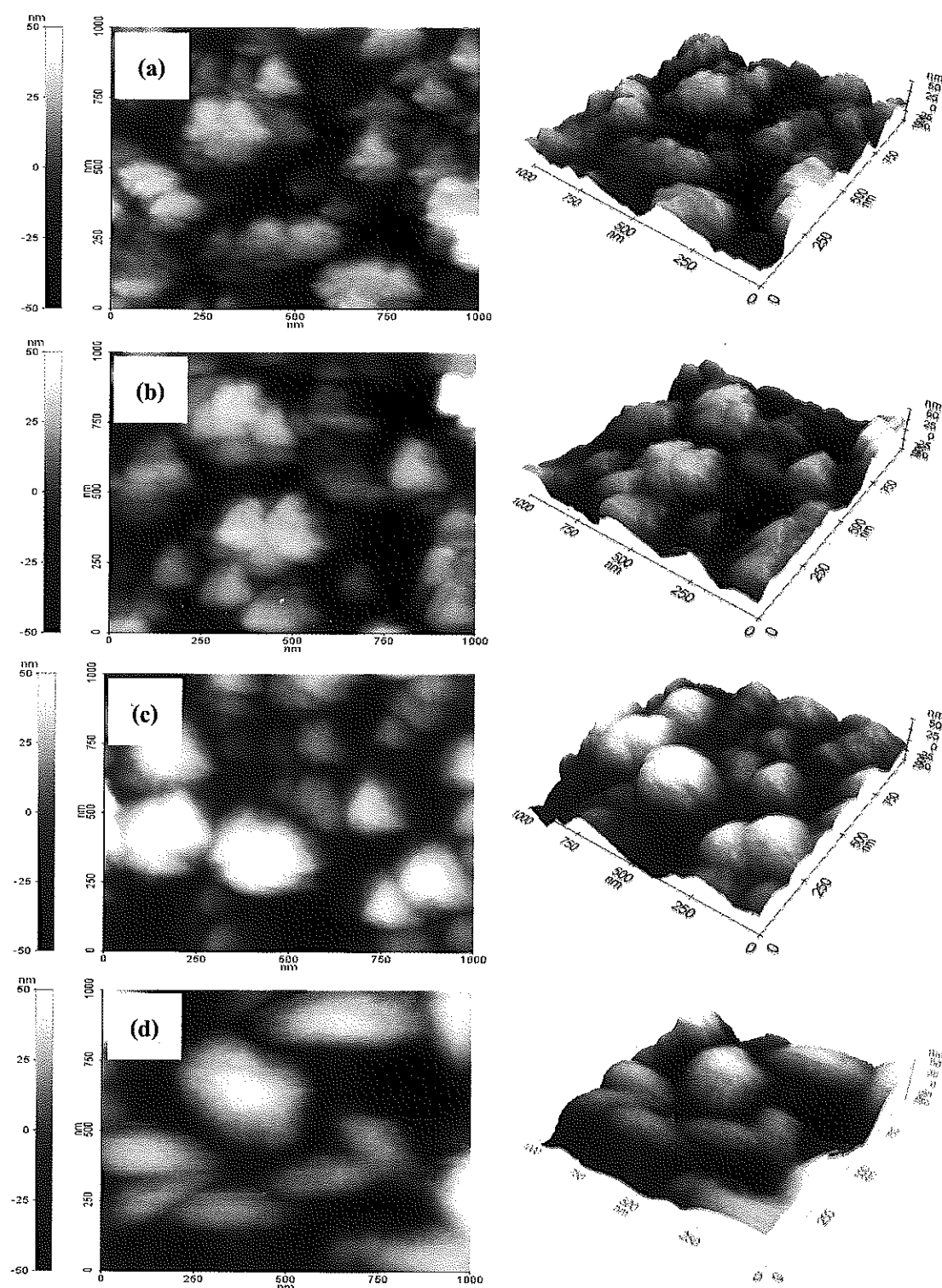


Figure 4.10 2D (left) and 3D (right) AFM micrograph of SnO_2 thin films for different dopants and various doping levels: (a) undoped SnO_2 , (b) Fe-doped SnO_2 6 mol%, (c) Fe-doped SnO_2 12 mol% and (d) Fe-doped SnO_2 18 mol%.

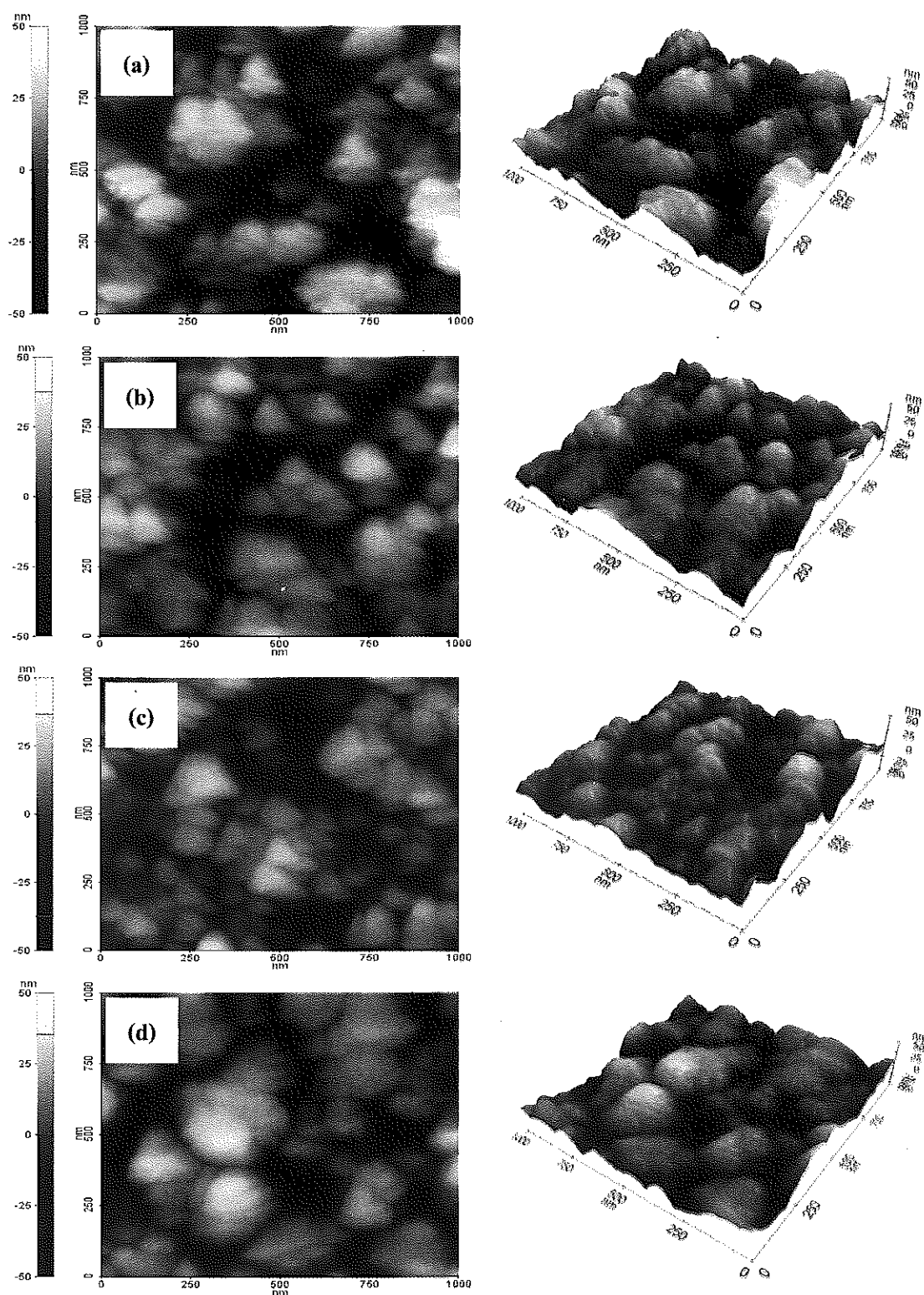


Figure 4.11 2D (left) and 3D (right) AFM micrograph of SnO_2 thin films for different dopants and various doping levels: (a) undoped SnO_2 , (b) Sb-doped SnO_2 6 mol%, (c) Sb-doped SnO_2 12 mol% and (d) Sb-doped SnO_2 18 mol%.

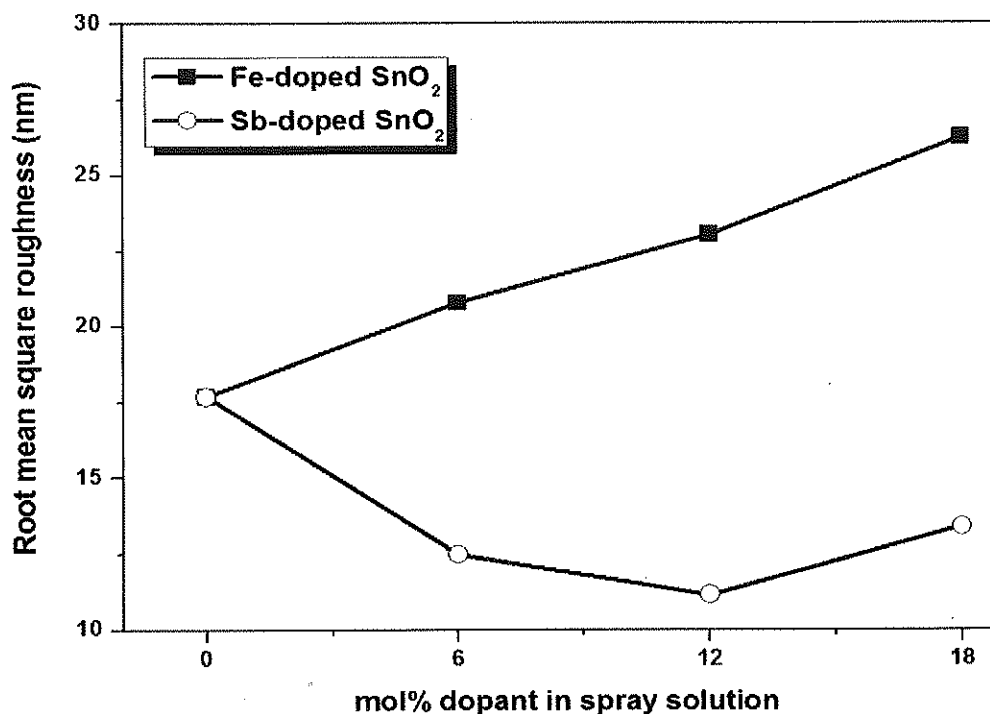


Figure 4.12 Root mean square (RMS) roughness of films at various dopant as a function of mol% doping concentrations in spray solution.

Mean grain size from AFM of thin films at various dopants as a function of mol% doping concentrations in spray solution were presented in Figure 4.13. For Fe-doped SnO_2 films, the mean grain size of films with 0, 6, 12 and 18 mol% Fe content were 269, 335, 373 and 527 nm, respectively. The mean grain size was increased with increasing the Fe content. Moreover, some trace amount of Fe may be segregated at the surface of the film due to solubility of Fe in SnO_2 was primarily responsible for surface segregation [24]. In the case of Fe-doped films, the surface agglomerates were elongated as compared to their shape deformations of crystalline in the Fe-doped SnO_2 thin films due to the stacking fault density [24].

For Sb-doping, the mean grain size of films with 6, 12 and 18 mol% Sb-doping content were 176, 107 and 225 nm, respectively. The mean grain of Sb-doping films was found to decrease with increasing the Sb content to 6 - 12 mol%, which good agreement with the XRD and SEM results. Therefore, the crystalline sizes of the films were decreased with increasing Sb-doping. The mean grain size for Fe-doped SnO_2 films were larger than that of Sb-doped SnO_2 films, shown in Figure 4.13. That was good agreement with the tetragonal distortion of films from

the XRD analysis, confirming that the solid solution limit of Fe ions in SnO_2 film could be higher than that of Sb ions. For Sb-doped SnO_2 , doping SnO_2 by Sb provided maximum decrease of the grain sizes at the same concentrations of Fe-doping. The grains of the second oxide located between the SnO_2 grains could be really prohibited from the tin atoms transferring from the one crystalline to another one during the film deposition. The presence of the second oxide promoted the generation of a larger number of nucleation centers for the SnO_2 growth. However, grain sizes of SnO_2 films were increased with 18 mol% Sb-doping, due to high substitution of Sn atoms by Sb atoms at high Sb-doping raised to amorphous films, which affected to increase of grain growth promotion on SnO_2 films surface.

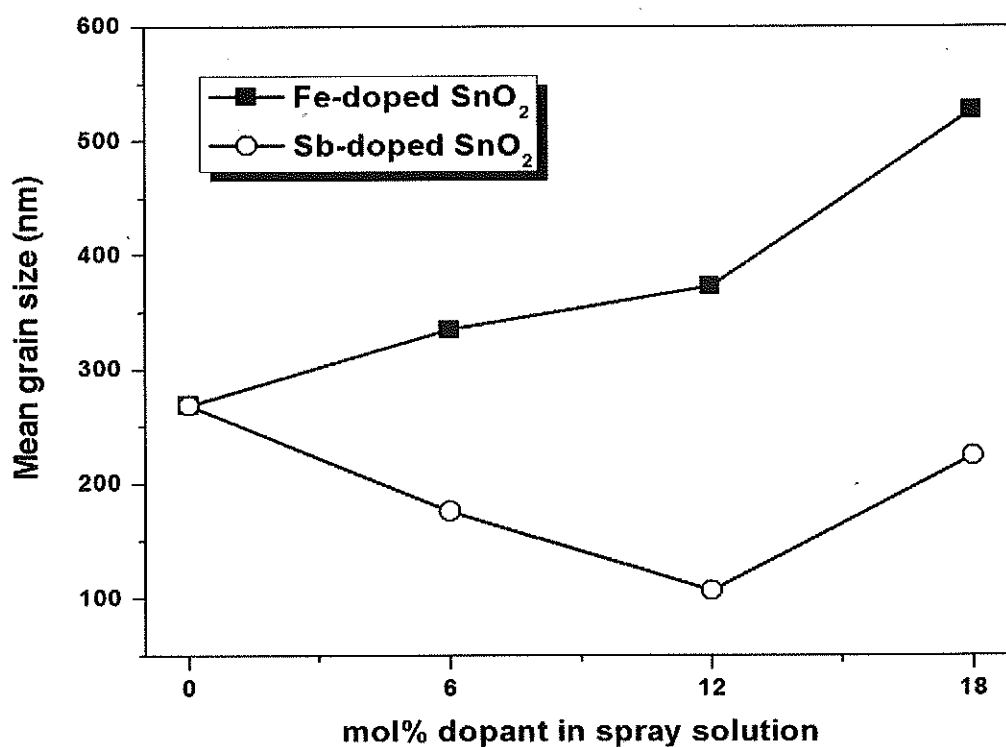


Figure 4.13 Mean grain sizes from AFM of thin films at various dopant as a function of mol% doping concentrations in spray solution.

4.3 Optical properties of undoped and (Fe or Sb)-doped tin oxide films

4.3.1 Characterization of undoped and (Fe or Sb)-doped tin oxide films by FT-IR

From Figure 4.14, the FT-IR transmittance spectra of the powder scratched from the SnO_2 , Fe- and Sb-doped SnO_2 thin films in the wavenumber range $400 - 1500 \text{ cm}^{-1}$ were illustrated. The FT-IR transmittance spectra presented the information about phase composition, and the way of oxygen was bound to the metal ions (M – O structure). The transmission peak of the prepared films at $700 - 1018 \text{ cm}^{-1}$ corresponded to vibration of Si-O bond. The Si-O vibration mode was appeared due to the powder scratched of glass substrate [48]. The vibration of Sn-O was appeared in the range of $400 - 700 \text{ cm}^{-1}$ as the result of condensation reaction. In previous result, Krishnakumar et al. [41] reported the FT-IR transmission spectra of SnO_2 nanostructure prepared by chemical precipitation technique. The FT-IR transmission band of films was appeared at 480 cm^{-1} which could be attributed to stretching frequency of Sn-O. In the other works, Song et al. prepared $\alpha\text{-Fe}_2\text{O}_3$ nanotube by hydrothermal method. The FT-IR transmission spectra of $\alpha\text{-Fe}_2\text{O}_3$ nanotube was presented at $455, 540$ and 1010 cm^{-1} which had been attributed to bending and stretching vibration frequency of Fe-O, respectively [49]. In addition, Abdullah et al. prepared Sb_2O_3 nanoparticles by forward and reverse precipitation technique. The FT-IR of Sb_2O_3 nanoparticles were presented at 460 and 596 cm^{-1} which attributed to stretching frequency of Sb-O [50].

In this work, the FT-IR transmission peaks of Fe-doped SnO_2 at 6, 12 and 18 mol% were $472, 483$ and 491 cm^{-1} , whereas those of tin oxide doped with Sb were $470, 475$ and 480 cm^{-1} , respectively (see in Table 4.3). The transmission band of Fe or Sb-doped SnO_2 thin films were slightly shift to the higher wavenumbers compared with pure SnO_2 (467 cm^{-1}). The results could be explained that, in Fe- and Sb-doped SnO_2 , Fe and Sb had been supposed to substituted Sn in of Sn-O group symmetric vibration. The different in charge and crystal radius of Sn, Fe and Sb was changed in symmetric vibration of Sn-O due to asymmetric vibration, and it increase the defect in SnO_2 lattice because of lattice mismatch. Asymmetric vibration was required more energy for molecular vibration than symmetric vibration. Therefore, the Sn-O band was resulted to shift into higher wavenumber with addition of dopants. The FT-IR results were good agreement with other authors [51-52]. In other possible reasons, a solubility limit of Fe and Sb atoms in SnO_2 lattice was generated the excess of Fe and Sb atoms, which could not replace the

with other authors[51-52]. In other possible reasons, a solubility limit of Fe and Sb atoms in SnO_2 lattice was generated the excess of Fe and Sb atoms, which could not replace the Sn atoms in the lattice, but form the interstitial additives. The presence of interstitial additives were increased the disorder of lattice markedly, which was caused to the shifting of Sn-O vibration frequency at high doping levels[52].

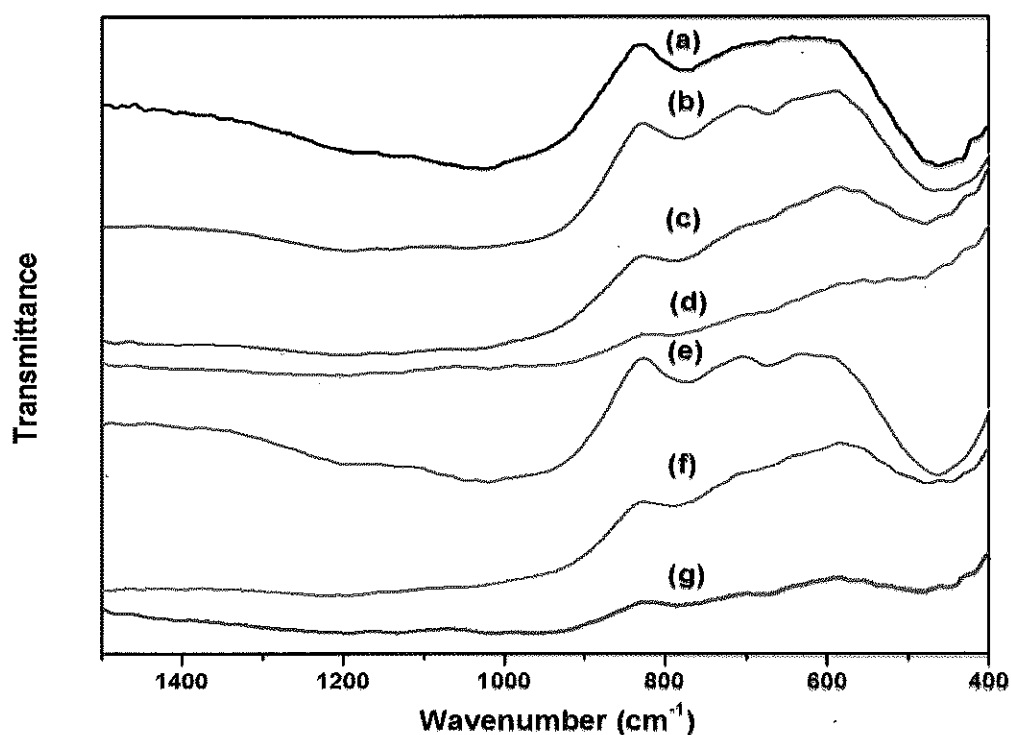


Figure 4.14 FT-IR spectra of the powder scratched from films:(a) undoped SnO_2 , (b) Fe-doped SnO_2 6 mol%, (c) Fe-doped SnO_2 12 mol%, (d) Fe-doped SnO_2 18 mol%, (e) Sb-doped SnO_2 6 mol%, (f) Sb-doped SnO_2 12mol% and (g) Sb-doped SnO_2 18 mol%.

Table 4.3 The main vibration frequencies (cm^{-1}) of SnO_2 thin films for different dopants and various doping levels

Thin film	Vibration frequencies (cm^{-1})
SnO_2	467
Fe-doped SnO_2 6 mol%	472
Fe-doped SnO_2 12 mol%	483
Fe-doped SnO_2 18 mol%	491
Sb-doped SnO_2 6 mol%	470
Sb-doped SnO_2 12 mol%	475
Sb-doped SnO_2 18 mol%	480

From Table 4.3, the vibration peaks of SnO_2 film with Fe-doping were shifted to higher wavenumber than those of Sb-doping at the same doping level. The incorporation of Fe ions were change in the symmetry vibration of Sn-O group in SnO_2 lattice than that of Sb ions, supporting by tetragonal lattice distortion of Fe-doped SnO_2 films which higher than that of Sb-doping at the same doping level (seen Table 4.1). Fe-doping were influenced on distortion of SnO_2 lattice structure more than that of Sb-doping, which was agreement to the shifting of vibration peak in FT-IR analysis.

4.3.2 Effect of dopants (Fe or Sb) and doping levels on the photoluminescence properties of tin oxide films

The room temperature photoluminescence (PL) emission spectra from 320 - 400 nm of the Fe- and Sb-doped SnO_2 thin films in various doping level at 0, 6, 12 and 18 mol% were shown in Figure 4.15 and Table 4.4. All SnO_2 films with various concentrations of Fe or Sb dopants exhibited were one emission peak with a wavelength of about 367 nm. The phonon energy corresponded to wavelength of 367 nm was about 3.38 eV. If the band gap of films was the bulk SnO_2 , this emission peak should be originated from the electrons transition from conduction band to acceptor level formed by interstitial oxygen atoms.

However, the band gap of undoped SnO_2 film in our work was about 3.53 eV not 3.38 eV (see below for section 4.3.4). Therefore, the emission peak of about 367 nm should not be originated from the electron transition from conduction band to acceptor band formed by

interstitial oxygen atoms. The emission band was related to the interface traps existing in the depletion regions among the SnO_2 grains boundaries and the level of the interface traps about 0.15 eV below the conduction band edge, which could be known that $3.38 + 0.15$ equaled to 3.53 eV. The single emission band appearance was due to radiative defects, related to the interface traps existing at the grain boundary and then emitted from the radiative transition from the level of 0.15 eV below the conduction band to the valance band [53].

Moreover, the previous works reported that the peak intensity of SnO_2 PL emission decreased with Fe [24] or Sb [54] doping. In present work, the PL intensity of SnO_2 doped with Fe at 6, 12 and 18 mol% were 80, 49 and 9 arb. unit, whereas Sb-doping levels were 43, 26 and 7 arb. unit, respectively. The results concluded that the PL emission intensity of films was decreased with increasing Fe- or Sb-doping level compared with pure SnO_2 (99 arb. unit).

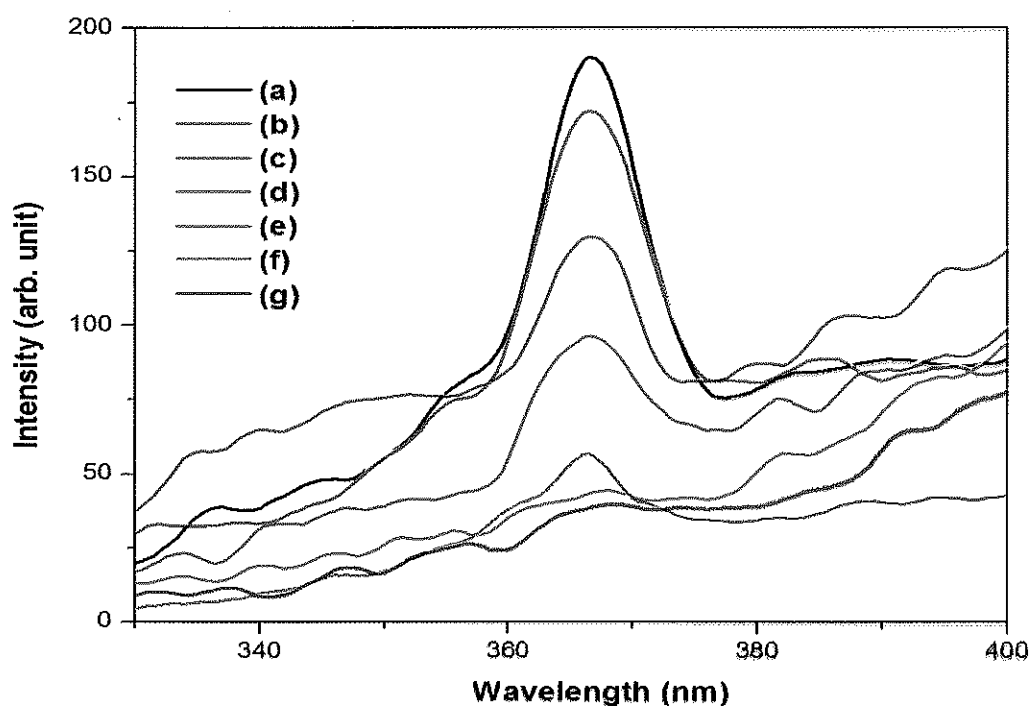


Figure 4.15 Photoluminescence spectra of (a) undoped SnO_2 , (b) Fe-doped SnO_2 6 mol%, (c) Fe-doped SnO_2 12 mol%, (d) Fe-doped SnO_2 18 mol%, (e) Sb-doped SnO_2 6 mol%, (f) Sb-doped SnO_2 12 mol% and (g) Sb-doped SnO_2 18 mol%.

Table 4.4 Photoluminescence (PL) emission intensity of SnO₂ thin films for different dopants and various doping levels

Thin film	PL emission intensity (arb. unit)
SnO ₂	99
Fe-doped SnO ₂ 6 mol%	80
Fe-doped SnO ₂ 12 mol%	49
Fe-doped SnO ₂ 18 mol%	9
Sb-doped SnO ₂ 6 mol%	43
Sb-doped SnO ₂ 12 mol%	26
Sb-doped SnO ₂ 18 mol%	7

From Table 4.4, possible origin of these peaks following, at room temperature, the high density of oxygen vacancies interacting with interfacial tin, led to the formation of a considerable amount of trapped states within the band gap, giving rise to high PL intensity of pure SnO₂. In spray deposited polycrystalline oxides, oxygen vacancies were known to be the most common defects and form the donor level. Moreover, because of the pyrolytic decomposition, there should be the existence of oxygen vacancies due to rapid evaporation and oxidation processes [54]. On the other hands, doping SnO₂ nanostructure by additives such as transition metal gave a higher density of crystalline defects such as stacking faults and point defects than their bulk host. These intrinsic defects were often caused to PL emission reduction at room temperature.

In the present case, the relative intensity of this peak was decreased in Fe- or Sb-doped films (seen in Figure 4.16), due to the acceptor nature of Fe and Sb ions with respect to Sn⁴⁺ ions in the SnO₂ matrix. Doped SnO₂ with Fe and Sb ions led to reduction of donor type oxygen vacancies, thereby reducing the radiative recombination centers. Hence, the intensity of oxygen vacancy related emission was decreased in Fe- or Sb-doped SnO₂ thin films [24]. In addition, the nature of this PL peak was indicated that it might decreased due to surface states of SnO₂ thin films. However, intensity reduction of this peak could also cause by possible partial segregation of Fe or Sb, modifying the surface states and the PL behavior in Fe or Sb-doped SnO₂ thin films.

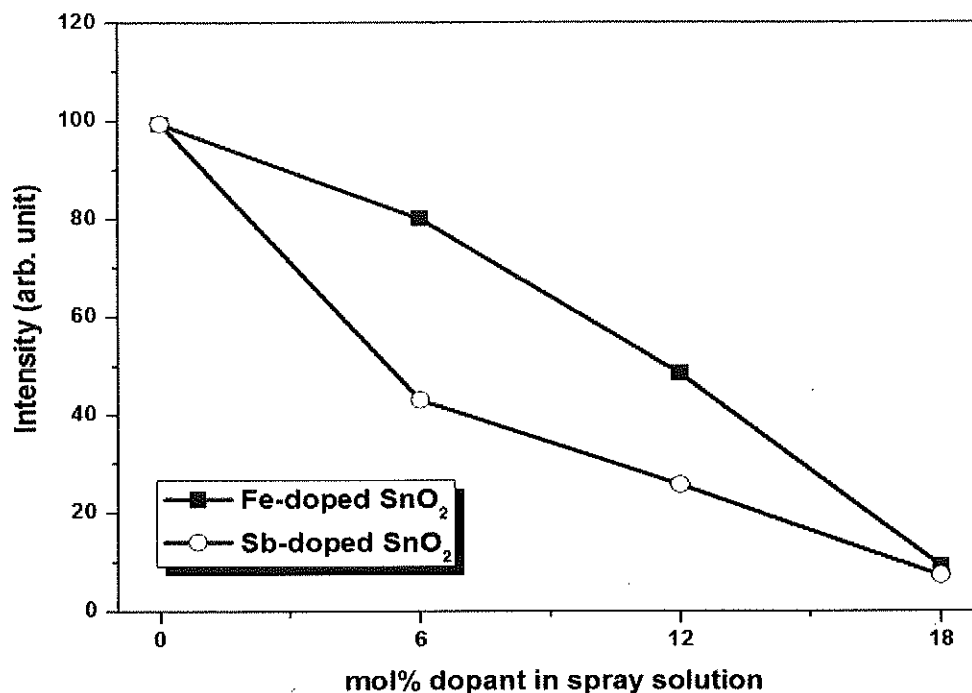


Figure 4.16 Variation of PL emission intensity of SnO₂ films at various dopant as a function of mol% doping concentrations in spray solution.

Furthermore, Fe or Sb-doping was led to change in the surface morphology of films. The microstructure changed along with defect chemistry of Fe- or Sb-doping in SnO₂ films led to variation of the room temperature PL spectra compared to pure SnO₂ films. The reduction of PL emission intensity were attributed to structural defects and surface states correlating to enhance of strain and rendered to variation of films surface morphology with Fe- and Sb doping, which was agreement in XRD, SEM and AFM results.

4.3.3 Effect of dopants (Fe or Sb) and doping levels on the transparency of tin oxide films

The optical transmittances spectra in the range of 300 - 1100 nm in SnO₂ and Fe- or Sb-doped SnO₂ thin films at 6, 12 and 18 mol% doping concentrations were shown in Figure 4.17. The average transmittance values in visible region (400 - 800) of films were presented in Figure 4.18.

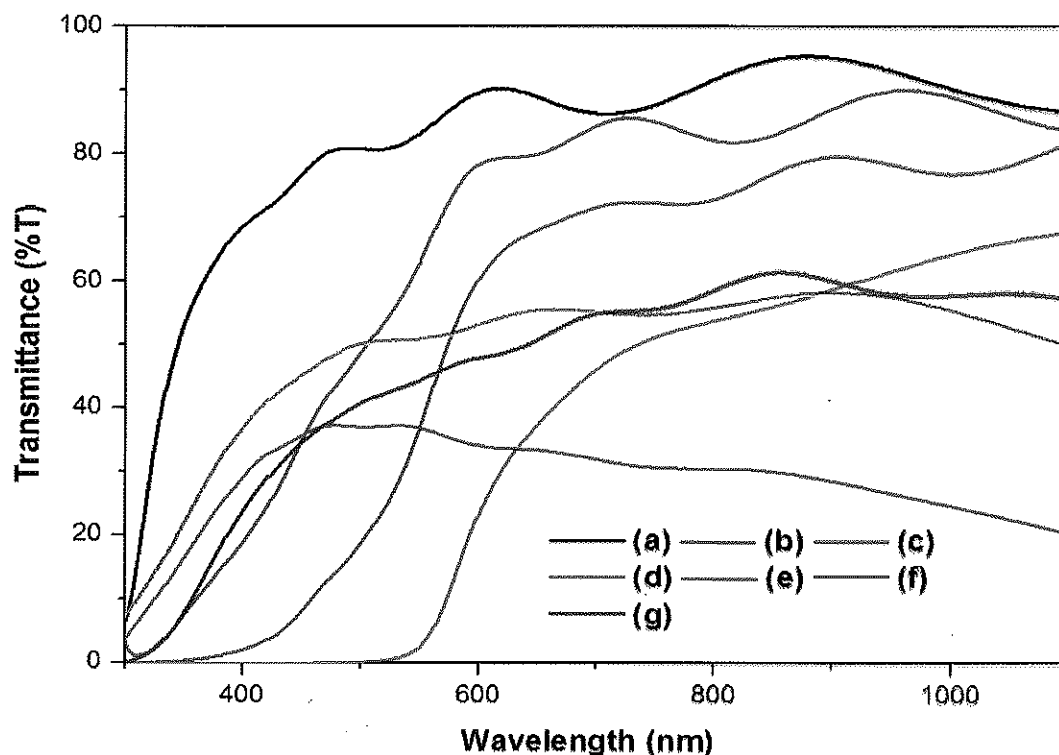


Figure 4.17 Optical transparency of thin films at various dopant as a function of mol% doping concentrations in spray solution: (a) undoped SnO_2 , (b) Fe-doped SnO_2 6 mol%, (c) Fe-doped SnO_2 12 mol%, (d) Fe-doped SnO_2 18 mol%, (e) Sb-doped SnO_2 6 mol%, (f) Sb-doped SnO_2 12 mol% and (g) Sb-doped SnO_2 18 mol%.

The average transmittance values in visible region (400 - 800) of doped thin films were lower than those of the pure SnO_2 as shown in Figure 4.18. The results could be explained that, materials containing an element in two different oxidation states of host and dopants were gave manifest deep and high intense light absorption. The electron transfer between the different oxidation states of the elements was caused to high intense light absorption [27]. The other reason for optical transmission reduction might cause from scattering effect on thin films surface [21]. The decrease in transmittance with the increase in dopant concentrations was attributed to substitution of Sn atoms by Fe or Sb atoms. The diffused and multiple reflections at the surface were occurred and given the reduction of films transparency.

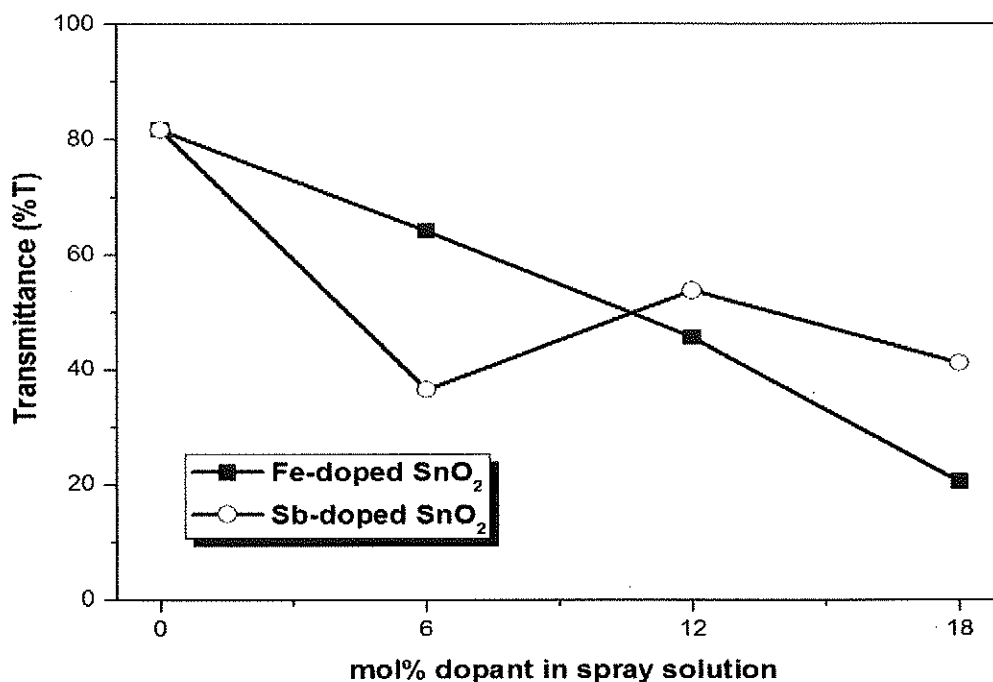


Figure 4.18 Average transmittance values in visible region (400 - 800 nm) from transmission spectra of thin films at various dopant as a function of mol% doping concentrations in spray solution.

The average optical transmittance of Sb-doped SnO₂ films were demonstrated in Figure 4.18 and Table 4.5. The mean transmittance of pure SnO₂ films was found to decrease on the addition of 6 mol% of Fe and Sb in spray solution. At 6 mol% doping, the average transmittances of Sb-doped SnO₂ films were lower than those of Fe-doping at the same doping levels. The results could be explained following, highly Sb-doped SnO₂ films which were elaborated by spray pyrolysis was presented a bluish coloration due to a charge transfer between two oxidation states of antimony, Sb³⁺ and Sb⁵⁺ [27]. As the amount of doping of Sb in SnO₂ was increased, the films color became darker. Changing in the Sb-doped SnO₂ film colors was attributed to the provision of additional electrons below the conduction band (transition state) in SnO₂ matrix by the Sb ions of doped state in SnO₂ lattice. Those colors were due to the property of ready excitation of the addition electrons. Moreover, the two oxidation states of antimony, Sb³⁺ and Sb⁵⁺ were generated more defects in SnO₂ films, resulting to high adsorption. More transmission reduction of Sb-doping was generated, when compared with Fe-doping.

Table 4.5 Transparency (%T) of SnO₂ thin films for different dopants and their doping levels

Thin film	Transparency (%T)
SnO ₂	81.68
Fe-doped SnO ₂ 6 mol%	64.08
Fe-doped SnO ₂ 12 mol%	45.55
Fe-doped SnO ₂ 18 mol%	20.53
Sb-doped SnO ₂ 6 mol%	36.49
Sb-doped SnO ₂ 12 mol%	53.69
Sb-doped SnO ₂ 18 mol%	41.14

However, the average transmittance at 12 and 18 mol% Sb-doping were higher than that of 6 mol% Sb-doping. These results were similarly in other reports [55]. High amount of Sb-doping in SnO₂ films was presented in the amorphous structure (shown in Table 4.1). At high Sb-doping, the deficiency in oxygen content was associated with the formation of SnO compound in the SnO₂ films. The differences in coordination of Sb³⁺ and Sb⁵⁺ ions led to the asymmetric atmosphere around them and made it difficult for electron transfer to take place due to increasing of amorphous structure of thin films. Thus, the increase of the amorphization in Sb-doped SnO₂ films with Sb-doping were caused in the increase of their transparency [55].

4.3.4 Effect of dopants (Fe or Sb) and doping levels on the optical band gap energy of tin oxide films

Fe- or Sb-doping also had influence on optical band gap (E_g) of the SnO₂ films [21, 27]. The direct optical band gap of SnO₂, Fe- and Sb-doped SnO₂ thin films at 6, 12 and 18 mol% doping concentrations were shown in Figure 4.19 and Table 4.6. As seen in Table 4.6, optical band gap of tin oxide doped with Fe-doping levels at 6, 12 and 18 mol% were 2.66, 2.20 and 2.07 eV, while for Sb-doping levels were 3.41, 3.09 and 3.24 eV, respectively. The optical band gaps were decreased with increasing of doping concentrations compared with pure SnO₂ (3.53 eV).

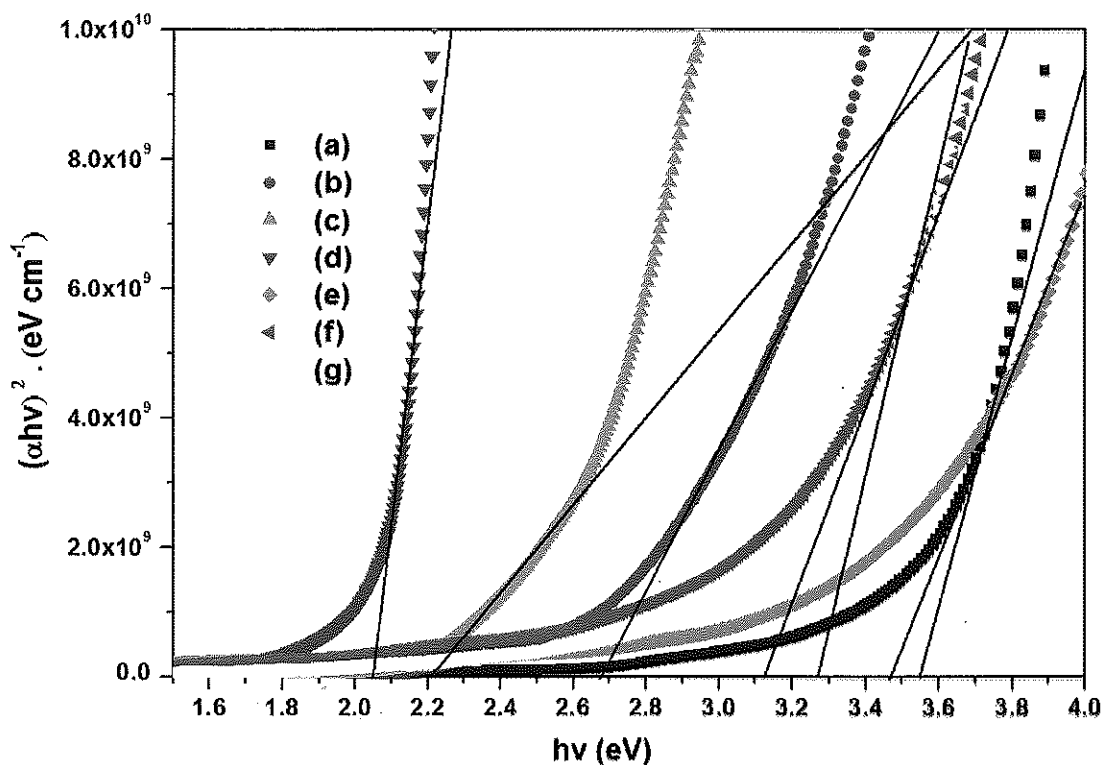
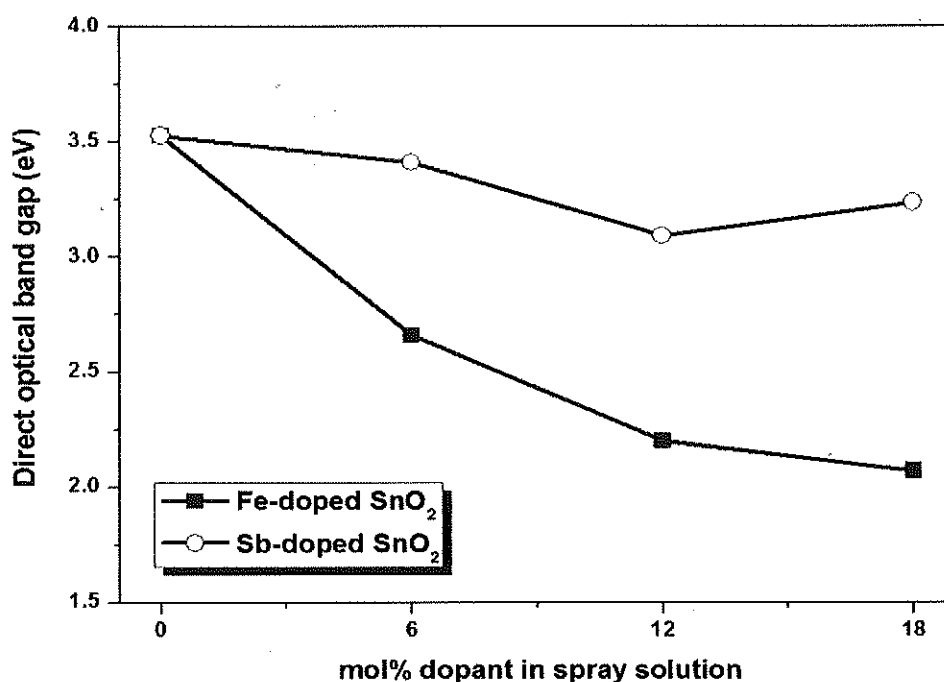


Figure 4.19 Direct optical band gap of thin films at various dopant as a function of mol% doping concentrations in spray solution: (a) undoped SnO_2 , (b) Fe-doped SnO_2 6 mol%, (c) Fe-doped SnO_2 12 mol%, (d) Fe-doped SnO_2 18 mol%, (e) Sb-doped SnO_2 6 mol%, (f) Sb-doped SnO_2 12 mol% and (g) Sb-doped SnO_2 18 mol%.

Furthermore, the red shift of the band edge of transition-metal-doped II-VI semiconductors was attributed to the sp-d spin - exchange interaction between the band electrons and the localized d - electrons of the transition metal ion substituting the cation. The s - d and p - d exchange interactions could give rise to a negative and a positive correction to the conduction and the valence band edges, respectively, which would lead to a SnO_2 band gap narrowing [53]. The other reasons for optical band gap reduction might be seen in lattice strain values in XRD analysis results (see in Table 4.1). The strain values were increased with increased dopant concentrations, which related to incorporation of dopant atoms to the lattice of SnO_2 and enhanced of lattice defect. That resulted in decreased optical band gap in SnO_2 thin films with increasing of doping concentrations.

Table 4.6 The direct optical band gaps of SnO₂ thin films for different and their doping levels

Thin film	Direct optical band gap (eV)
SnO ₂	3.53
Fe-doped SnO ₂ 6 mol%	2.66
Fe-doped SnO ₂ 12 mol%	2.20
Fe-doped SnO ₂ 18 mol%	2.07
Sb-doped SnO ₂ 6 mol%	3.41
Sb-doped SnO ₂ 12 mol%	3.09
Sb-doped SnO ₂ 18 mol%	3.24

**Figure 4.20** Direct optical band gaps of thin films at various dopant as a function of mol% doping concentrations in spray solution.

The variation of direct band gap of SnO₂ films with function of Fe- and Sb-doping levels were presented in Figure 4.20. As seen, the optical band gaps of Fe-doped SnO₂ films were lower than Sb-doping at same doping level. This observation could be described with band gap of dopant sources. In fact, the optical band gap of host was depended on band gap of

dopant sources. The direct optical band gap of Fe_2O_3 and Sb_2O_3 were 2.6 eV [56] and 3.4 - 3.6 eV [57], respectively. It was found that, the optical band gap of Fe dopant source was lower than Sb dopant source. That was lead to low optical band gap of Fe-doped SnO_2 compared with Sb-doping. In the other reasons, the tetragonal lattice distortion of Fe-doping was higher than Sb-doping, which relate to high solid solution limit. That was lead to high substitution of Fe ions in SnO_2 structure. Moreover, optical band gap energy of Sb-doping was increased at 18 mol% doping. That was due to the low limit of solid solution of Sb ions in SnO_2 films, related to limit of Sb substitution in SnO_2 lattice structure.

CHAPTER 5

CONCLUSIONS

The aim of this thesis work has been focused on the structural and optical properties of Fe or Sb-doped SnO_2 thin films deposited on micro-slide glass by spray pyrolysis. Doping levels influences (0, 6, 12 and 18 mol%) on films properties were investigated by XRD, SEM, AFM, FT-IR, Photoluminescence and UV-Vis spectroscopic analysis techniques.

Based on the experiment results, the conclusions were presented as follows:

1. From the XRD results, polycrystalline structure with clearly characteristic peak of the rutile phases SnO_2 crystallites with tetragonal structure in undoped SnO_2 , Fe-doped SnO_2 6 and 12 mol% and Sb-doped SnO_2 6, 12 and 18 mol%, except only 18 mol% Fe-doped SnO_2 .

2. From SEM analysis, the grain growth of SnO_2 films was increased with increasing of Fe-doping and suppressed with increasing of Sb-doping.

3. AFM analysis showed that the increase of Sb-doping level reduced the grain growth of SnO_2 films with reduction of both the grain size and the surface roughness, in contrasted with Fe-doping. The doping SnO_2 with Sb were effected on grain growth suppression of films more than that of Fe-doping.

4. From FT-IR results, Sn ions could be replaced by Fe or Sb ions on SnO_2 lattice. The substitutions of dopants ions was changed the symmetry of Sn-O group and increased the defects in SnO_2 lattice because of lattice mismatch, and caused in shifting to higher wavenumber of Fe-doping than that of Sb-doping at the same doping level.

5. The photoluminescence (PL) analysis indicated that the PL emission intensity of SnO_2 film was suppressed by Fe or Sb-doping. The PL intensity of SnO_2 film with Sb-doping was lower than Fe-doping at the same doping level, because the incorporation of Sb ions were more produced a higher density of crystalline defects of SnO_2 films compared with Fe ions.

6. The SnO_2 film doped with Fe or Sb were presented a decrease of direct optical band gap. At the same doping level, the direct optical band gaps of Fe-doping was less than those of Sb-doping. The Fe-dopings were effected on optical band gap of SnO_2 more than that of

Sb-doping. Transparency of SnO_2 films were decreased with increasing of Fe- or Sb-doping level due to a charge transfer transition between two oxidation states of dopants and host.

REFERENCES

REFERENCES

- [1] Hosono, H. "Recent progress in transparent oxide semiconductors: Materials and device application", Thin Solid Films. 515(15): 6000-6014, 2007.
- [2] Jie, J. et al. "One-dimensional II–VI nanostructures: Synthesis, properties and optoelectronic applications", Nano Today. 5(4): 313-336, 2010.
- [3] Murakami, K. et al. "Initial growth of SnO₂ thin film on the glass substrate deposited by the spray pyrolysis technique", Thin Solid Films. 515(24): 8632-8636, 2007.
- [4] Ma, H.L. et al. "Thickness dependence of properties of SnO₂: Sb films deposited on flexible substrates", Applied Surface Science. 191(1-4): 313-318, 2002.
- [5] Patil, L.A. et al. "Highly sensitive and quickly responding ultrasonically sprayed nanostructured SnO₂ thin films for hydrogen gas sensing", Sensors and Actuators B: Chemical. 143(1): 270-277, 2009.
- [6] Patil, L.A. et al. "Highly sensitive ethanol sensors based on nanocrystalline SnO₂ thin films", Current Applied Physics. 10(5): 1249-1254, 2010.
- [7] El-Etre, A.Y. and Reda, S.M. "Characterization of nanocrystalline SnO₂ thin film fabricated by electrodeposition method for dye-sensitized solar cell application", Applied Surface Science. 256(22): 6601-6606, 2010.
- [8] Arias, A.C. et al. "The use of tin oxide thin films as a transparent electrode in PPV based light-emitting diodes", Thin Solid Films. 371(1-2): 201-206, 2000.
- [9] Gordillo, G. et al. "Characterization of SnO₂ thin films through thermoelectric power measurements", Thin Solid Films. 342(1-2): 160-166, 1999.
- [10] Gubbins, M.A. et al. "Nanostructural characterisation of SnO₂ thin films prepared by reactive r.f. magnetron sputtering of tin", Thin Solid Films. 405(1-2): 270-275, 2002.
- [11] Liu, P.Y. et al. "Characterizations of SnO₂ and SnO₂: Sb thin films prepared by PECVD", Vacuum. 76(1): 7-11, 2004.
- [12] Gu, F. et al. "Luminescence of SnO₂ thin films prepared by spin-coating method", Journal of Crystal Growth. 262(1-4): 182-185, 2004.

REFERENCES (CONTINUED)

- [13] Michel, E. et al. "SnO₂ thin films prepared by dip-coating from microwave synthesized colloidal suspensions", Journal of Colloid and Interface Science. 257(2): 258-262, 2003.
- [14] Zaouk, D. et al. "Fabrication of tin oxide (SnO₂) thin film by electrostatic spray pyrolysis", Microelectronic Engineering. 51-52(0): 627-631, 2000.
- [15] Zadsar, M. et al. "Substrate temperature effect on structural, optical and electrical properties of vacuum evaporated SnO₂ thin films", Materials Science in Semiconductor Processing. 15(4): 432-437, 2012.
- [16] Patil, P.S. et al. "Effect of substrate temperature on structural, electrical and optical properties of sprayed tin oxide (SnO₂) thin films", Ceramics International. 29(7): 725-734, 2003.
- [17] Serin, T. et al. "Electrical, structural and optical properties of SnO₂ thin films prepared by spray pyrolysis", Journal of Non-Crystalline Solids. 352(3): 209-215, 2006.
- [18] Kasar, R.R. et al. "Studies and correlation among the structural, optical and electrical parameters of spray-deposited tin oxide (SnO₂) thin films with different substrate temperatures", Physica B: Condensed Matter. 403(19-20): 3724-3729, 2008.
- [19] Patil, P.S. "Versatility of chemical spray pyrolysis technique", Materials Chemistry and Physics. 59(3): 185-198, 1999.
- [20] Jadsadapattarakul, D. et al. "Tin oxide thin films deposited by ultrasonic spray pyrolysis", Ceramics International. 34(4): 1051-1054, 2008.
- [21] Bagheri-Mohagheghi, M.M. et al. "Fe-doped SnO₂ transparent semi-conducting thin films deposited by spray pyrolysis technique: Thermoelectric and p-type conductivity properties", Solid State Sciences. 11(1): 233-239, 2009.
- [22] Korotcenkov, G. et al. "Cathodoluminescence studies of un-doped and (Cu, Fe, and Co)-doped tin dioxide films deposited by spray pyrolysis", Current Applied Physics. 10(4): 1123-1131, 2010.
- [23] Rani, S. et al. "Effect of Fe doping on the gas sensing properties of nano-crystalline SnO₂ thin films", Sensors and Actuators B: Chemical. 122(1): 204-210, 2007.

REFERENCES (CONTINUED)

- [24] Rani, S. et al. "Structure, microstructure and photoluminescence properties of Fe-doped SnO₂ thin films", Solid State Communications. 141(4): 214-218, 2007.
- [25] Soitah, T.N. et al. "Structural, optical and electrical properties of Fe-doped SnO₂ fabricated by sol-gel dip coating technique", Materials Science in Semiconductor Processing. 13(3): 125-131, 2010.
- [26] Bisht, H. et al. "Comparison of spray pyrolyzed FTO, ATO and ITO coatings for flat and bent glass substrates", Thin Solid Films. 351(1-2): 109-114, 1999.
- [27] Elangovan, E. and Ramamurthi, K. "A study on low cost-high conducting fluorine and antimony-doped tin oxide thin films", Applied Surface Science. 249(1-4): 183-196, 2005.
- [28] Elangovan, E. et al. "Studies on the structural and electrical properties of spray deposited SnO₂: Sb thin films as a function of substrate temperature", Solid State Communications. 130(8): 523-527, 2004.
- [29] Lee, S.Y. and Park, B.O. "Structural, electrical and optical characteristics of SnO₂: Sb thin films by ultrasonic spray pyrolysis", Thin Solid Films. 510(1-2): 154-158, 2006.
- [30] Rajpure, K.Y. et al. "Effect of Sb doping on properties of conductive spray deposited SnO₂ thin films", Materials Chemistry and Physics. 64(3): 184-188, 2000.
- [31] Ravichandran, K. and Philominathan, P. "Fabrication of antimony doped tin oxide (ATO) films by an inexpensive, simplified spray technique using perfume atomizer", Materials Letters. 62(17-18): 2980-2983, 2008.
- [32] Zhang, D. et al. "Surface morphologies and properties of pure and antimony-doped tin oxide films derived by sol-gel dip-coating processing", Materials Chemistry and Physics. 100(2-3): 275-280, 2006.
- [33] Hadia, N.M.A. et al. "Effect of the temperatures on structural and optical properties of tin oxide (SnO_x) powder", Physica B: Condensed Matter. 405(1): 313-317, 2010.
- [34] Batzill, M. and Diebold, U. "The surface and materials science of tin oxide", Progress in Surface Science. 79(2-4): 47-154, 2005.

REFERENCES (CONTINUED)

- [35] Rantala, T.T. et al. "Surface relaxation of the (110) face of rutile SnO_2 ", Surface Science. 420(1): 103-109, 1999.
- [36] Elangovan, E. et al. "Some physical properties of spray deposited SnO_2 thin films", Journal of optoelectronics and advanced materials. 6(1): 197 - 203, 2004.
- [37] Thanachayanont, C. et al. "Microstructural investigation and SnO nanodefects in spray-pyrolyzed SnO_2 thin films", Materials Letters. 65(17-18): 2610-2613, 2011.
- [38] Shanthi, S. et al. "Growth and characterization of antimony doped tin oxide thin films", Journal of Crystal Growth. 197(4): 858-864, 1999.
- [39] Amma, D.S.D. et al. "Structural, electrical and optical studies on chemically deposited tin oxide films from inorganic precursors", Materials Chemistry and Physics. 93(1): 194-201, 2005.
- [40] Smith, A. et al. "Relation between solution chemistry and morphology of SnO_2 -based thin films deposited by a pyrosol process", Thin Solid Films. 266(1): 20-30, 1995.
- [41] Krishnakumar, T. et al. "Structural, optical and electrical characterization of antimony-substituted tin oxide nanoparticles", Journal of Physics and Chemistry of Solids. 70(6): 993-999, 2009.
- [42] Parra, R. et al. "The influence of aluminium on the overall properties of SnO_2 -based varistors", Journal of Materials Science. 42(13): 4832-4837, 2007.
- [43] Fabricio, R. S., Elson, L. and Armando, B. "Electronic and structural properties of $\text{Sn}_x\text{Ti}_{1-x}\text{O}_2$ solid solutions: a periodic DFT study", Catalysis Today. 85(1): 145-152, 2003.
- [44] Beaulieu, L.Y and Dahn, J.R. "Measuring thickness changes in thin films due to chemical reaction by monitoring the surface roughness with in situ atomic force microscopy", Microscopy and Microanalysis. 8(2): 422-428, 2002.
- [45] Shannon, R.D. "Revised Effective Ionic Radii and Systematic Studies of Interatomic Distances in Halides and Chalcogenides", Acta Crystallographica Section A. 32(1): 751-767, 1976.

REFERENCES (CONTINUED)

- [46] Benrabah, B. et al. "Impedance studies of Sb doped SnO_2 thin film prepared by sol gel process", Superlattices and Microstructures. 50(6): 591-600, 2011.
- [47] "Ostwald ripening" http://en.wikipedia.org/wiki/Ostwald_ripening. 25 February, 2013.
- [48] Ahmed, S.F. et al. "Effect of Al doping on the conductivity type inversion and electro-optical properties of SnO_2 thin films synthesized by sol-gel technique", Journal of Sol-Gel Science and Technology. 39(3): 241-247, 2006.
- [49] Song, L. et al. "A hydrothermal method for preparation of $\alpha\text{-Fe}_2\text{O}_3$ nanotubes and their catalytic performance for thermal decomposition of ammonium perchlorate", Colloids and Surfaces A: Physicochemical and Engineering Aspects. 360(1-3): 1-5, 2010.
- [50] Abdullah, A.H. et al. "Effect of precipitation route on the properties of antimony trioxide", Materials Chemistry and Physics. 111(2-3): 201-204, 2008.
- [51] Wang, X.C. et al. "Microstructure, magnetic and optical properties of sputtered polycrystalline ZnO films with Fe addition", Applied Surface Science. 256(6): 1930-1935, 2010.
- [52] Zhang, B., Zhang, J. and Cai, W. "The FTIR studies on the structural and electrical properties of SnO_2 : F films as a function of hydrofluoric acid concentration", Optoelectronic and Advanced Materials 4(8): 1158-1162, 2010.
- [53] Wang, C. et al. "Structure, morphology and properties of Fe-doped ZnO films prepared by facing-target magnetron sputtering system", Applied Surface Science. 255(15): 6881-6887, 2009.
- [54] Babar, A.R. et al. "Physical properties of sprayed antimony doped tin oxide thin films: The role of thickness", Journal of Semiconductors. 32(5): 1-8, 2011.
- [55] Shokr, E.K. et al. "Sb-doping effects on optical and electrical parameters of SnO_2 films", Journal of Physics and Chemistry of Solids. 61(1): 75-85, 2000.
- [56] Zhou, H.S. et al. "Nonlinear Optical Susceptibility of Fe_2O_3 Thin Film Synthesized by a Modified Sol-Gel Method", Journal of Sol-Gel Science and Technology. 19(1-3): 539-541, 2000.

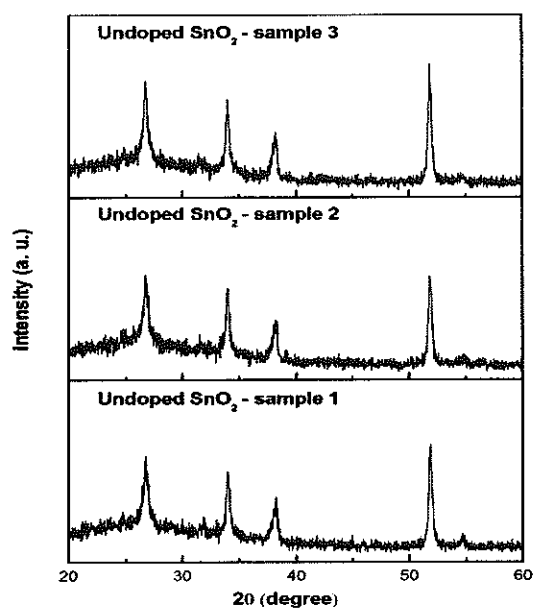
REFERENCES (CONTINUED)

- [57] Tigau, N. et al. "The effect of substrate temperature on the optical properties of polycrystalline Sb_2O_3 thin films", Journal of Crystal Growth. 277(1-4): 529-535, 2005.

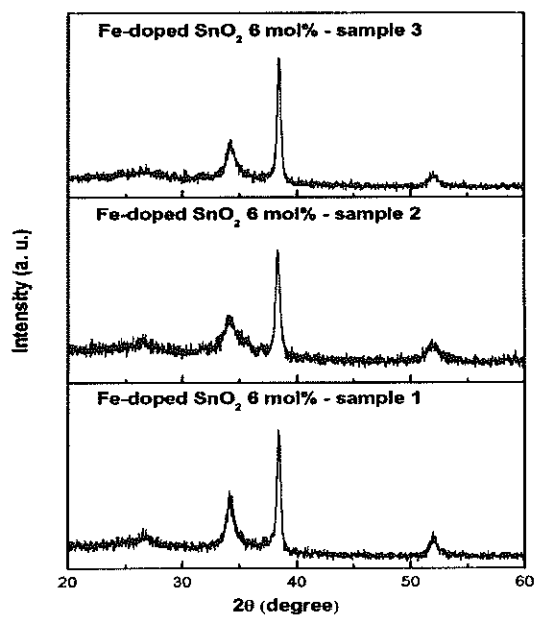
APPENDICES

APPENDIX A

Results of characterized studies

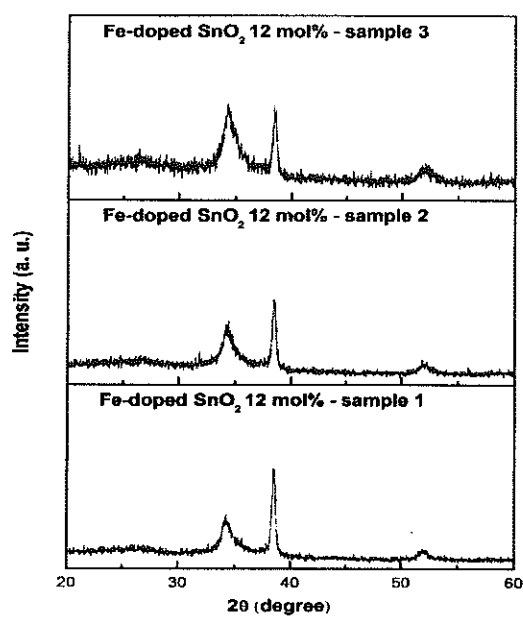


(a)

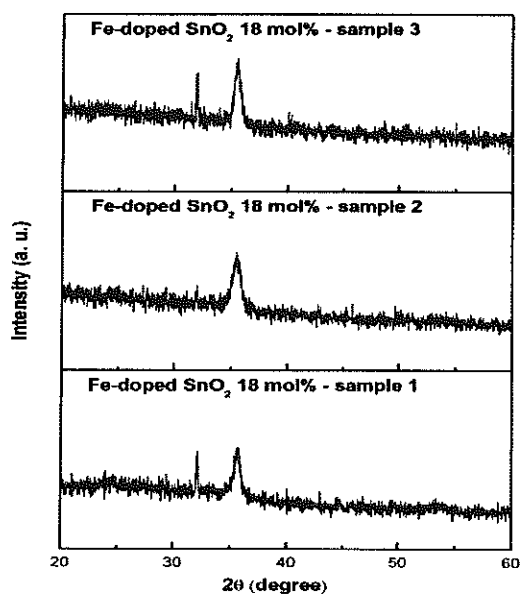


(b)

Figure A.1 X-ray diffraction patterns of thin films for various doping levels ($n = 3$);
(a) undoped SnO_2 and (b) Fe-doped SnO_2 6 mol%.



(a)



(b)

Figure A.2 X-ray diffraction patterns of thin films for various doping levels ($n = 3$);
(a) Fe-doped SnO_2 12 mol% and (b) Fe-doped SnO_2 18 mol%.

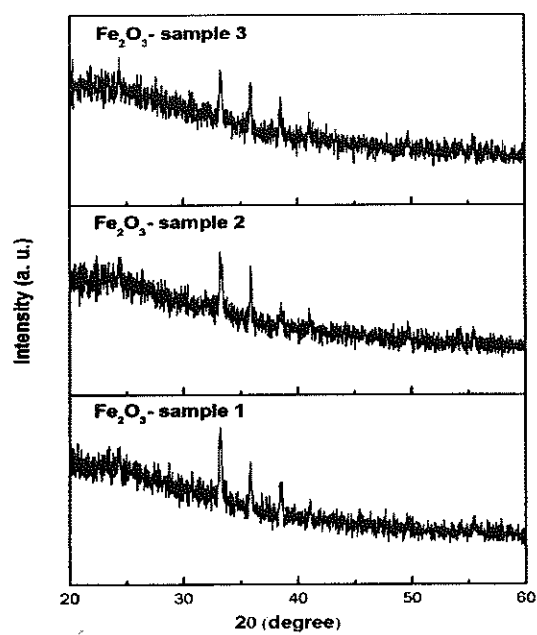
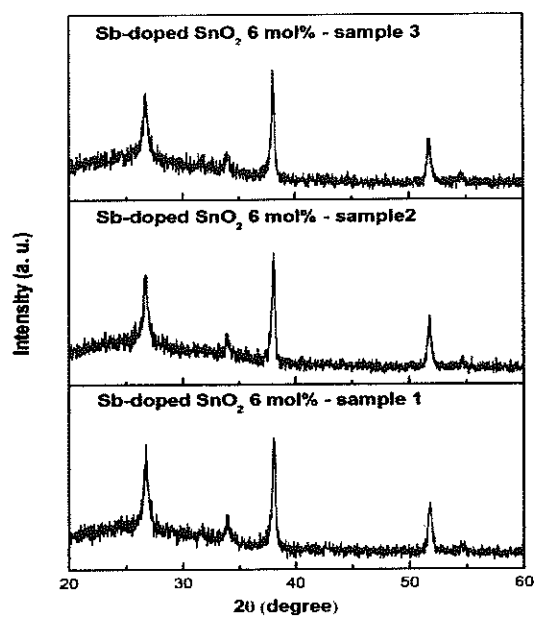
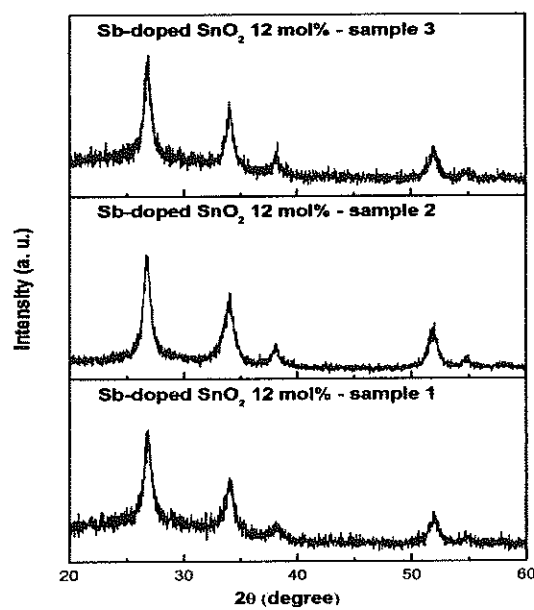


Figure A.3 X-ray diffraction patterns of Fe_2O_3 thin films ($n = 3$).



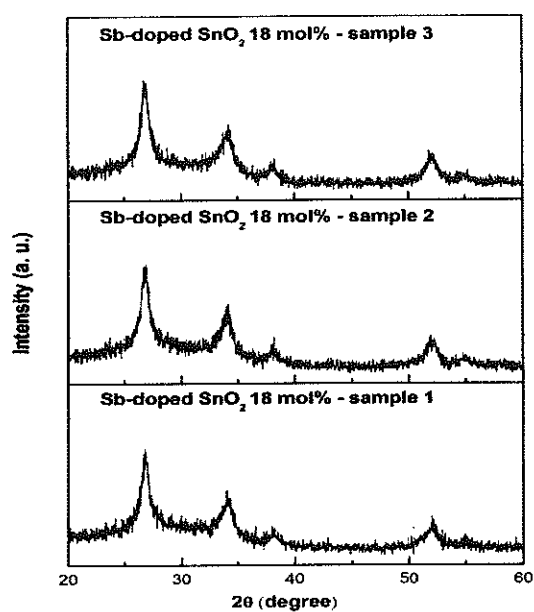
(a)



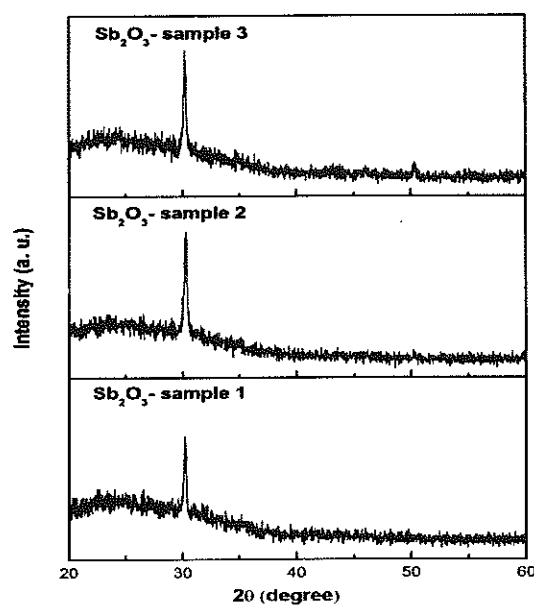
(b)

Figure A.4 X-ray diffraction patterns of thin films for various doping levels ($n = 3$);

(a) Sb-doped SnO_2 6 mol% and (b) Sb-doped SnO_2 12 mol%.



(a)



(b)

Figure A.5 X-ray diffraction patterns of thin films ($n = 3$); (a) Sb-doped SnO_2 18 mol% and (b) Sb_2O_3 film.

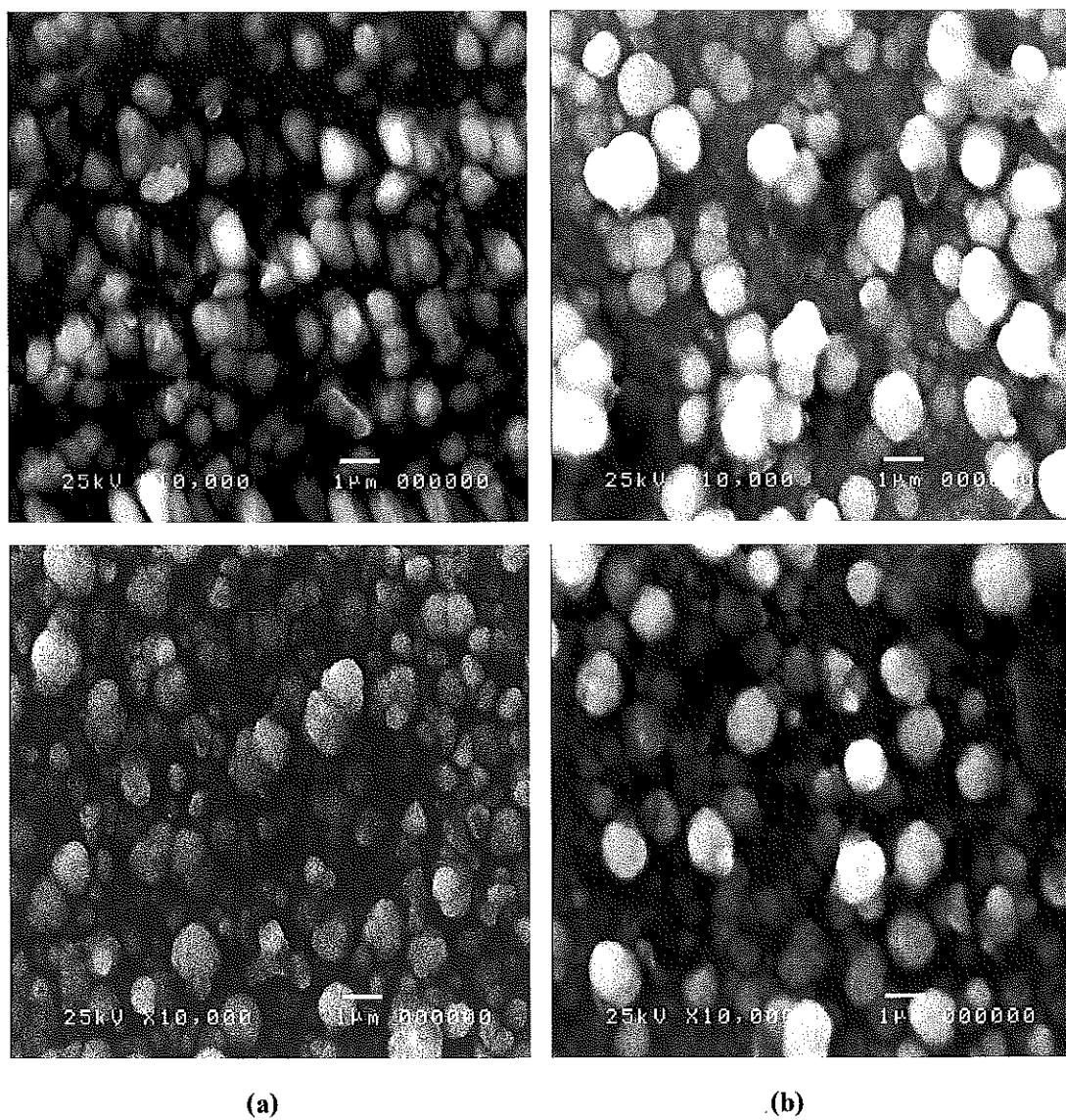


Figure A.6 SEM micrographs thin films ($n = 2$); (a) SnO₂ and (b) Fe-doped SnO₂ 6 mol%.

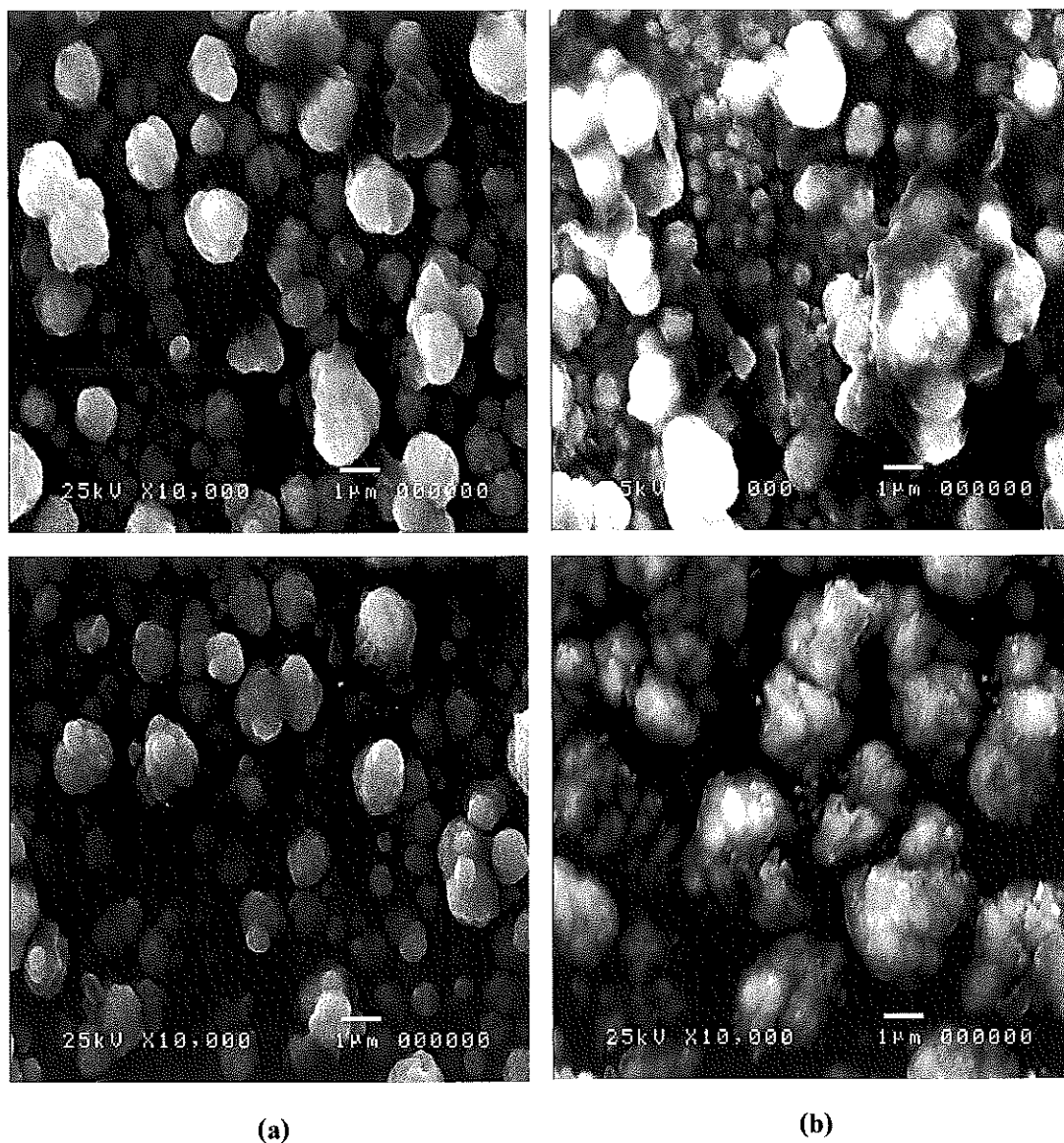


Figure A.7 SEM micrographs of SnO₂ thin films for different doping levels ($n = 2$);

(a) Fe-doped SnO₂ 12 mol% and (b) Fe-doped SnO₂ 18 mol%.

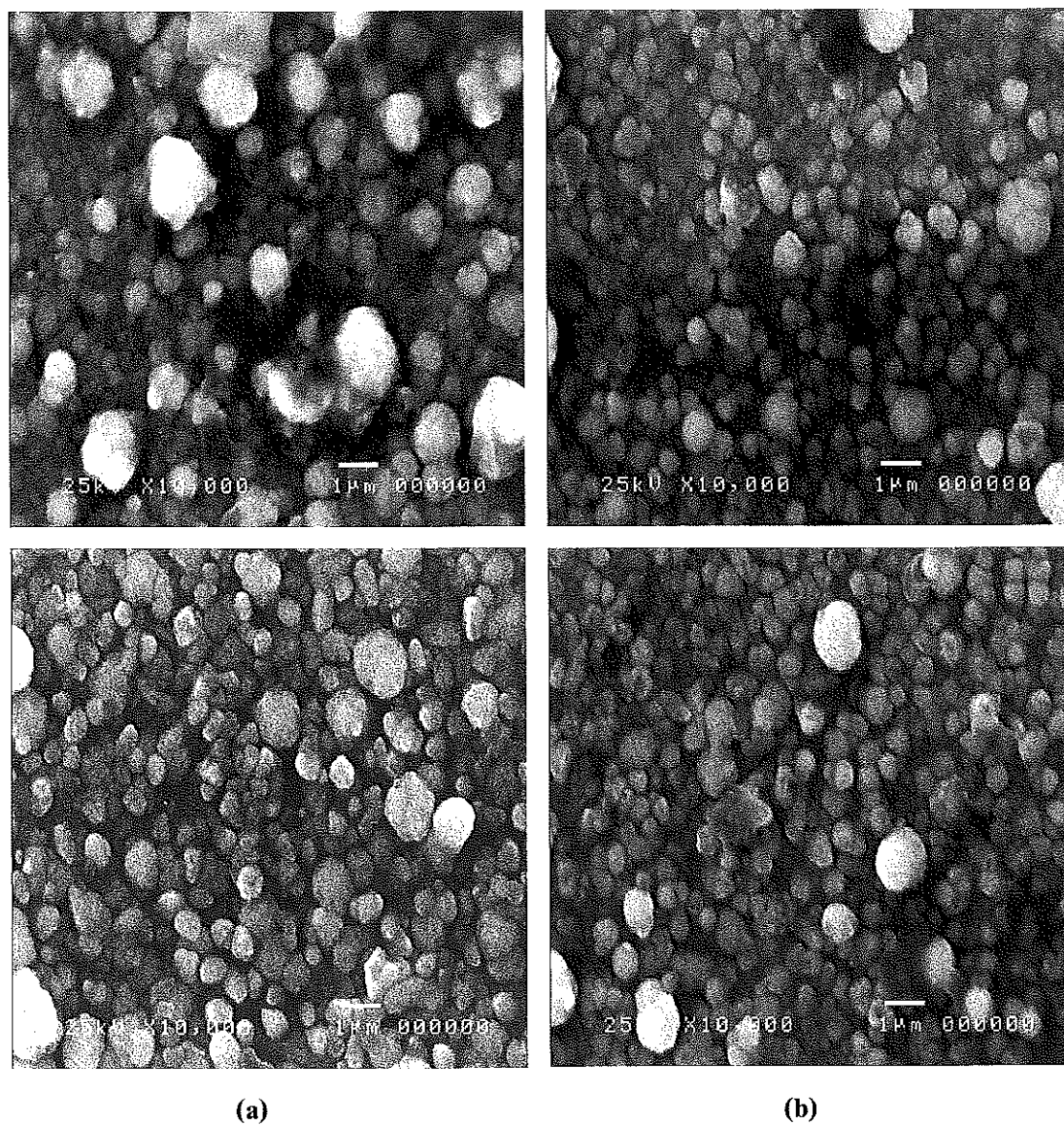


Figure A.8 SEM micrographs of SnO₂ thin films for different doping levels ($n = 2$);

(a) Sb-doped SnO₂ 6 mol% and (b) Sb-doped SnO₂ 12 mol%.

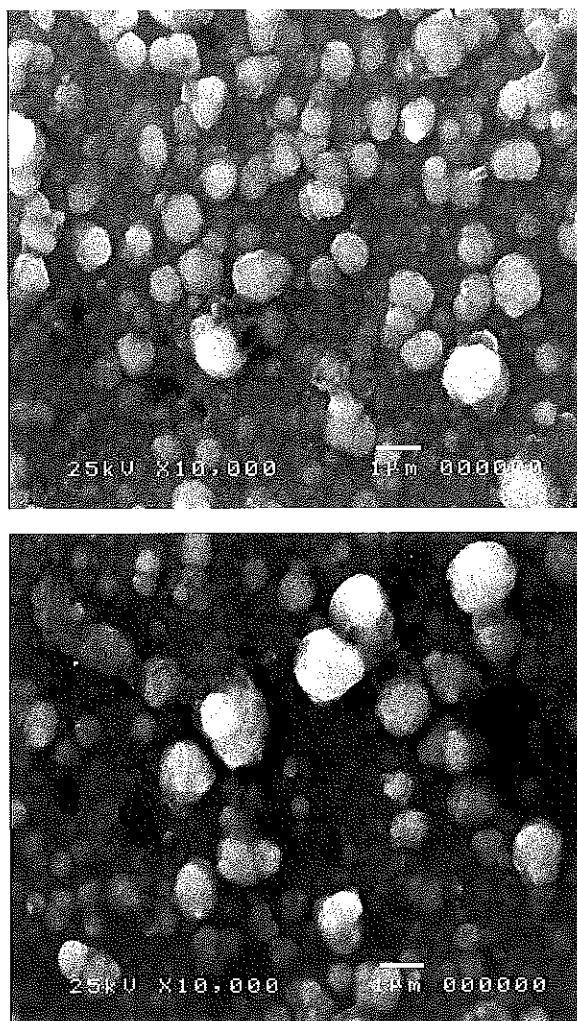


Figure A.9 SEM micrographs of Sb-doped SnO₂ 18 mol% thin films ($n = 2$).

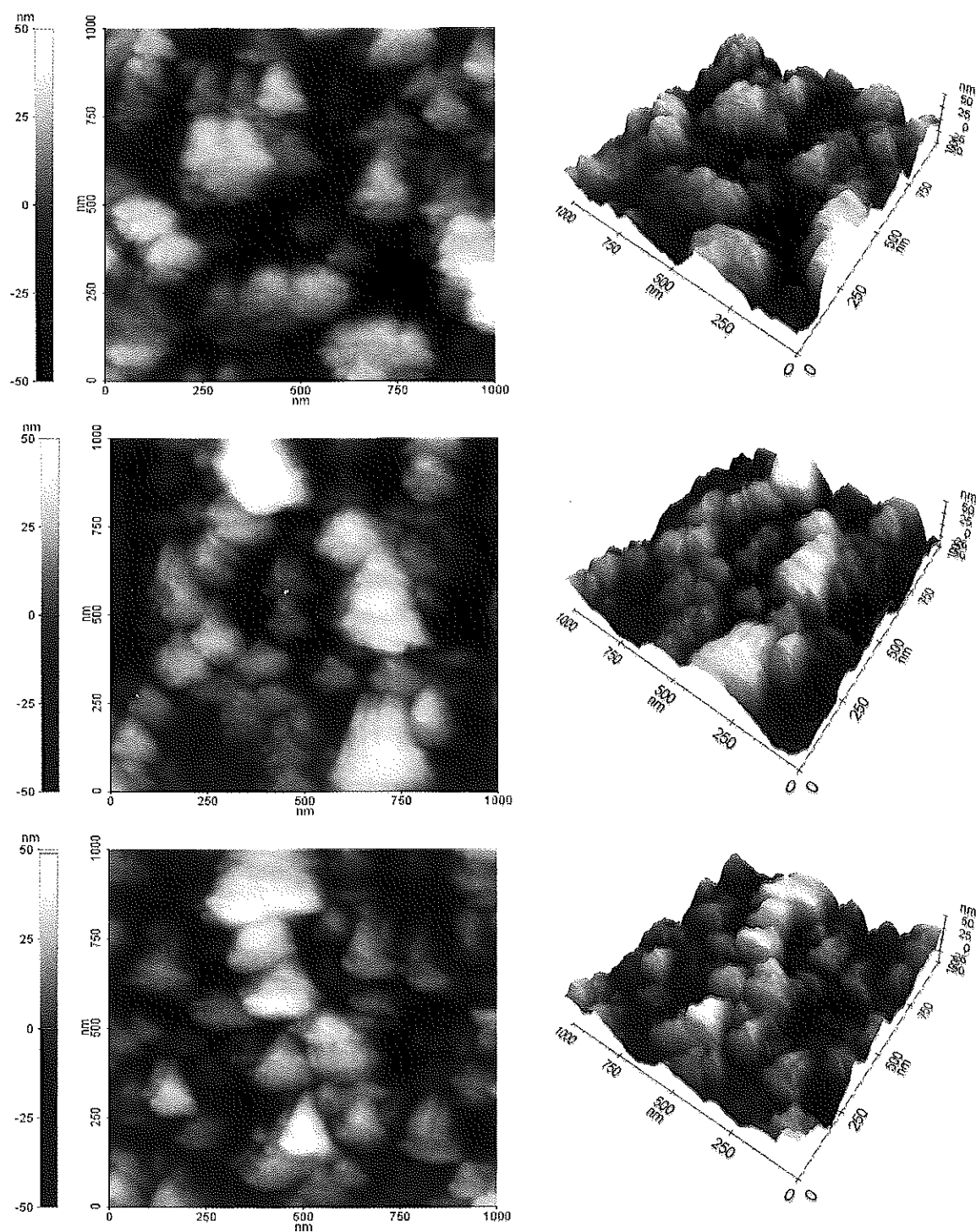


Figure A.10 2D (left) and 3D (right) AFM micrographs of undoped SnO_2 thin films ($n = 3$).

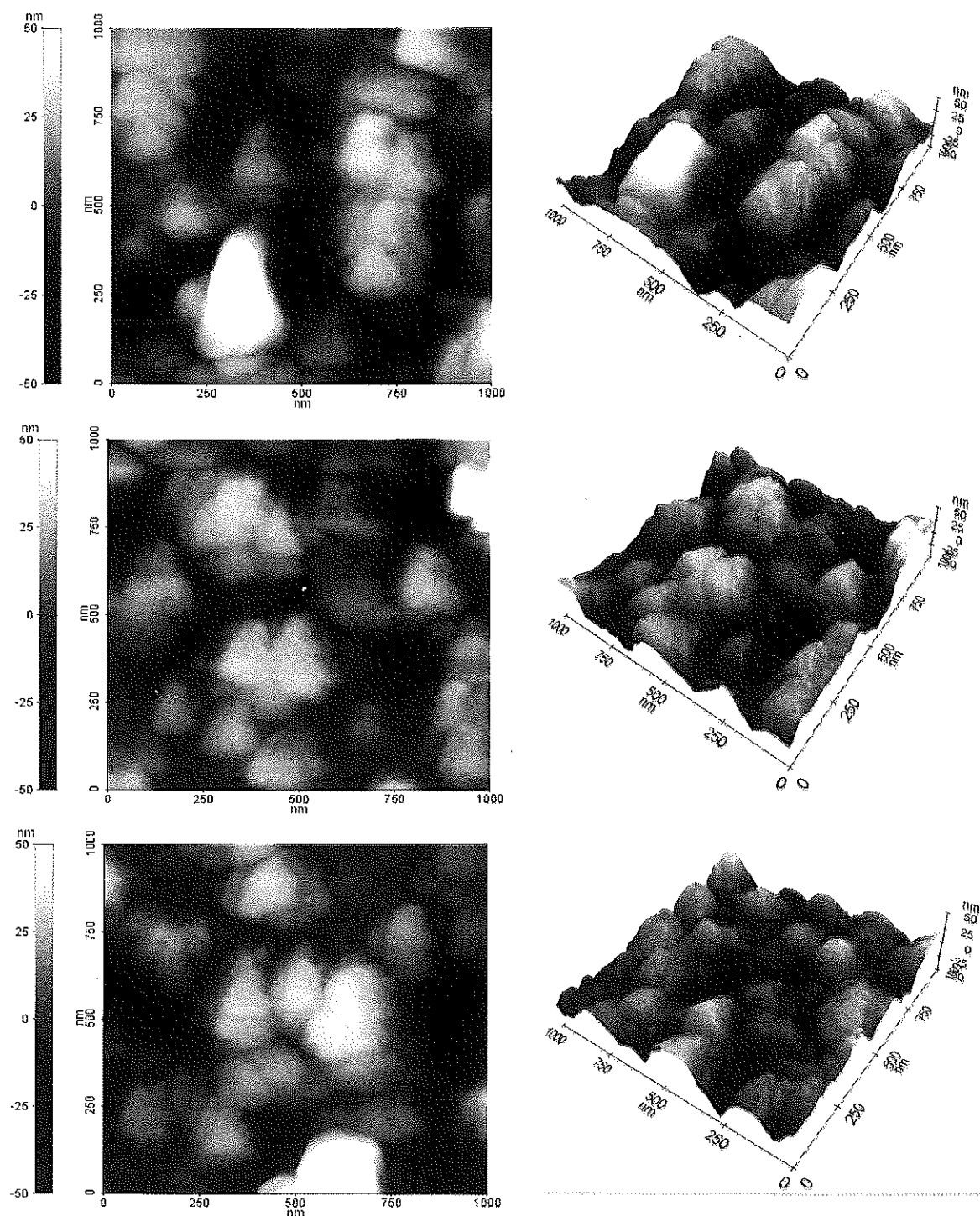


Figure A.11 2D (left) and 3D (right) AFM micrographs of Fe-doped SnO_2 6 mol% ($n = 3$).

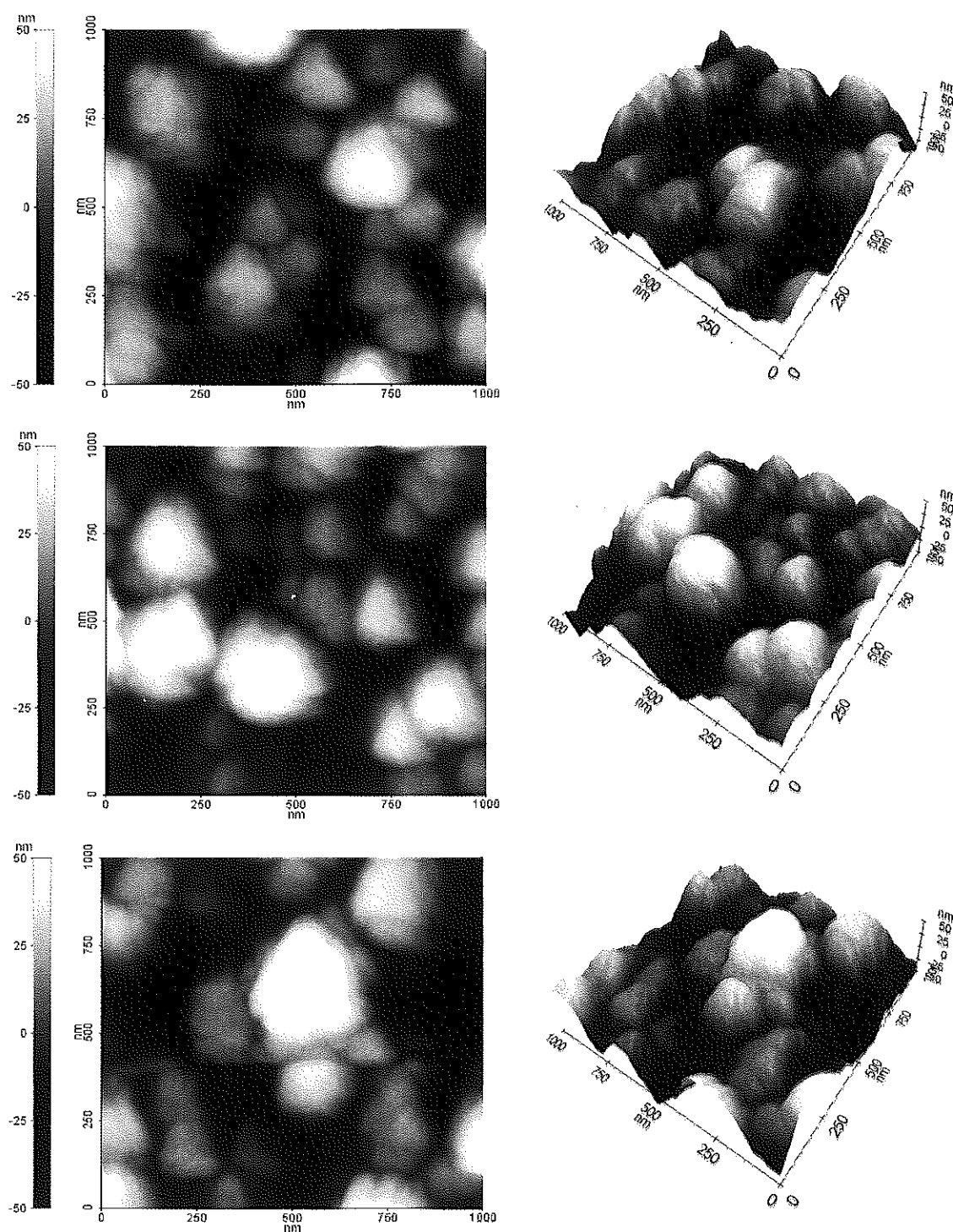


Figure A.12 2D (left) and 3D (right) AFM micrographs of Fe-doped SnO₂ 12 mol% thin films (n = 3).

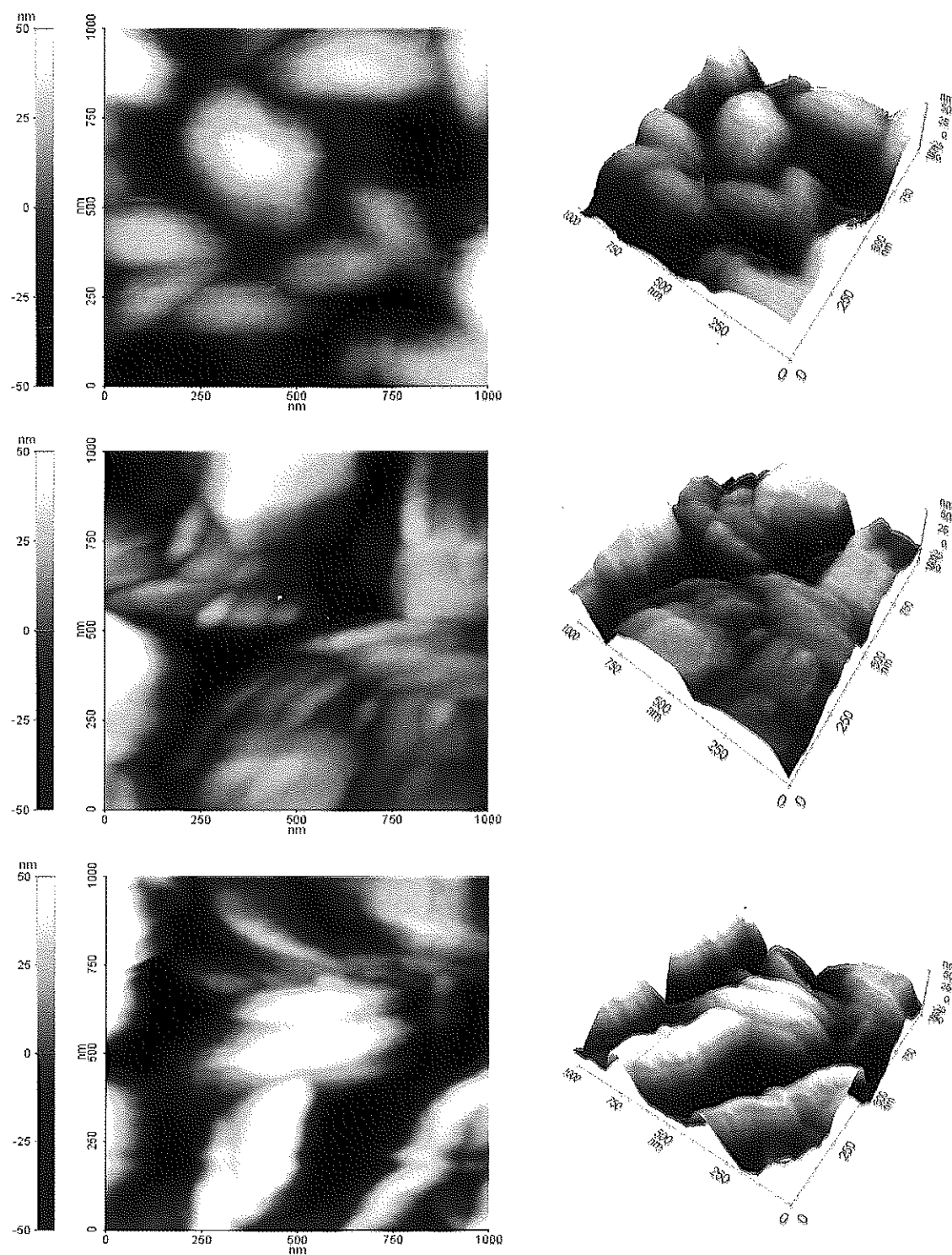


Figure A.13 2D (left) and 3D (right) AFM micrographs of Fe-doped SnO_2 18 mol% thin films ($n=3$).

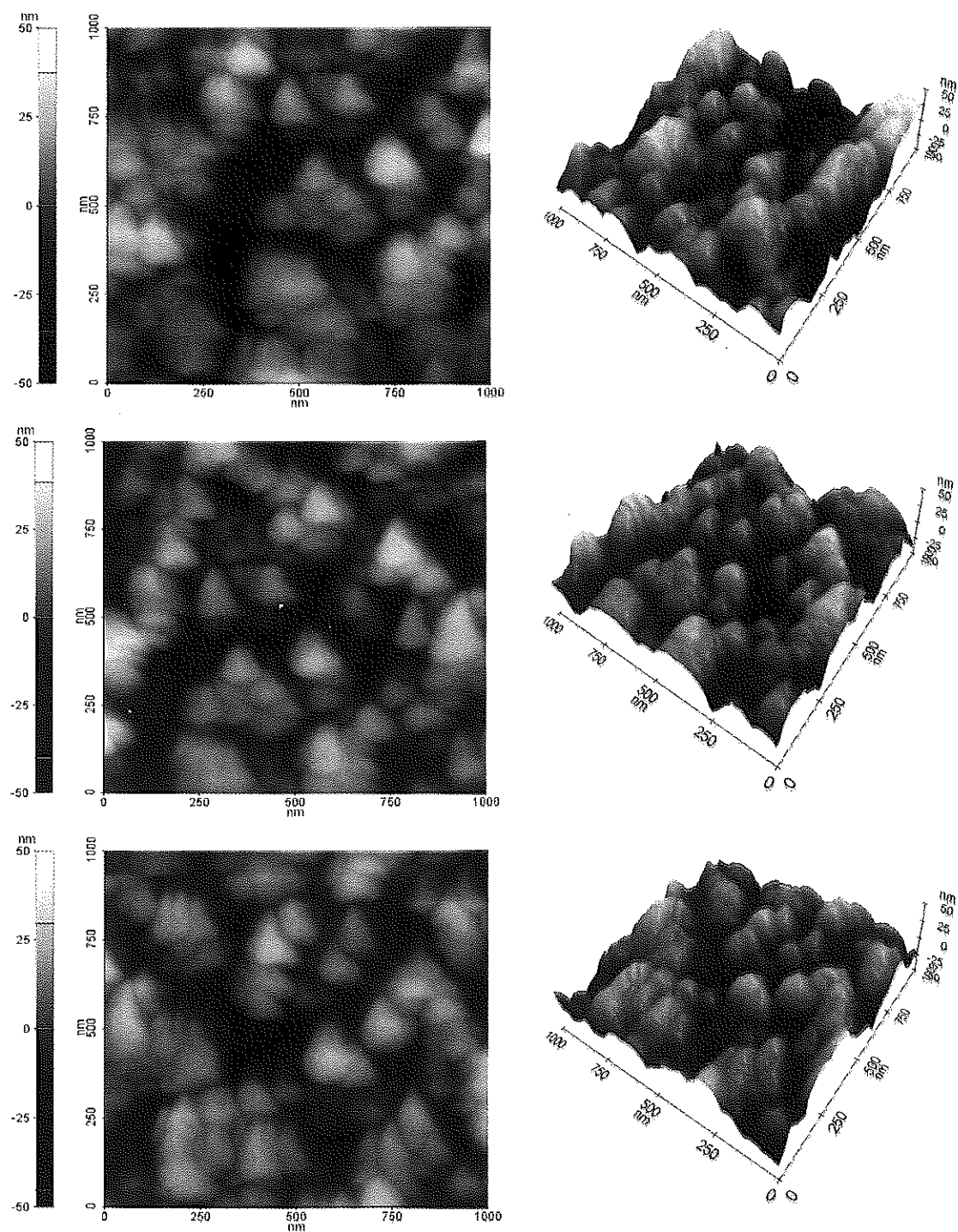


Figure A.14 2D (left) and 3D (right) AFM micrographs of Sb-doped SnO_2 6 mol% thin films ($n = 3$).

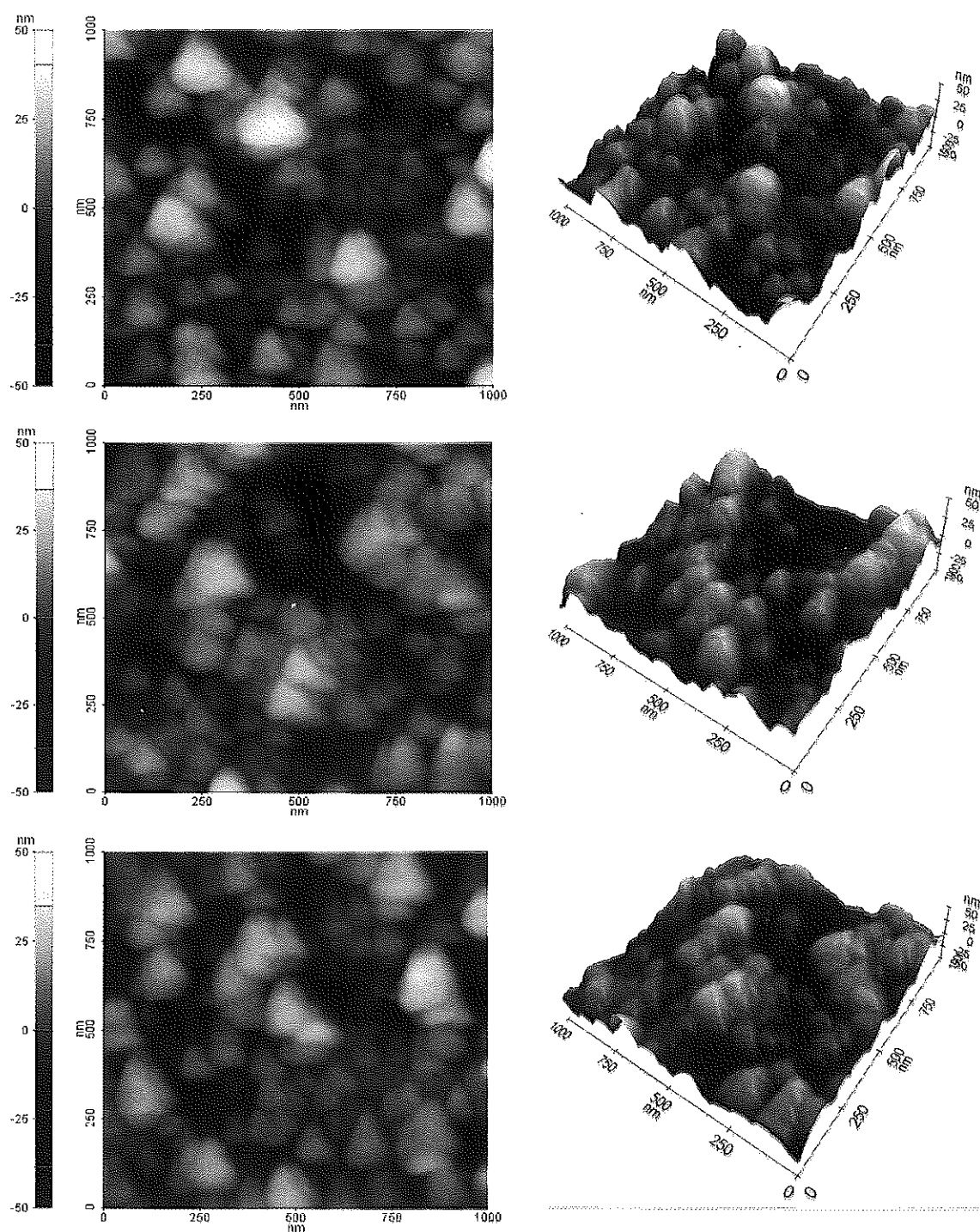


Figure A.15 2D (left) and 3D (right) AFM micrographs of Sb-doped SnO_2 12 mol% thin films ($n = 3$).

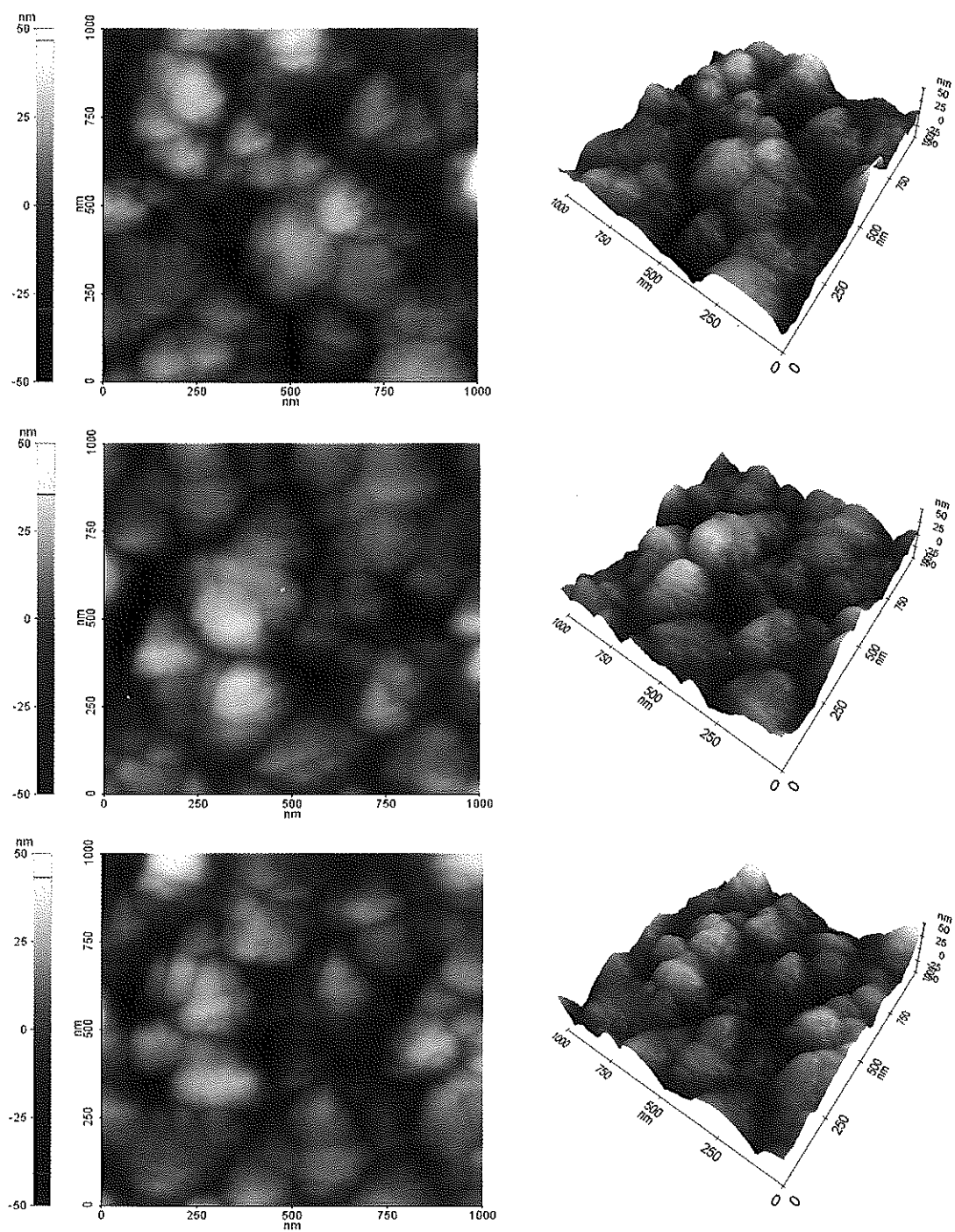
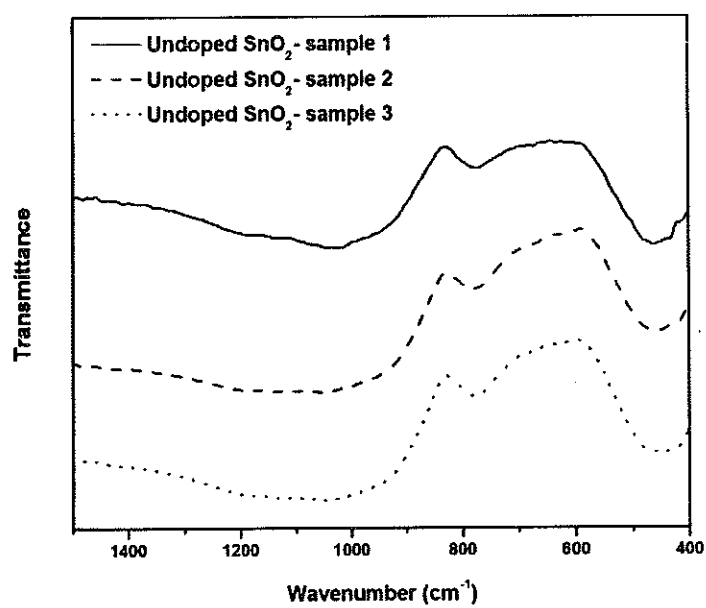
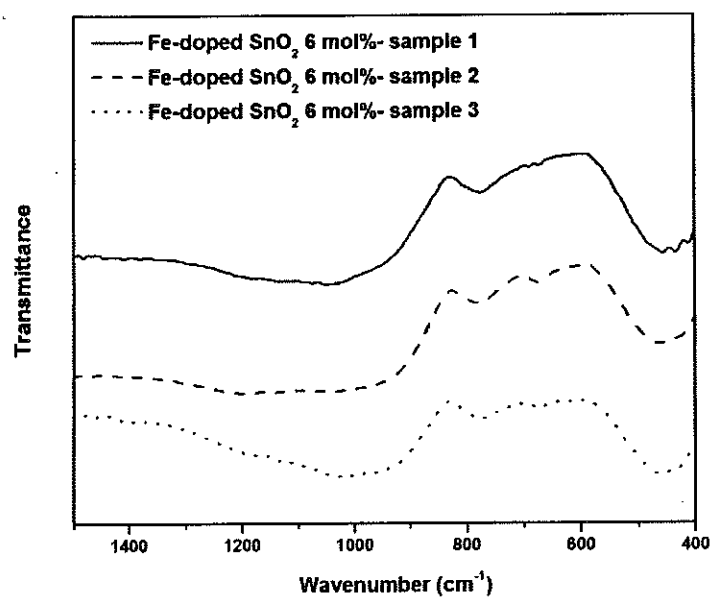


Figure A.16 2D (left) and 3D (right) AFM micrographs of Sb-doped SnO_2 18 mol% thin films ($n = 3$).

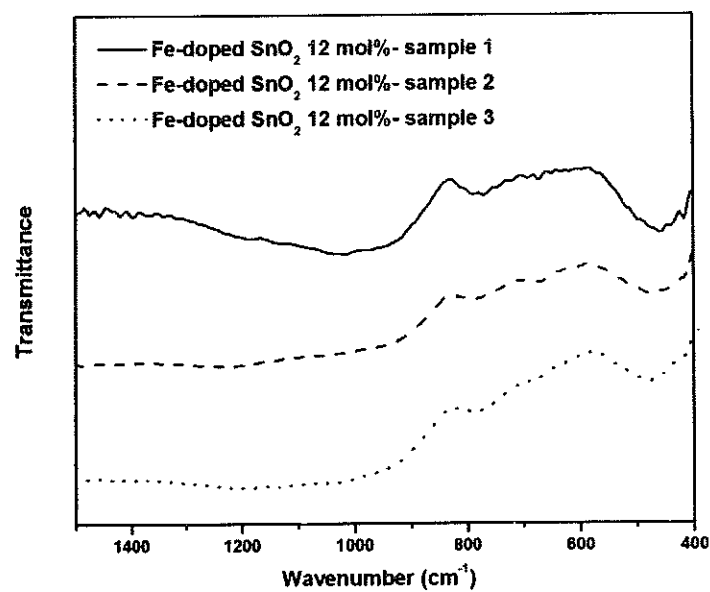


(a)

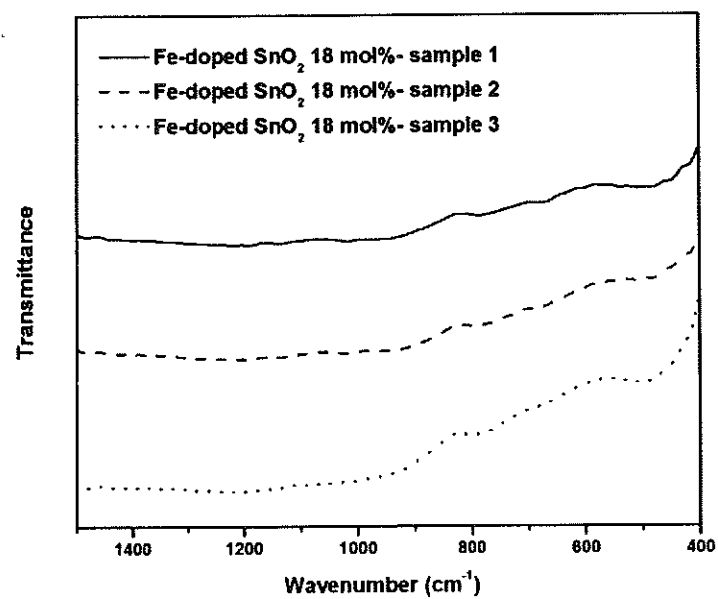


(b)

Figure A.17 FT-IR spectra of films ($n = 3$); (a) undoped SnO_2 and (b) Fe-doped SnO_2 6 mol%.

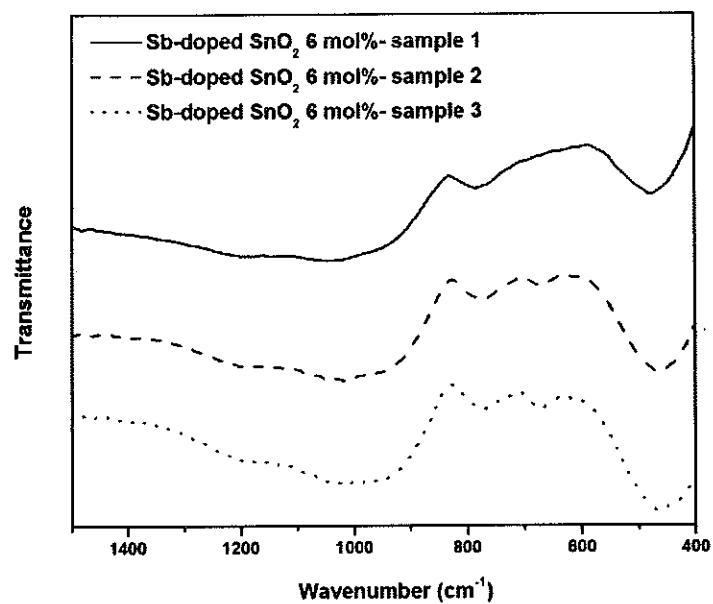


(a)

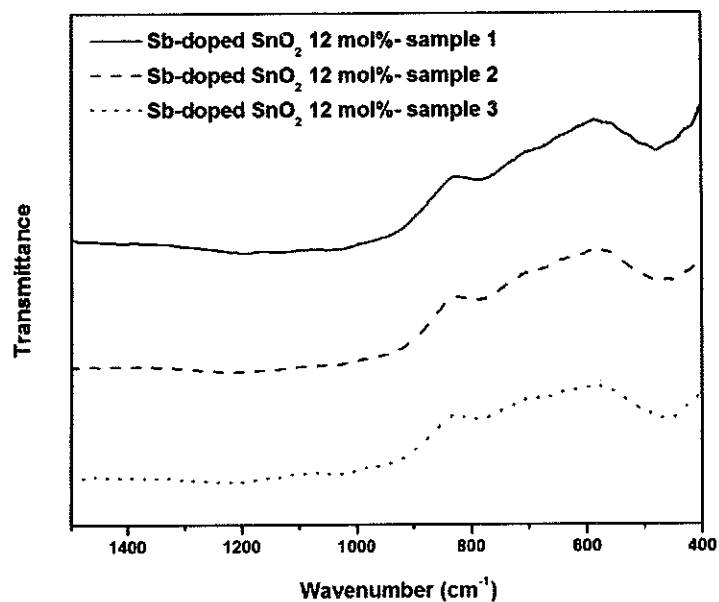


(b)

Figure A.18 FT-IR spectra of films ($n = 3$); (a) Fe-doped SnO_2 12 mol% and (b) Fe-doped SnO_2 18 mol%.



(a)



(b)

Figure A.19 FT-IR spectra of films ($n = 3$); (a) Sb-doped SnO_2 6 mol% and (b) Sb-doped SnO_2 12 mol%.

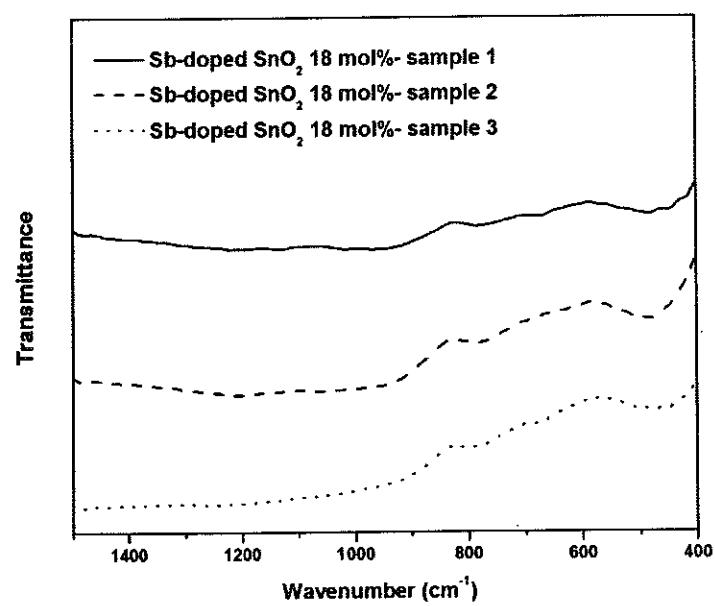
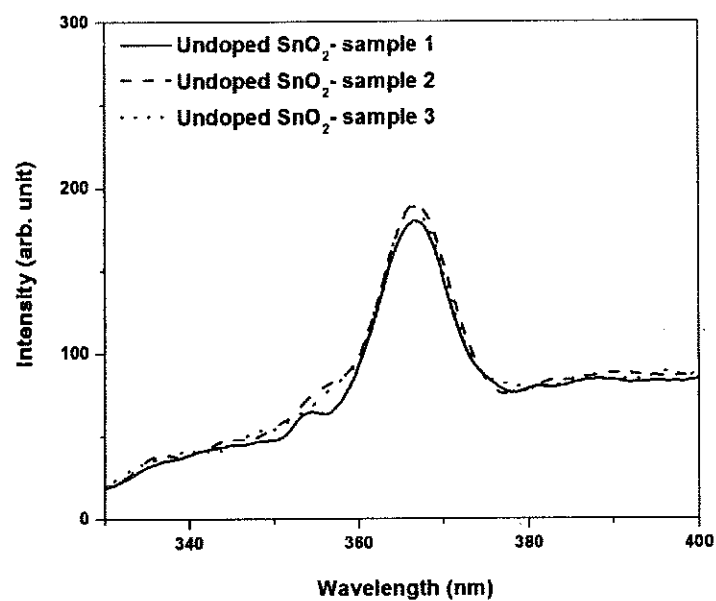
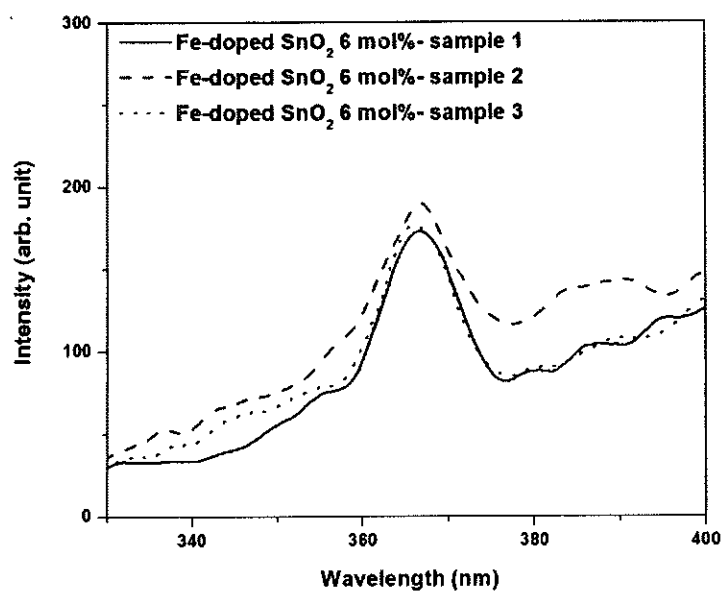


Figure A.20 FT-IR spectra of Sb-doped SnO₂ 18 mol% thin films ($n = 3$).

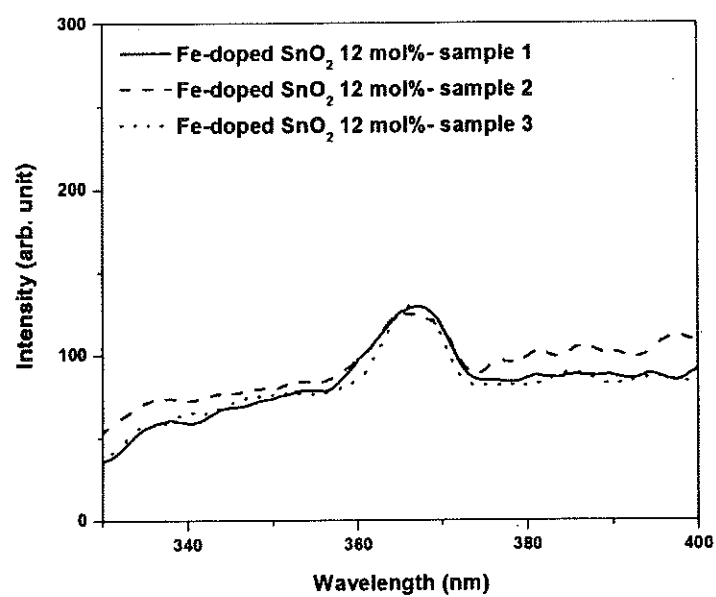


(a)

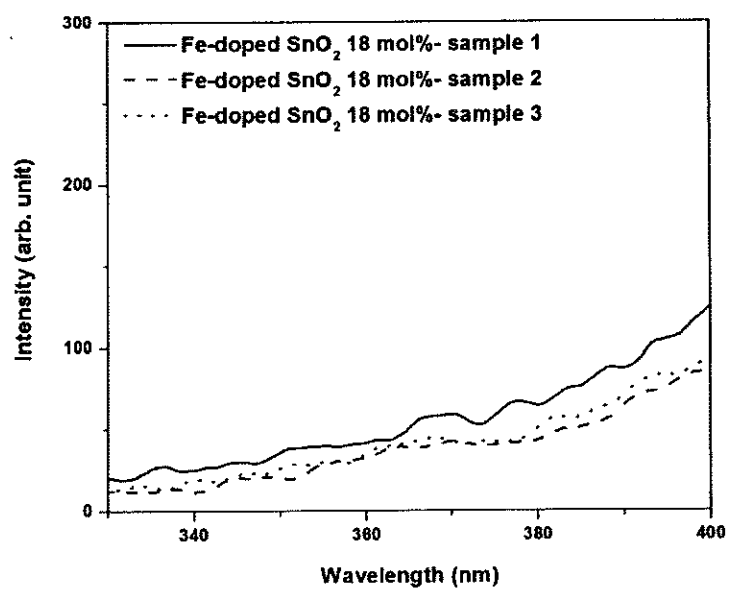


(b)

Figure A.21 PL spectra of films ($n = 3$); (a) undoped SnO_2 and (b) Fe-doped SnO_2 6 mol%.

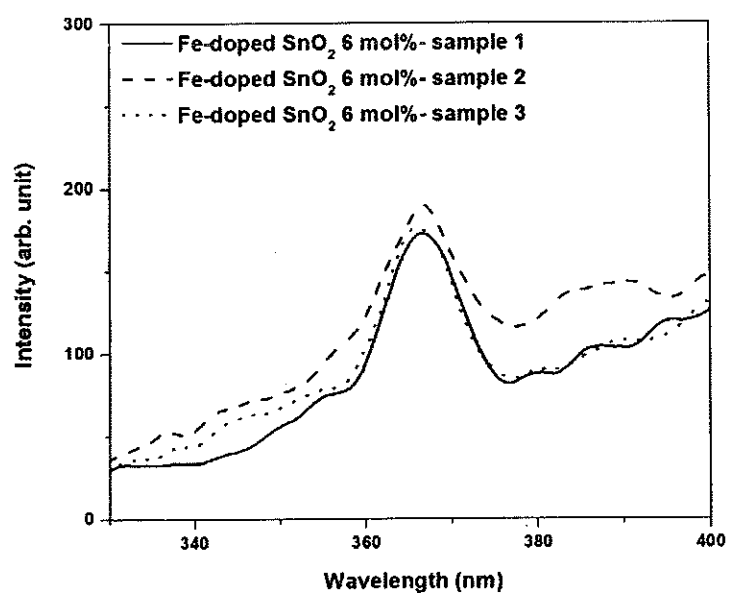


(a)

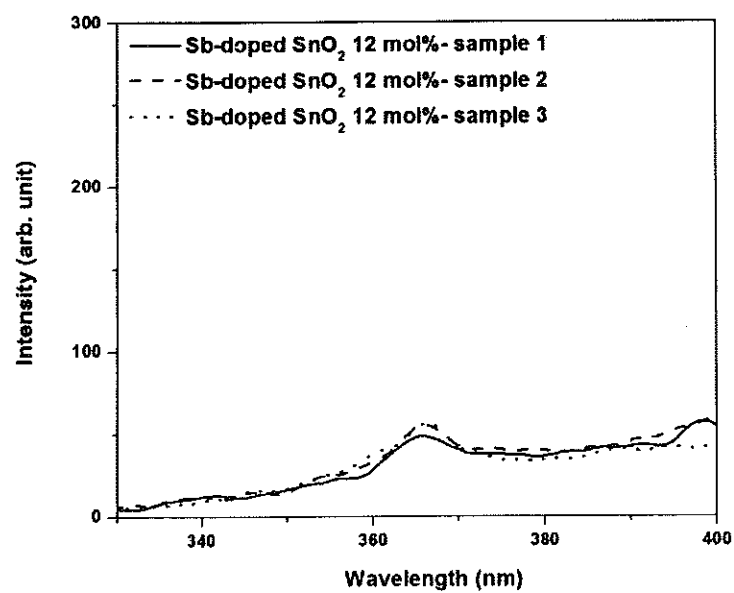


(b)

Figure A.22 PL spectra of films ($n = 3$); (a) Fe-doped SnO_2 12 mol% and (b) Fe-doped SnO_2 18 mol%.



(a)



(b)

Figure A.23 PL spectra of films ($n = 3$); (a) Sb-doped SnO_2 6 mol% and (b) Sb-doped SnO_2 12 mol%.

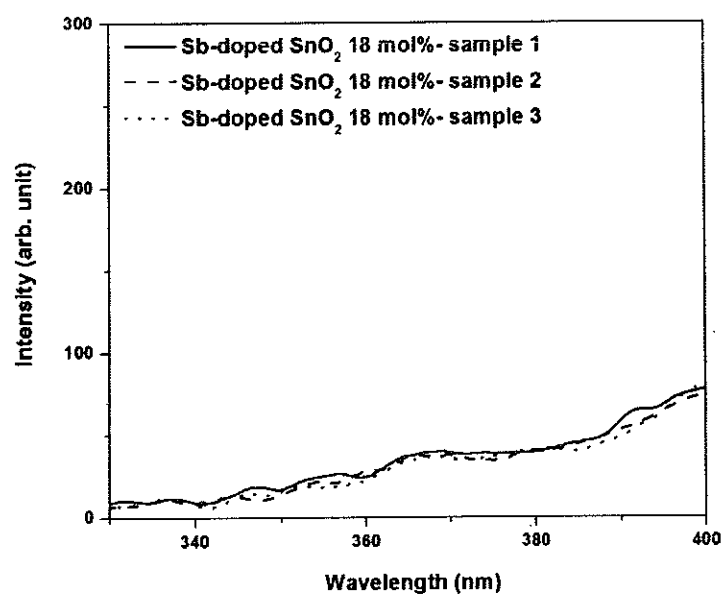
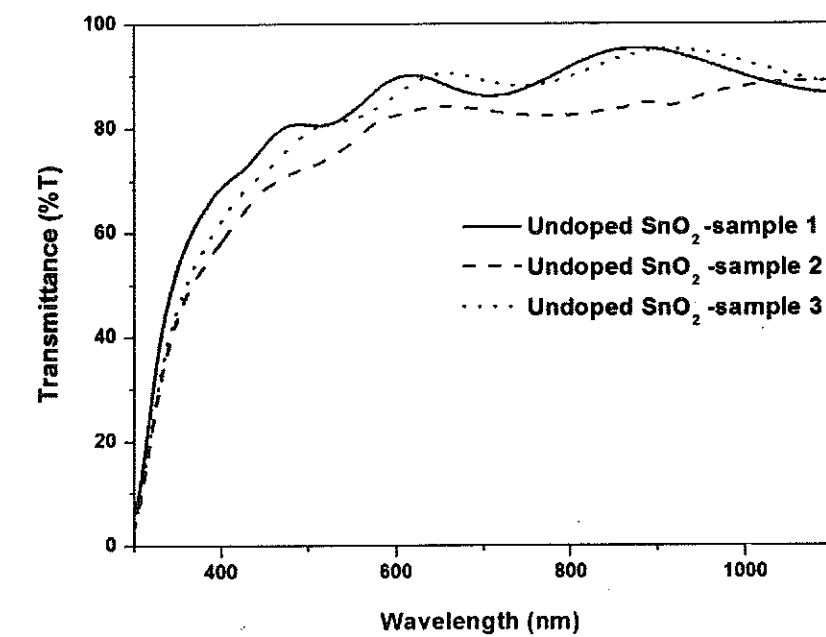
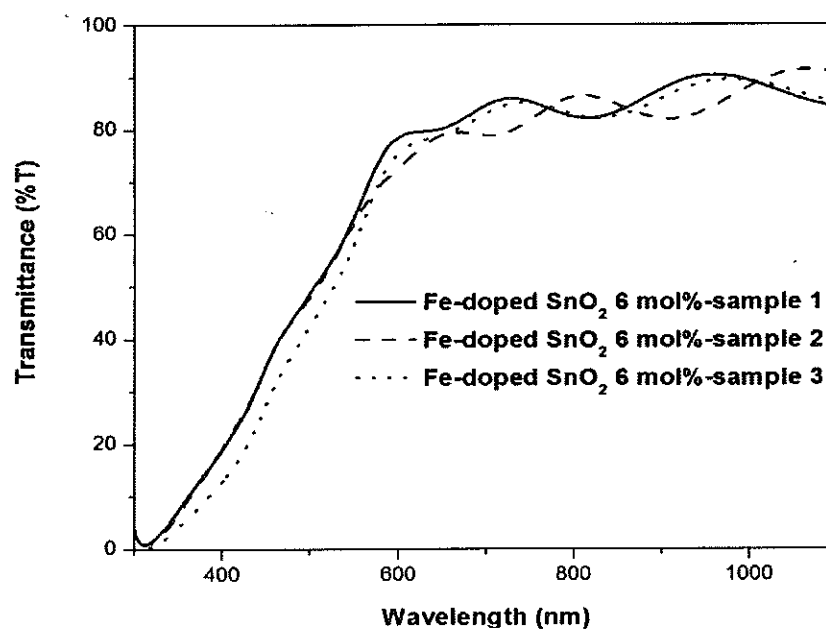


Figure A.24 PL spectra of Sb-doped SnO₂ 18 mol% thin films ($n = 3$).

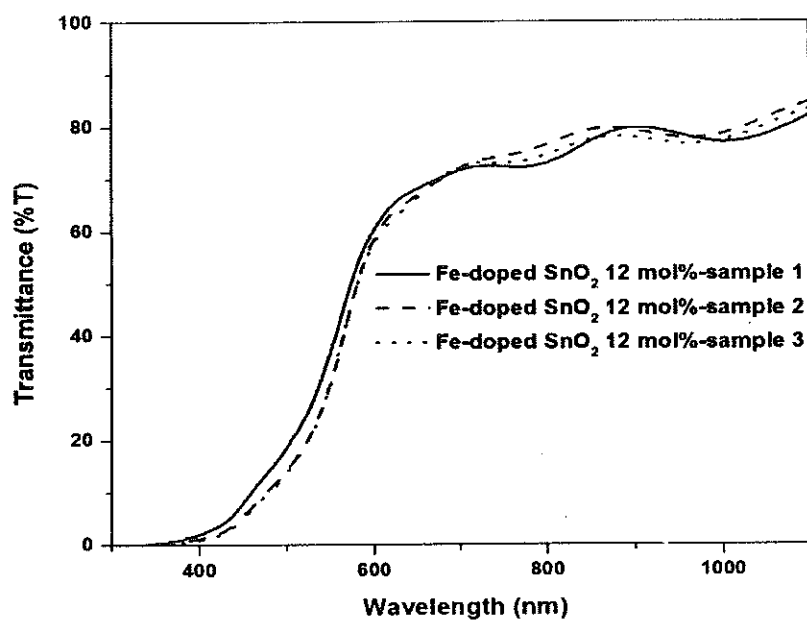


(a)

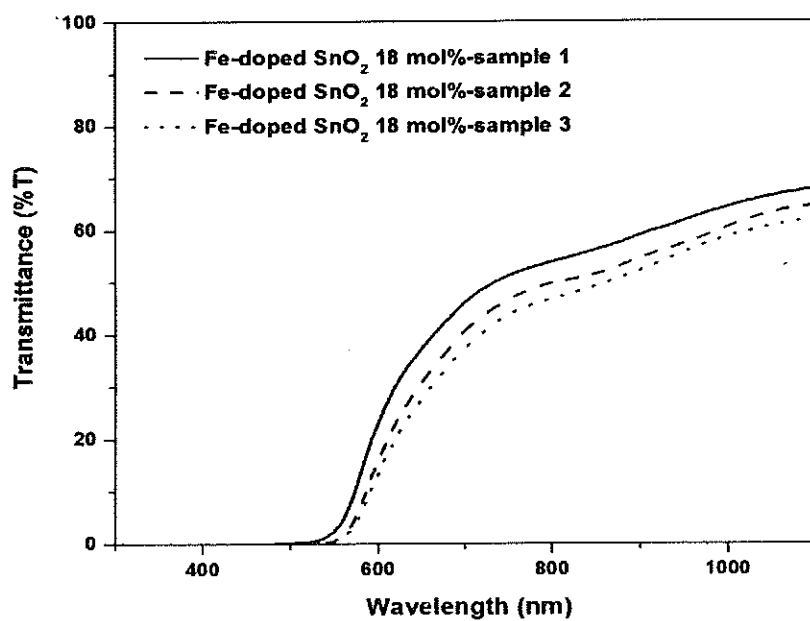


(b)

Figure A.25 Optical transparencies of films ($n = 3$); (a) undoped SnO_2 and (b) 6 mol% Fe-doped SnO_2 .

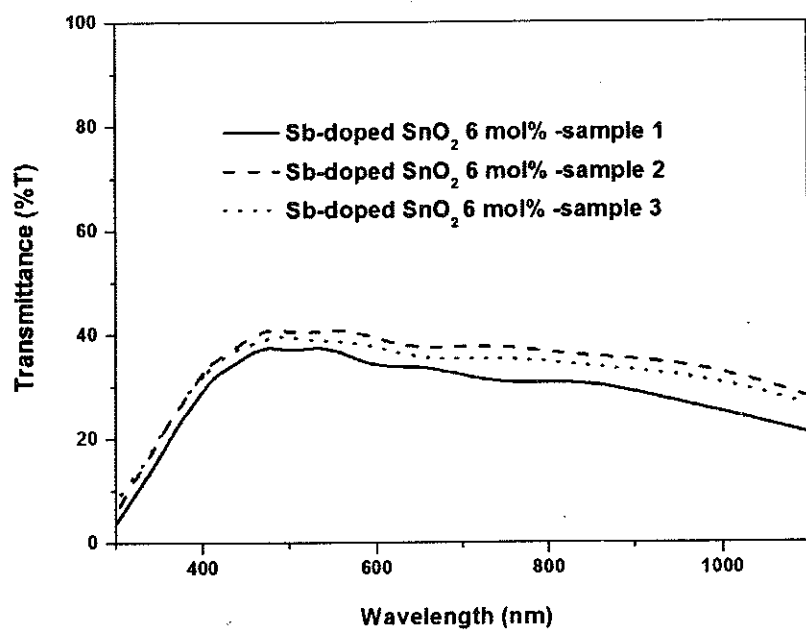


(a)

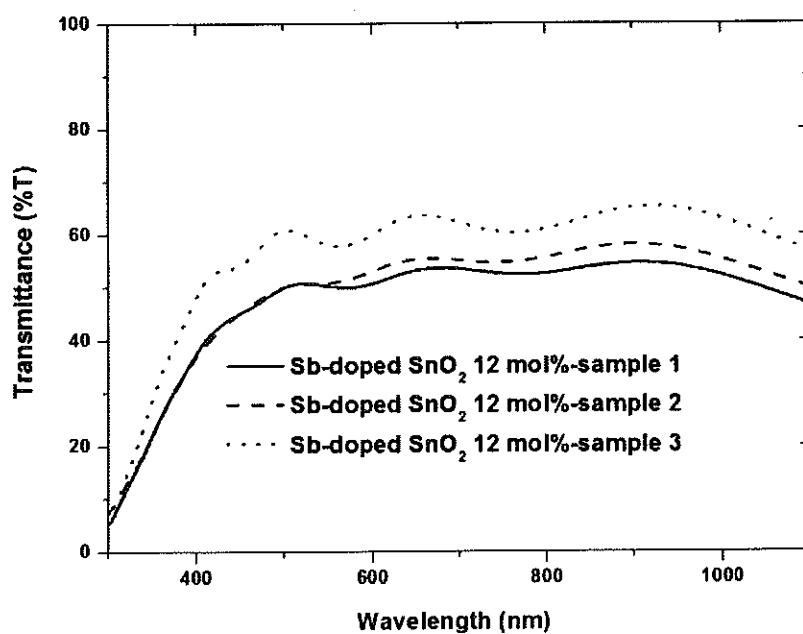


(b)

Figure A.26 Optical transparencies of films ($n = 3$); (a) Fe-doped SnO_2 12 mol% and (b) Fe-doped SnO_2 18 mol%.



(a)



(b)

Figure A.27 Optical transparencies of films ($n = 3$); (a) Sb-doped SnO₂ 6 mol% and (b) Sb-doped SnO₂ 12 mol%.

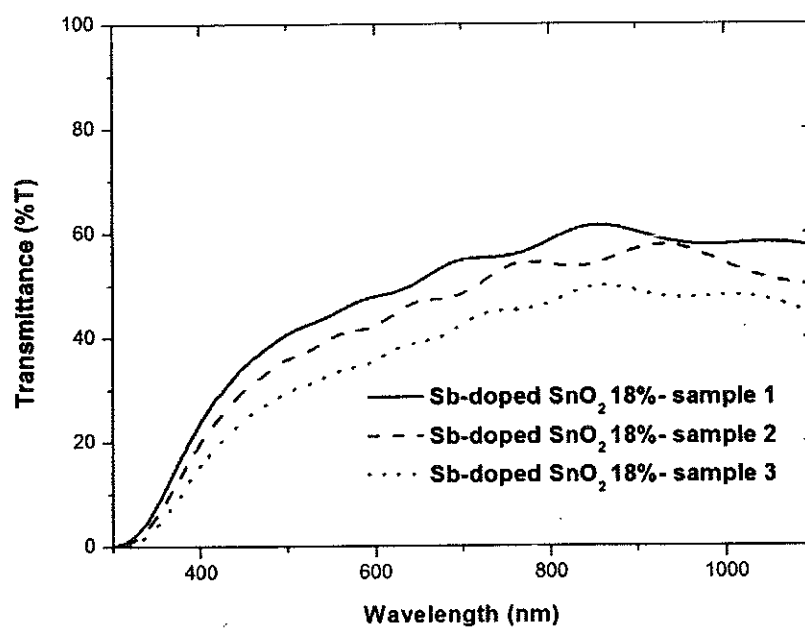
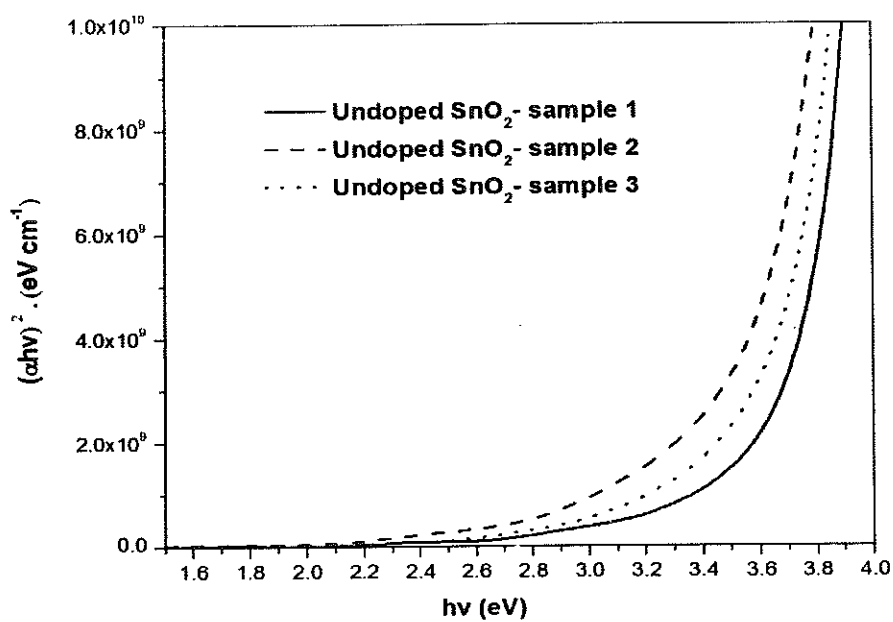
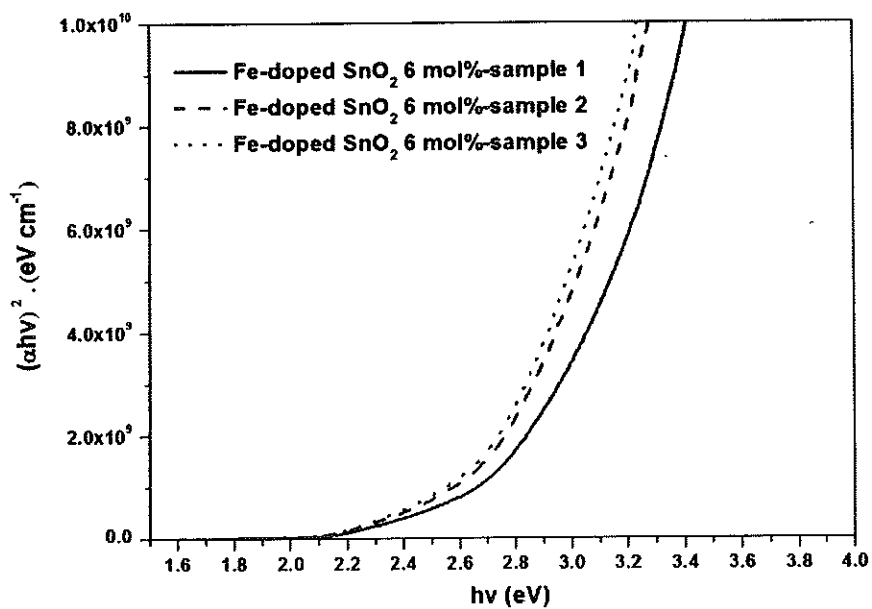


Figure A.28 Optical transparencies of Sb-doped SnO₂ 18 mol% thin films (n = 3).

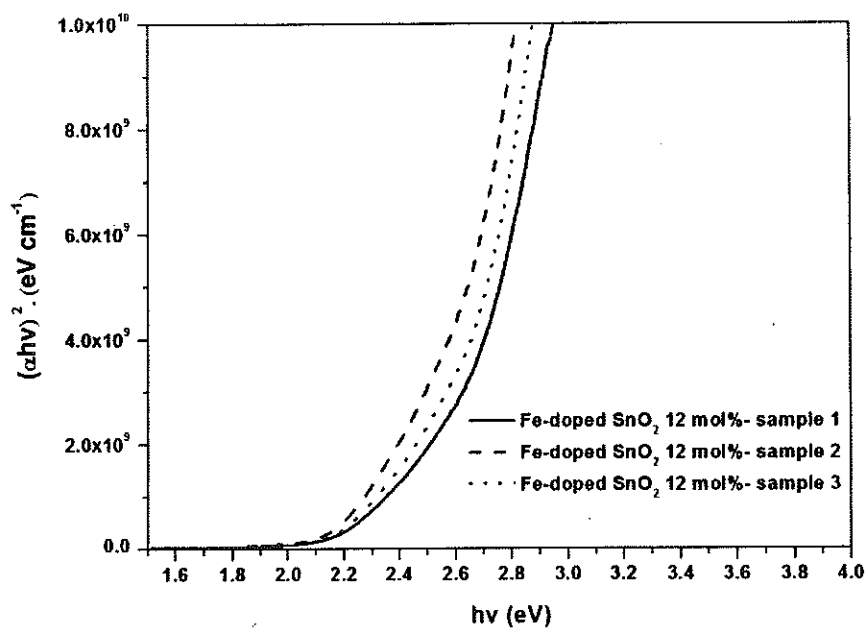


(a)

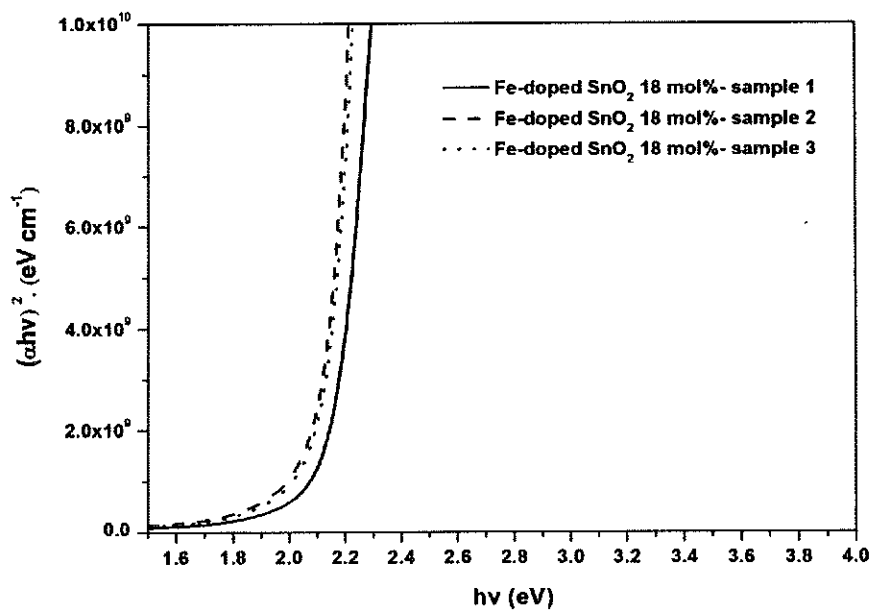


(b)

Figure A.29 Optical band gaps of films ($n = 3$); (a) undoped SnO_2 and (b) Fe-doped SnO_2 6 mol%.

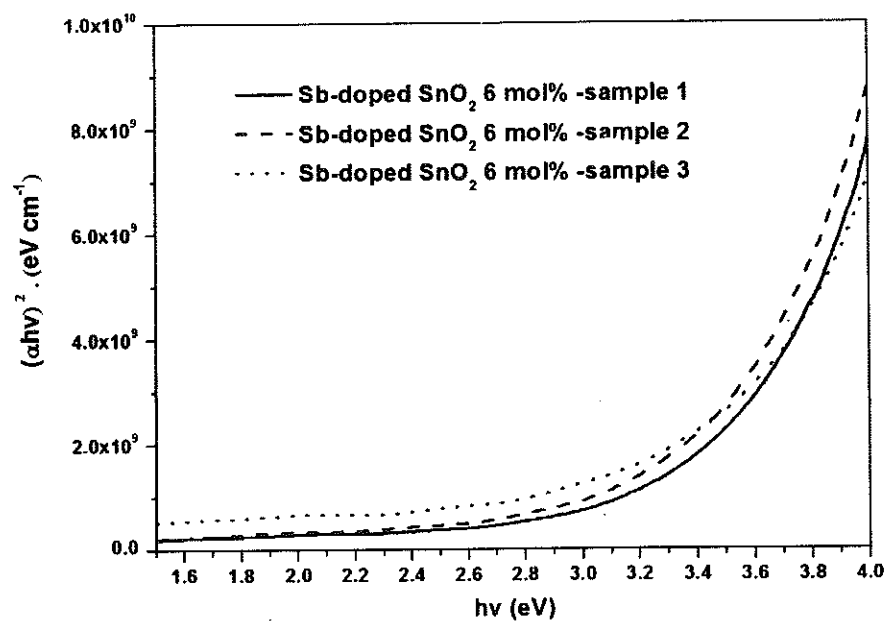


(a)

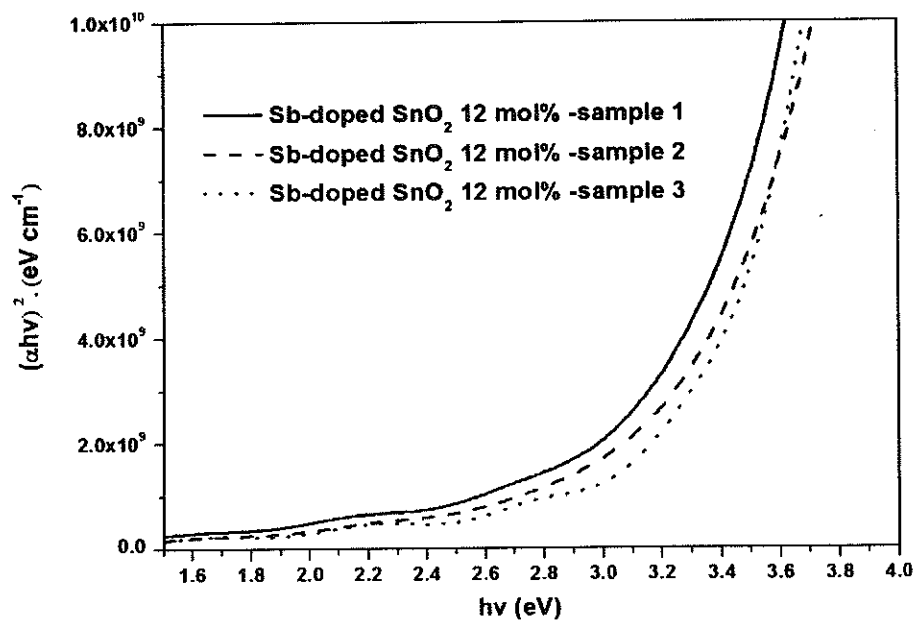


(b)

Figure A.30 Optical band gaps of films ($n = 3$); (a) Fe-doped SnO_2 12 mol% and (b) Fe-doped SnO_2 18 mol%.



(a)



(b)

Figure A.31 Optical band gaps of films ($n = 3$); (a) Sb-doped SnO₂ 6 mol% and
(b) Sb-doped SnO₂ 12 mol%.

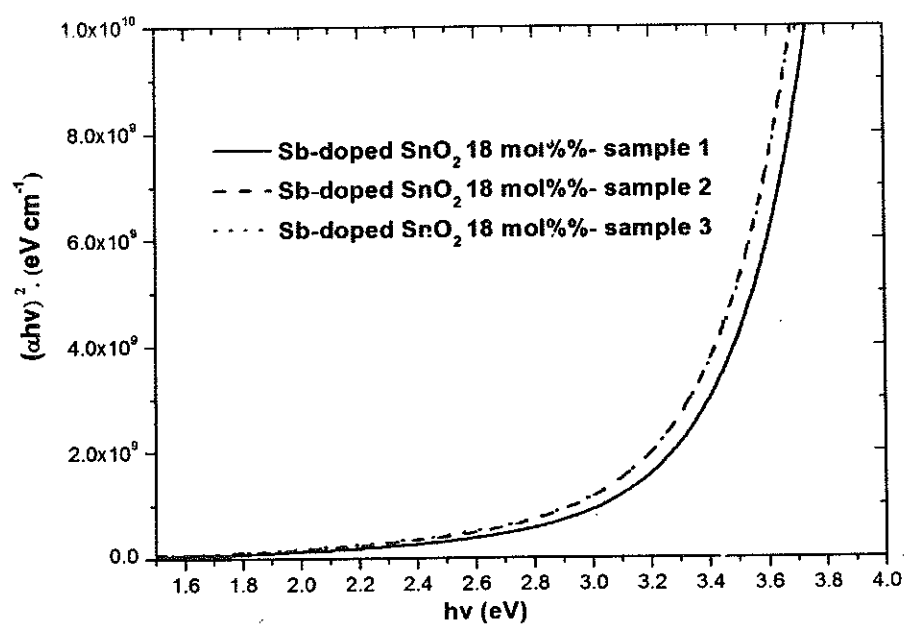


Figure A.32 Optical band gaps of Sb-doped SnO_2 18 mol% thin films ($n = 3$).

APPENDIX B

**Estimation of photoluminescence emission intensity of prepared thin films
with background correction method**

Photoluminescence emission intensity was significant factor which used for study of some thin films properties. However, in case of background intensity of emission spectra were not balanced, background correction method was important to correction of data. Estimation of photoluminescence emission intensity of thin films with background correction method was obtained by equation B.1.

$$I = I_1 - [I_3 + (I_2 - I_3) \left(\frac{\lambda_3 - \lambda_1}{\lambda_3 - \lambda_2} \right)] \quad (\text{B.1})$$

where; I is the photoluminescence emission intensity of thin films

λ_1 , λ_2 and λ_3 are emission wavelength of films at middle of spectrum, base of spectrum in left and right side, respectively

I_1 , I_2 and I_3 are emission intensity of films at λ_1 , λ_2 and λ_3 , respectively

The positions of presented symbols were shown in Figure B.1.

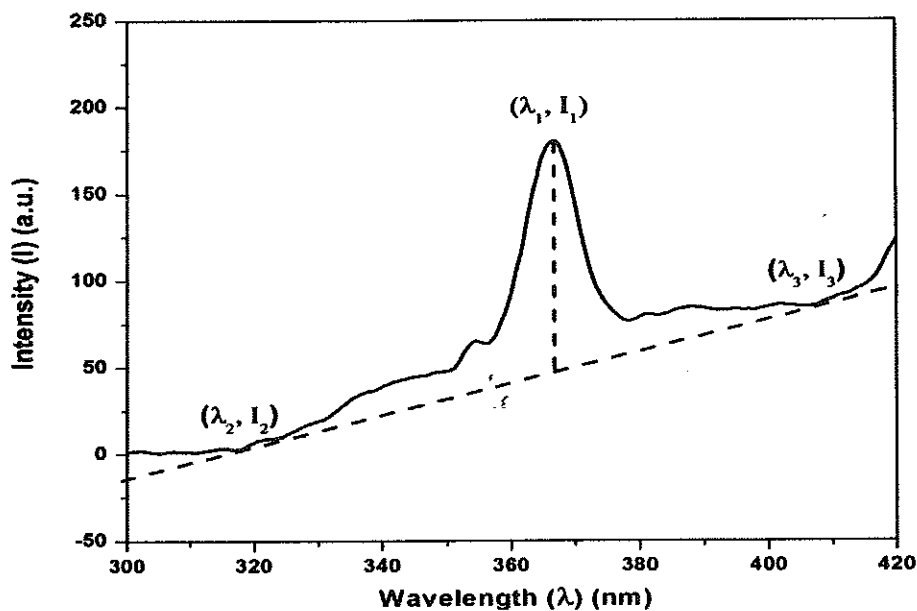


Figure B.1 The positions of presented symbols in background correction equation.

The example of photoluminescence emission intensity estimation with background correction method for SnO_2 sample was shown in following steps;

1. From photoluminescence emission spectrum of SnO_2 sample, data from emission spectrum were shown in Table 1B and applied in Figure B.2.

Table 1B data from emission spectrum of SnO_2 sample

Symbols	Data values	
	Emission wavelength (nm)	Emission intensity (a. u.)
λ_1	363	-
λ_2	318	-
λ_3	408	-
I_1	-	142
I_2	-	3
I_3	-	86

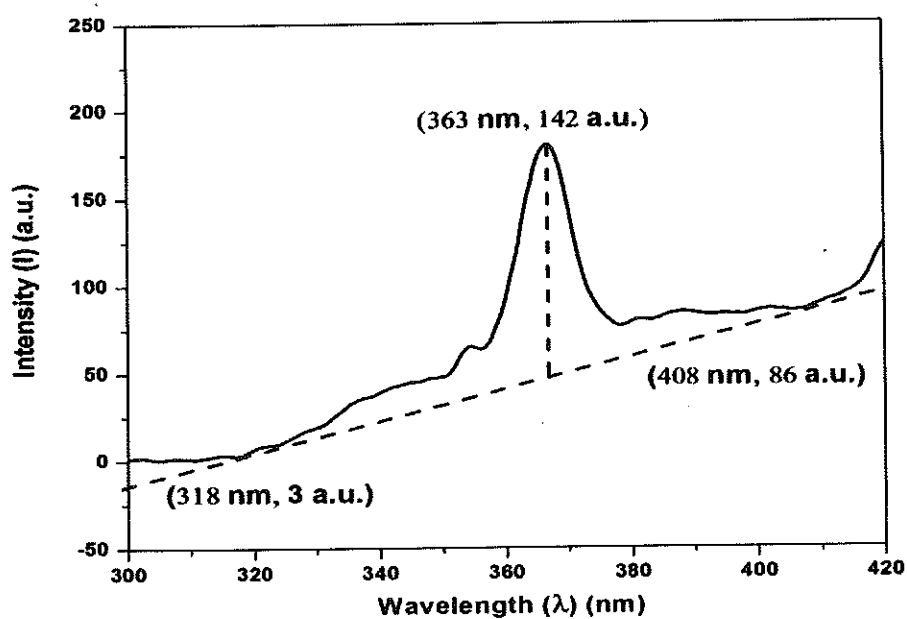


Figure B.2 data values of presented symbols in background correction equation.

2. Data values in Table 1B were used in equation B.1 as shown follows in equation B.2 - B.4., respectively.

$$I = 142 \text{ a. u.} - [86 \text{ a. u.} + (3 \text{ a. u.} - 86 \text{ a. u.}) \left(\frac{408 \text{ nm} - 363 \text{ nm}}{408 \text{ nm} - 318 \text{ nm}} \right)] \quad (\text{B.2})$$

$$I = 142 \text{ a. u.} - 44.5 \text{ a. u.} \quad (\text{B.3})$$

$$I = 97.5 \text{ a. u.} \quad (\text{B.4})$$

The background correction method was applied to other samples of prepared SnO_2 thin films for correction of photoluminescence emission intensity data.

VITAE

NAME

Mr. Jumnain Putpan

BIRTH DATE

18 November 1986

BIRTH PLACE

Yasothon Province, Thailand

EDUCATION

B. Sc. (Chemistry), Department of Chemistry,
Faculty of Science, Ubon Ratchathani University,
Ubon Ratchathani, Thailand, 2004-2008.

M. Sc. (Chemistry), Department of Chemistry,
Faculty of Science, Ubon Ratchathani University,
Ubon Ratchathani, Thailand, 2009-2012.

SCHOLARSHIPS

Research Price from Center of Excellence for
Innovation in Chemistry, Office of the Higher
Education Commission, Ministry of Education:
Postgraduate Education and Research Program in
Chemistry (PERCH-CIC), 2009-2011.

Research Price from Faculty of Science, Ubon
Ratchathani University, Ubon Ratchathani, Thailand,
2009-2012.

PUBLICATION

Jumnain Putpan and Suwat Pabchanda. "Structural
and optical properties of (Fe and Sb)-doped tin
dioxide films prepared by spray pyrolysis method".
Journal of Science and Technology, University of
Ubon Ratchathani, 14th, volume 3, July - September,
pages 9 - 16, 2012.

PRESENTATIONS

6th Ubon Ratchathani Research Conference
(UBRC 6th) in the title of "Structural and optical
properties of (Fe and Sb)-doped tin dioxide films
prepared by spray pyrolysis method", Sunee Grand &
Convention Center Hotel, Ubon Ratchathani,

Thailand, 2012, (Oral presentation).

7th PERCH Congress in the title of“(Fe, Sb, Cu or Zn)-doped Tin Dioxide Thin Films Deposited by Spray Pyrolysis: Doping Influence on The Structural and Optical Properties of Film”. Jomtien Palm Beach Hotel & Resort, Pattaya, Chonburi, Thailand, 2011, (Poster presentation).